

NCNR
Highlights
2008

Magnetic Order versus Superconductivity in the Iron-based $\text{La}(\text{O}_{1-x}\text{F}_x)\text{FeAs}$ Systems

C. de la Cruz^{1,2}, Q. Huang³, J. W. Lynn³, J. Li^{3,4}, W. Ratcliff II³, J.L. Zarestky⁵, H.A. Mook², G.F. Chen⁶, J.L. Luo⁶, N.L. Wang⁶, and P. Dai^{1,2}

The recent discovery of superconductivity in the rare-earth (R) iron-based oxide systems [$\text{RO}_{1-x}\text{F}_x\text{FeAs}$ and $(\text{Ba}, \text{Sr}, \text{Ca})\text{Fe}_2\text{As}_2$] opens a new field because these materials are the first oxide superconductors not containing copper with transition temperatures (T_c) exceeding 50 K. The parent (non-superconducting) LaOFeAs material is metallic but shows anomalies near 150 K in resistivity, dc magnetic susceptibility, and specific heat, while optical conductivity and theoretical calculations suggest that these anomalies are caused by the development of a spin-density-wave magnetic order. In the high-transition temperature (high- T_c) copper oxides it is generally believed that antiferromagnetism plays a fundamental role in the superconducting mechanism because superconductivity occurs when mobile ‘electrons’ or ‘holes’ are doped into the parent antiferromagnetic Mott insulator compounds, and the question naturally arises whether the superconductivity in these two classes of materials have a common origin.

The present neutron measurements demonstrate that LaOFeAs undergoes an abrupt structural transition below ≈ 150 K, distorting the tetragonal crystal symmetry, and this is the origin of the transport anomalies in these systems. However, the structural transition is closely followed by the development of long range spin-density-wave-type antiferromagnetic order at ≈ 137 K. The ordered moment is quite small, indicating that the magnetism is itinerant in nature, but with a simple commensurate magnetic structure. Doping the system with fluorine suppresses both the magnetic order and structural distortion in favor of superconductivity. Therefore, much like high- T_c copper oxides, the superconducting regime in these Fe-based materials occurs in close proximity to a long-range ordered antiferromagnetic ground state.

Neutron diffraction was employed to study samples of polycrystalline non-superconducting LaOFeAs and superconducting $\text{La}(\text{O}_{1-x}\text{F}_x)\text{FeAs}$ with $x = 0.08$ ($T_c = 26$ K) [1].

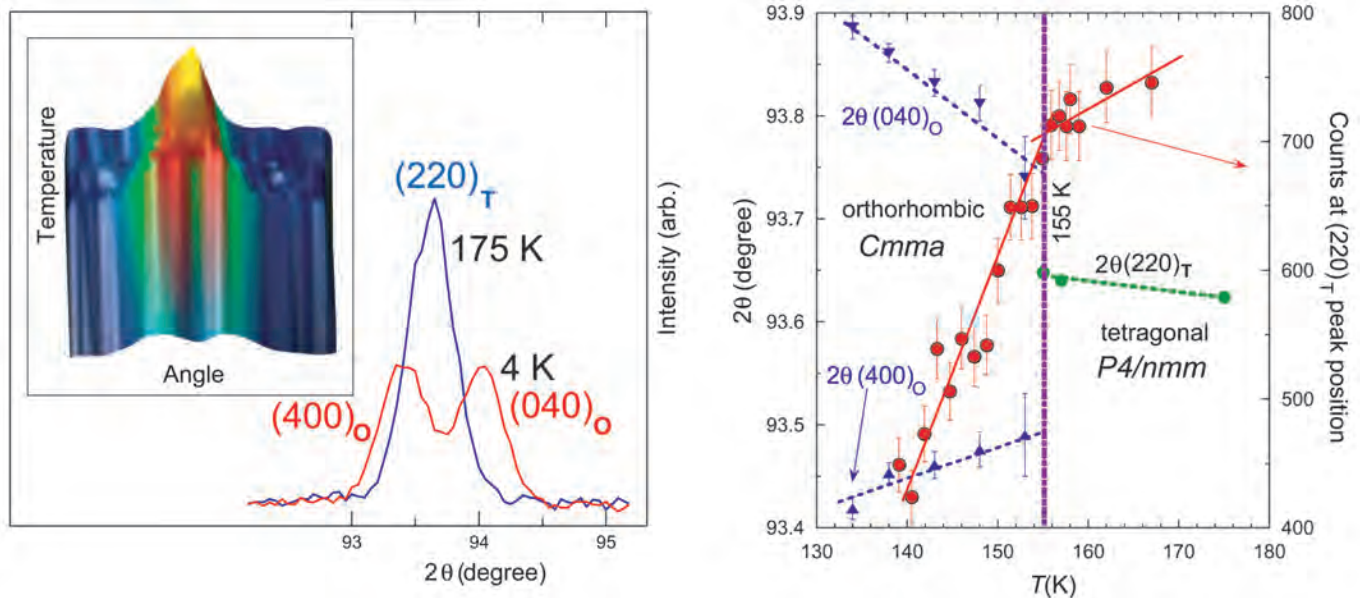


FIGURE 1: Temperature dependence of the $[2,2,0]$ structure reflection. Left: The diffraction intensity profile in the inset shows that the angle dependence of the $[2,2,0]_T$ reflection abruptly splits into two peaks [$[4,0,0]_O$ and $[0,4,0]_O$, $[O$ denotes orthorhombic]] as a function of temperature. The graph shows the data at 175 K, and in the ground state at 4 K. A structural transition has occurred from the high temperature structure with tetragonal symmetry to orthorhombic symmetry [$Cmma$]. The right plot shows the intensity (red symbols) at the peak position for the tetragonal peak, which decreases rapidly below the transition at 155 K as the peak positions move apart. The fitted peak positions (blue and green symbols) are also shown, and indicate the abrupt nature of the transition.

¹ The University of Tennessee, Knoxville, TN 37996

² Oak Ridge National Laboratory, Oak Ridge, TN 37831

³ NIST Center for Neutron Research, National Institute of Standards and Technology, Gaithersburg, MD 20899

⁴ University of Maryland, College Park, MD 20742

⁵ Ames Laboratory and Iowa State University, Ames, IA 50011

⁶ Beijing National Laboratory for Condensed Matter Physics, Institute of Physics, Chinese Academy of Sciences, Beijing 100080, China

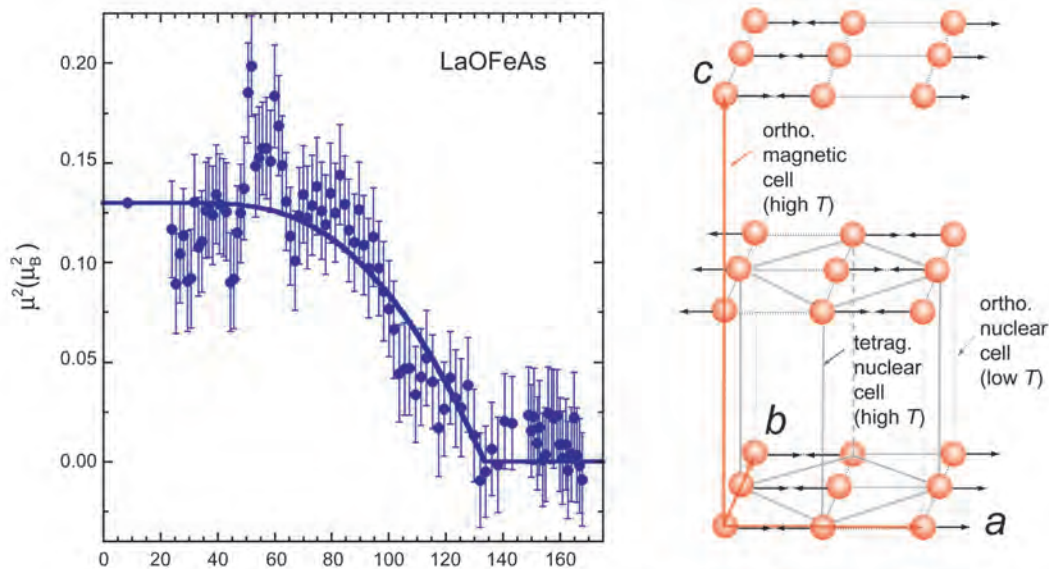


FIGURE 2: Temperature dependence of the order parameter for the strongest (1,0,3) magnetic reflection. Data were obtained in diffraction mode using the position-sensitive detector. The solid curve is a simple fit to mean field theory, which indicates that the order develops at a Néel temperature of $T_N = 137(3)$ K. The figure on the right shows the antiferromagnetic structure of the system, giving a $\sqrt{2}a_T \times \sqrt{2}a_T \times 2c_T$ magnetic unit cell. All the magnetic structures for this class of materials have antiparallel spins along the a direction and parallel spins along the b direction, with $a > b$ and the spin direction along a . Both the magnetic and structural transitions are absent in superconducting $\text{La}(\text{O}_{1-x}\text{F}_x)\text{FeAs}$ ($T_c = 26$ K).

At 170 K detailed refinements of the data obtained on BT-1 show that the crystal structure belongs to the expected tetragonal $P4/nmm$ space group. Upon cooling to 4 K, the (2,2,0) reflection that has a single peak at 170 K splits into two peaks as shown in Fig. 1. This immediately demonstrates that a structural phase transition has occurred. The symmetry of the low temperature phase can be described by an orthorhombic $Cmma$ space group with (approximate) unit cell $\sqrt{2}a_T \times \sqrt{2}a_T \times c_T$ (the subscript T refers to the tetragonal parent cell). The detailed temperature dependent data shown in Fig. 1 reveal that there is an abrupt splitting of the (2,2,0) peak that occurs at ≈ 155 K. These results thus indicate that the non-superconducting system has a structural phase transition and this phase transition is associated with the observed resistivity and specific heat anomalies. Since a similar splitting of the (2,2,0) peak is absent in superconducting $\text{La}(\text{O}_{0.92}\text{F}_{0.08})\text{FeAs}$, one can safely assume that this transition is suppressed with the appearance of superconductivity in $\text{La}(\text{O}_{1-x}\text{F}_x)\text{FeAs}$ via fluorine doping.

We now turn to the search for magnetic order in the undoped system. The magnetic scattering is expected to be quite weak, and we therefore carried high-intensity/coarse resolution measurements on BT-7 to search for spin-density-wave magnetic order in LaOFeAs . The data revealed that there are extra peaks in the low temperature diffraction pattern that are simply related to the chemical unit cell. Indexing these reflections indicates that these magnetic peaks arise from a simple stripe-type antiferromagnetic structure of Fe moments with a magnetic cell $\sqrt{2}a_T \times \sqrt{2}a_T \times 2c_T$ as indicated in Fig. 2. To see if the observed magnetic scattering at low temperature in LaOFeAs is associated with the 150 K phase transition, we carried out a measurement

of the strongest magnetic peak. Figure 2 shows the temperature dependence of the square of the ordered magnetic moment (proportional to the magnetic intensity), which vanishes at ≈ 137 K, about ≈ 18 K lower than the structural phase transition (Fig. 1). That the magnetic order is established at lower temperatures than the structural distortion is quite surprising. Normalizing the magnetic intensity to the nuclear scattering, we find an ordered Fe moment in the ground state of $0.36(5) \mu_B$. The small value of the moment suggests that this is an itinerant electron (band) magnetic. Finally, we note that an identical scan in the superconducting $\text{La}(\text{O}_{0.92}\text{F}_{0.08})\text{FeAs}$ shows that this magnetic peak is absent. Therefore, the resistivity anomaly in the parent compound is caused by structural distortion, not spin-density-wave ordering as originally suggested, while both transitions are suppressed when the system is doped into the superconducting regime. The disappearance of the static antiferromagnetic order and the lattice distortion in the doped superconducting materials suggests that the underlying physical properties of this class of superconductors may have important similarities to the high- T_c copper oxides. In any event, there is no doubt that this new class of materials will open new avenues of research regardless of the origin for the electron pairing and superconductivity.

References

- [1]. C. de la Cruz, Q. Huang, J. W. Lynn, J. Li, W. Ratcliff II, J. L. Zarestky, H. A. Mook, G. F. Chen, J. L. Luo, N. L. Wang, and P. Dai, *Nature* **453**, 899 (2008).
- [2]. T. Yildirim, *Phys. Rev. Lett.* **101**, 057010 (2008).

Competing Magnetic Interactions, Frustration, and the Structural Phase Transition in LaOFeAs

T. Yildirim¹

The layered rare-earth iron-pnictide quaternary oxides $R\text{OFeAs}$ ($R = \text{La, Ce, Sm, etc.}$) exhibit superconductivity up to a transition temperature (T_C) of 55 K when doped with either electrons (O_{1-x}F_x) or holes ($\text{La}_{1-x}\text{Sr}_x$) [1]. This marks the first non-copper based oxides that, like the cuprates, superconduct at relatively high temperatures upon electron and hole doping of their non-superconducting parent compounds. Clearly, understanding the electronic, magnetic, and structural properties of the parent compound LaOFeAs is key to determining the underlying mechanism that makes these materials superconduct upon electron/hole doping.

Experimental studies including resistivity and magnetic susceptibility show an anomaly near 150 K in LaOFeAs [1]. The origin of this anomaly has been very recently determined by neutron scattering studies [2]. It has been found that LaOFeAs exhibits spin-density-wave (SDW) antiferromagnetic long-range ordering with a small moment ($0.35 \mu_B$ per Fe) followed by a small structural distortion [2]. Even though the SDW ordering was predicted from Fermi surface nesting, there is no proposed microscopic theory that explains the origin of the observed structural distortion. It is also not clear if the magnetic and structural phase transitions are related to each other. Finally, given the fact that both the cuprates and LaOFeAs exhibit antiferromagnetic ordering, one wonders how strong and what kind of magnetic spin-fluctuations are present in the two dimensional (2D) Fe-square lattice of LaOFeAs.

Very recently, from accurate all-electron density functional calculations we have answered some of these questions [3]. We considered a $\sqrt{2} \times \sqrt{2}$ -supercell of the primitive cell of LaOFeAs (see Fig.1). In order to determine the true ground state, we have considered four different cases. These are non-magnetic (NM), ferromagnetic (F) and the two different antiferromagnetic spin configurations shown in Fig.2. The first one of the antiferromagnetic configurations is AF1 where the nearest neighbor spins are antiparallel to each other. The second antiferromagnetic configuration, AF2, is shown in Fig. 2b. In AF2 the Fe spins along the square

diagonal are aligned antiferromagnetically. This is the stripe-phase recently observed [2]. The AF2 spin configuration can be considered as two interpenetrating simple square AF sublattices (red and blue sublattices in Fig. 2b). We note that since each Fe ion is at the middle of a square AF lattice, the mean field at each spin site is zero. Hence one sublattice can be rotated freely with respect to the other sublattice without costing any energy. For this reason the AF2 spin-configuration is fully frustrated.

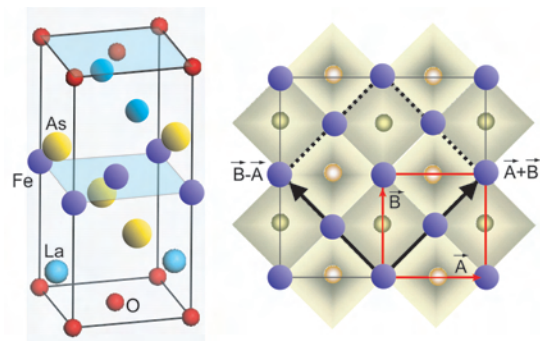


FIGURE 1: The crystal structure of LaOFeAs (left) and the top view of the FeAs-plane and the relations between primitive and $\sqrt{2} \times \sqrt{2}$ -supercell used in our calculations. The dark and light shaded areas indicate the As atoms below and above the Fe-square lattice, respectively.

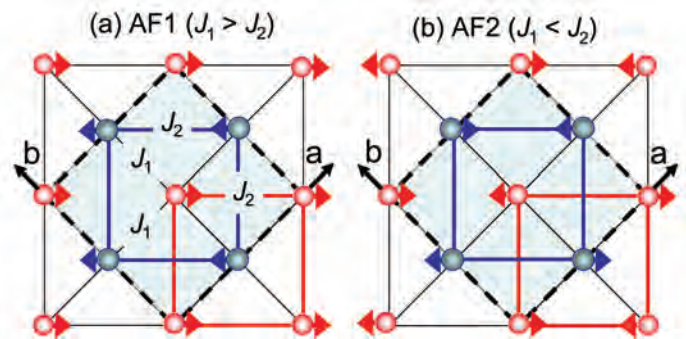


FIGURE 2: Two antiferromagnetic configurations considered in this study.

In order to determine which spin configurations among NM, F, AF1, and AF2, is the ground state, we have carried out total energy calculations as a function of Fe-magnetic moment. Our results are summarized in Fig. 3. The zero of energy is taken as the $M = 0$ case (i.e., NM calculation). From Fig. 3, it is clear that LaOFeAs has only one magnetic ground state which is AF2. The Ferro spin-configuration always results in the highest energy, regardless the Fe-magnetic moment. Similarly, AF1 ordering

¹NIST Center for Neutron Research, National Institute of Standards and Technology, Gaithersburg MD 20899

always yields energies higher than the NM case. For the AF2 ordering, we see that the energy minimum occurs near the fixed moment calculation with $M = 1\mu_B$. Repeating calculations where magnetization is not fixed, we obtained the optimum magnetic moment as $M = 0.87\mu_B$ per Fe. As we discuss below in detail, the Fe magnetic moment is further reduced almost by a half when the structure is allowed to distort due to AF2 stripe ordering.

In order to gain a better insight into the nature of the magnetic interactions present in Fe-square lattice of the LaOFeAs system, we map the calculated total energies of the F, AF1 and AF2 configurations shown in Fig. 3a to a simple Heisenberg like model. For fully localized spin-systems this is a perfect thing to do but for the case of LaOFeAs this is only an approximation. Nevertheless, the calculated J s should be a good indication of the magnetic interactions present in the system. Fig. 3b shows J_1 and J_2 obtained from the energies of the F, AF1 and AF2 at given magnetic moment. It is clear that both J_1 and J_2 are quite large and positive (i.e., antiferromagnetic). J_2 is always larger than $J_1/2$ and therefore the AF2 structure is the only ground state for any given moment of the Fe ion. By looking at the exchange paths for J_1 and J_2 , we notice that the Fe-As-Fe angle is around 75° and 120° for nn and nnn Fe-pairs, respectively. Hence it makes sense that the 2nd nn exchange interaction is as strong as the nn exchange because the angle is closer to the optimum value of 180° . It is quite surprising and also very interesting that there are strong and competing antiferromagnetic interactions in the LaOFeAs system that results in a totally frustrated AF2 spin configuration.

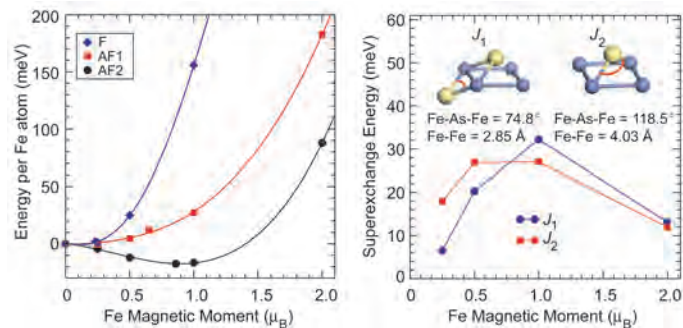


FIGURE 3: Left: The total energy per Fe atom versus magnetic moment for F, AF1 and AF2 spin-configuration, indicating AF2 is the only ground state of the system. Right: The magnetic interactions for nn and nnn Fe ions obtained from the energies of F, AF, and AF2 configurations.

We next discuss the implication of the magnetically frustrated AF2 configuration on the structural distortion recently observed by neutron scattering [2]. Fig. 4 shows the total energy of the AF2 spin configuration as a function of the γ angle. When $\gamma = 90^\circ$, we have the original tetragonal cell. Once γ deviates from 90° , the original $\sqrt{2}\times\sqrt{2}$ -structure (shown as a dashed line) is no longer tetragonal but orthorhombic (i.e., the cell lengths along the a and b axes are no longer equal). The total energy versus γ plot shown in Fig.4 clearly indicates that the structure is indeed distorted with $\gamma = 91.0^\circ$, which is in good agreement with the

experimental value of 90.3° . From the all-electron method we get $M = 0.48\mu_B$ which is in excellent agreement with the experimental value of $0.35\mu_B$. The net energy gain by the structural distortion is about 12 meV per cell, which is of the same order as the temperature at which this phase transition occurs. We also considered two types of AF2 where the spins along the short axis are aligned parallel or antiparallel. These two configurations are no longer equivalent. According to our calculations the configuration in which the spins are ordered parallel along the short-axis is the ground state. We note that it should be possible to determine the exact spin-configuration from neutron powder diffraction. Finally, we note that the other spin configurations including the non-magnetic case do not yield structural distortion. Therefore, the experimentally observed structural distortion is due to only AF2 stripe ordering.

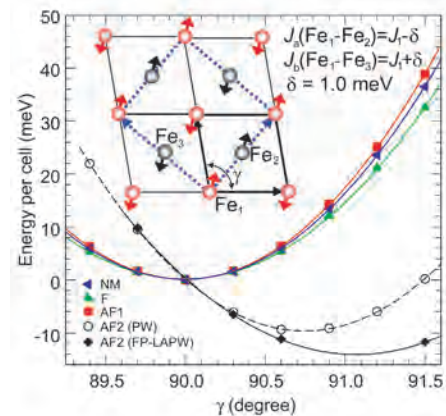


FIGURE 4: The total energy per cell versus the angle γ for NM, F, AF1 and AF2 spin-configurations. Note that only the AF2 spin configuration yields structural distortion. The inset shows that as γ increases, the ferromagnetically aligned Fe ions [i.e., Fe1-Fe2] get closer while the antiferromagnetically aligned ions [i.e., Fe1-Fe3] move apart.

In conclusion, from first-principles fixed spin moment calculations we show that ferromagnetic and checkerboard antiferromagnetic (AFM) ordering in LaFeAsO are not stable and the stripe AFM configuration with $M(\text{Fe}) = 0.48\mu_B$ is the only stable ground state. The main exchange interactions between Fe ions are large, antiferromagnetic and frustrated. The stripe AFM phase breaks the tetragonal symmetry, removes the frustration, and causes a structural distortion. These results successfully explain the magnetic and structural phase transitions in LaOFeAs recently observed by neutron scattering. The presence of competing strong antiferromagnetic exchange interactions suggest that magnetism and superconductivity in doped LaOFeAs may be strongly coupled, much like in the high- T_C cuprates.

REFERENCES

- [1] Y. Kamihara, T. Watanabe, M Hirano, H. Hosono, J. Am. Chem. Soc. **130**, 3296 (2008).
- [2] C. de la Cruz, Q. Huang, J.W. Lynn, J. Li, W. Ratcliff II, H.A. Mook, G.F. Chen, J.L. Luo, N.L. Wang, and P. Dai, Nature **453**, 899 (2008).
- [3] T. Yildirim, Phys. Rev. Lett. **101**, 057010 (2008).

Structural Origin of the Enhanced Magnetostrictive Properties of $\text{Fe}_{1-x}\text{Ga}_x$ (Galfenol)

H. Cao¹; P. M. Gehring²; C. P. Devreugd, J-F. Li, D. Viehland³; J. A. Rodriguez⁴

Galfenol is the name given to alloys of Ga and Fe created by the Naval Ordnance Labs in 1998 that exhibit very large magnetostriction and a high relative permeability coupled with robust mechanical properties. Magnetostrictive materials are the magnetic analogue of piezoelectrics in that they can be used to convert between electrical and mechanical forms of energy via their mechanical response to an applied magnetic field. Although Galfenol has only 1/3rd to 1/4th the magnetostriction of Terfenol-D, an alloy based on Tb, Dy, and Fe that exhibits the highest room-temperature magnetostriction of any known material, it is nonetheless an extremely attractive choice for use in device applications such as magneto-acoustic sensors, actuators, and transducers because it can be used in mechanically harsh environments with minimal shock hardening.

The addition of Ga into the body-centered cubic (bcc) α -Fe (or $A2$) phase is known to produce a diversity of crystal structures. In fact, both equilibrium and metastable $\text{Fe}_{1-x}\text{Ga}_x$ phase diagrams have been reported [1]. In the metastable case a chemically ordered bcc Fe_3Ga (or DO_3) phase coexists with the $A2$ phase for $0.14 < x < 0.20$ [4], where both the magnetostriction along the [100] direction (λ_{100}) and the stability of the two-phase region are strongly affected by the rate of cooling. The presence of two peaks in the magnetostriction as a function of Ga content has been reported for alloys that have been cooled rapidly from high temperatures. The first peak at $x \approx 0.19$ has been attributed to an increase in the magneto-elastic coupling that results from the formation of short-range ordered (SRO) Ga pairs along the [100] axis of the $A2$ structure, while the second peak at $x \approx 0.27$ has been attributed to a softening of the shear modulus $c' = (c_{11} - c_{12})/2$. The history dependence of both λ_{100} and the $A2$ - DO_3 two-phase region suggests that the enhanced magnetostriction maybe due to an underlying heterogeneity rather than being due to a conventional homogeneous ferromagnetic phase.

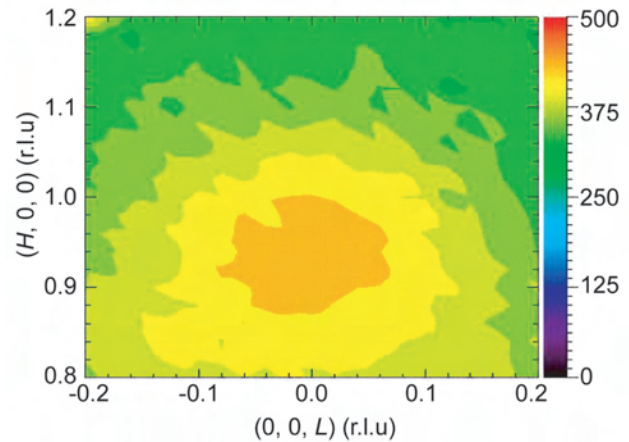


FIGURE 1: Neutron scattering intensity map measured at 300 K on a furnace-cooled single crystal of $\text{Fe}_{0.81}\text{Ga}_{0.19}$. The symmetry of the underlying matrix allows no $(1,0,0)$ reflection. The broad diffuse scattering that peaks near $(0.95,0,0)$ thus indicates the presence of a short-range ordered structure having a different symmetry and lattice spacing.

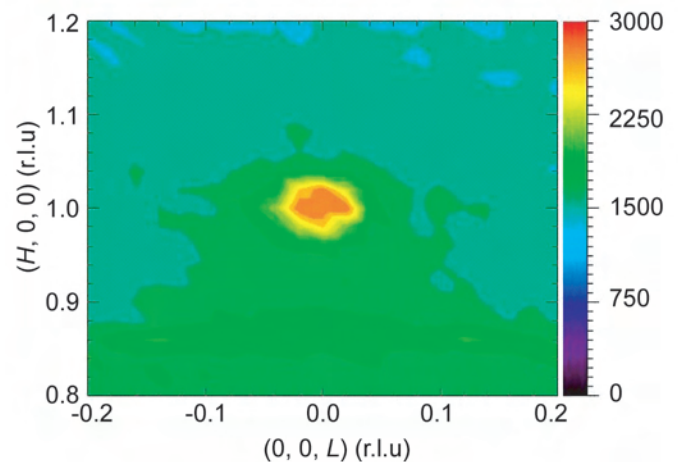


FIGURE 2: Neutron scattering intensity map measured at 300 K on a slow-cooled single crystal of $\text{Fe}_{0.81}\text{Ga}_{0.19}$. Under slow-cooled conditions, $\text{Fe}_{0.81}\text{Ga}_{0.19}$ exhibits a long-range ordered structure with DO_3 symmetry, for which a $(1,0,0)$ reflection is allowed. The diffuse scattering observed in the quenched crystal is absent. The diffuse scattering located below the line $H = 1$ and shown in green is believed to be size-effect scattering.

Figure 1 shows a color contour plot of the neutron diffuse scattering intensity measured at room temperature in the vicinity of the $(1,0,0)$ reciprocal lattice position from a furnace cooled ($10^\circ\text{C}/\text{min}$) single crystal of $\text{Fe}_{0.81}\text{Ga}_{0.19}$, a composition corresponding to one of the two peaks in the magnetostriction

¹Virginia Polytechnic Institute and State University, Blacksburg, VA 24061

²NIST Center for Neutron Research, National Institute of Standards and Technology, Gaithersburg, MD 20899

³Virginia Polytechnic Institute State University, Blacksburg, VA 24061

⁴University of Maryland, College Park, MD 20742

[2]. The presence of substantial diffuse scattering, slightly offset from (1,0,0), is evident and is shown in orange and yellow. This broad scattering is consistent with the presence of a short-range ordered structure having a symmetry and lattice spacing different from that of the underlying $A2$ matrix, which admits no structural peak at (1,0,0). Identical neutron scattering measurements made on a slowly-cooled (2 °C/min) single crystal of the same composition, for which the magnetostriction is markedly lower, are shown in Fig. 2. In this case a strong and sharp Bragg peak is seen at (1,0,0), consistent with a long-range ordered DO_3 structure. More importantly, no evidence is seen of the broad and nearly isotropic diffuse scattering shown in Fig. 1. Instead anisotropic diffuse scattering contours are observed below the line $H = 1$, which are believed to arise from correlated atomic displacements that result from the atomic size mismatch between Fe and Ga, also known as size effect diffuse scattering.

To ascertain whether or not the diffuse scattering observed in Fig. 1 is related to the enhanced magnetostriction observed in quenched alloys of Galfenol, linear Q -scans through the diffuse scattering intensity along the [100] direction were made on three different compositions of $Fe_{1-x}Ga_x$ with very different values of magnetostriction. Data were obtained on single crystals for $x = 0.10, 0.15$, and 0.19 , which are shown in Fig. 3. It is immediately apparent that the diffuse scattering grows markedly with increasing Ga content and in fact tracks the corresponding increase in the magnetostriction. These data are consistent with a structurally heterogeneous model [3] that was proposed to explain the enhanced magnetostriction in Galfenol alloys. This model assumes that the quenched condition is in fact a structurally and chemically heterogeneous state consisting of coarsening-resistant DO_3 nanoprecipitates within an $A2$ matrix. An essential element of this model is that the nanoprecipitates possess a lower than cubic symmetry.

Close examination of the data in Fig. 3 reveals an asymmetry in the diffuse scattering, especially for $x = 0.19$, that is well described by tetragonally-distorted DO_3 regions with a tetragonality $c/a = 1.2$. This value agrees precisely with that predicted by the structurally heterogeneous model. This finding lends strong credence to idea that the large magnetostriction in quenched Galfenol alloys is directly related to the structural heterogeneity of the DO_3 nanoprecipitates, i.e., that the enhancement of λ_{100} results from the redistribution of the orientation of lower symmetry DO_3 -like nanoprecipitate particles under field or stress.

References

- [1] O. Ikeda, R. Kainuma, I. Ohnuma, K. Fukamichi, K. Ishida, J. Alloys and Compounds **347**, 198 (2002).
- [2] H. Cao, P. M. Gehring, C. Devreugd, J-F. Li, and D. Viehland, submitted to Phys. Rev. Lett.
- [3] A. G. Khachatryan and D. Viehland, Metal. and Mater. Trans. A **38A**, 2308 (2007).

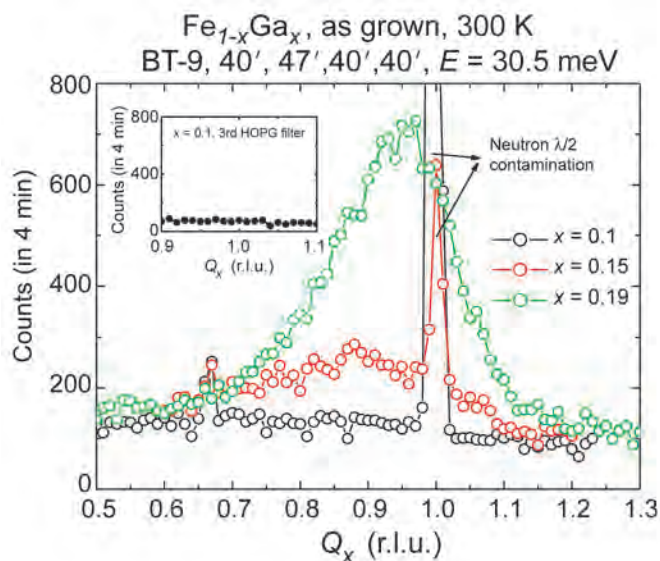


FIGURE 3: Diffuse scattering profiles measured at 300 K near [1,0,0] along [1,0,0] are shown for furnace-cooled $Fe_{1-x}Ga_x$ ($x = 0.10, 0.15, 0.19$). The peak and Q -integrated diffuse scattering intensities grow with increasing Ga content and track the magnetostriction, which reaches a maximum value for $x = 0.19$. The sharp peaks at [1,0,0] and [0.67,0,0] come from neutrons with wavelengths $\lambda/2$ and $\lambda/3$, respectively, that scatter from the [2,0,0] reflection, and vanish after inserting a third HOPG filter before the sample as shown in the inset.

Tuning the Magnetocaloric Properties of the Magnetic Refrigerant $\text{MnFe}(\text{P}_{1-x}\text{Ge}_x)$

D. Liu^{1,2}, M. Yue², J. Zhang², T. M. McQueen³, J. W. Lynn¹, X. Wang², Y. Chen^{1,4}, J. Li^{1,4}, R. J. Cava³, X. Liu⁵, Z. Altounian⁵, Q. Huang¹

The magnetocaloric effect (MCE)—the expulsion of heat from a material when a magnetic field is applied and its absorption when the field is removed—was discovered in 1881. In 1933 using a technique based on MCE called “adiabatic demagnetization” a temperature well below 1 K was achieved for the first time, and for most of its history the effect was only useful for producing very low temperatures. Recently, magnetic refrigeration at ambient temperatures has attracted renewed interest with the discovery of new materials with improved efficiencies and advantages, as potential replacements for the classical vapor compression systems in use today. To be useful the magnetorefrigerant needs to have a large change in magnetic entropy near room temperature for modest applied fields (< 2 T), be inexpensive, and environmentally friendly, and $\text{Mn}_{1-y}\text{Fe}_{1-y}\text{P}_{1-x}\text{Ge}_x$ is the first system to fulfill all these requirements.

We have used neutron diffraction and magnetization measurements to reveal that the application of a magnetic field drives the material through a first order phase transition from paramagnetic (PM) to ferromagnetic (FM), and that these phases correspond to two very distinct crystal structures. The latent heat of this transition, deriving both from the sudden onset of magnetic order and change in crystal structure, is the source of the MCE [1]. This entropic control of combined magnetic and structural transitions circumvents the limitation imposed by the magnetic entropy alone, and provides a new pathway to optimize the refrigerant properties. Indeed, by tuning the physical properties of this system we now have achieved an MCE of ≈ 75 J/Kg K on both increasing and decreasing field cycles, more than twice the value of the previous record, thrusting $\text{Mn}_{1-y}\text{Fe}_{1-y}\text{P}_{1-x}\text{Ge}_x$ into the lead as a viable commercial refrigerant.

Neutron powder diffraction is the classic technique to solve for both crystal and magnetic structures, and for $\text{Mn}_{1.1}\text{Fe}_{0.9}\text{P}_{0.8}\text{Ge}_{0.2}$ we find it is single phase and paramagnetic above ≈ 260 K, single phase and

ferromagnetic below 200 K, and in between undergoes a strongly first-order phase transition as a function of temperature or applied magnetic field (see Fig. 1). It turns out that both phases possess the same space group symmetry ($P\bar{6}2m$) but have distinctly different structures, with the *a*- and *b*-axes being ≈ 1.3 % longer while the *c*-axis is contracted by ≈ 2.6 % in the FM phase compared to the PM phase. There is no significant change in the unit cell volume for the two phases. We find that one site (3*g*) (see upper panel of Fig. 2) is completely occupied by Mn atoms, which are co-planar with P/Ge(1) atoms at the 1*b* site in the *z* = 0.5 layer. The other site (3*f*) has ≈ 93 % Fe, with ≈ 7 % Mn distributed randomly, and the 3*f* Fe/Mn site is co-planar with the P/Ge(2) atoms at the 2*c* site in the *z* = 0 layer. Ge and P are randomly mixed, although Ge atoms prefer the P/Ge(2) (2*c*) site (≈ 27 % Ge occupied) to the P/Ge(1) (1*b*) site (≈ 5 % Ge). For the ferromagnetic phase the refinements give Mn and Fe moments parallel in the *a*-*b* plane, with ordered moments (at 245 K) of 2.9(1) μ_B and 0.9(1) μ_B for the Mn (3*g*) site and Fe/Mn (3*f*) site, respectively, similar to what is seen for other compounds with the Fe_2P -type structure.

The important point is that the results demonstrate that magnetic field, or temperature, has no significant effect other than to convert the system between the ferromagnetic and paramagnetic structural phases.

The results make it clear that the large MCE originates from the applied magnetic field driving the phase conversion, and the measured magnetic entropy changes are shown in Fig. 2. For magnetic field increasing and decreasing we obtain 74 J/Kg K and 78 J/Kg K, respectively, for a field change of 5 T in this bulk $\text{Mn}_{1.1}\text{Fe}_{0.9}\text{P}_{0.8}\text{Ge}_{0.2}$ compound. These values are twice the previous value for this system and the highest MCE for any material presently known. It is also quite unusual to be able to achieve similar values in both field directions, as typically the field-decreasing MCE can be quite drastically reduced. For the present material the field-decreasing MCE actually exceeds the field-increasing values.

¹ NIST Center for Neutron Research, National Institute of Standards and Technology, Gaithersburg, MD 20899

² Beijing University of Technology, Beijing 100022, China

³ Princeton University, Princeton, NJ 08544

⁴ University of Maryland, College Park, MD 20742

⁵ McGill University, Montreal, Quebec, H3A 2T8, Canada

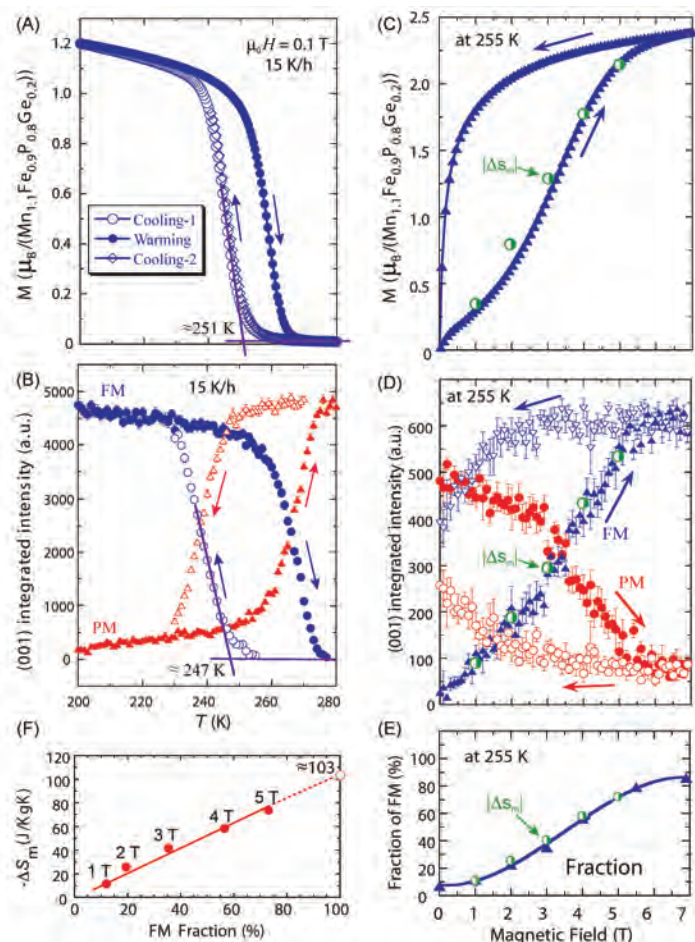


FIGURE 1: Comparison of the diffraction and magnetization measurements. (A) Temperature dependence of the magnetization in an applied field of 0.1 T. (B) Integrated intensities of the (001) reflections for the PM- and FM- phases as a function of temperature on cooling and warming. (C) Field-dependent magnetization at 255 K. The magnetic entropy change $|\Delta S_M|$, normalized to the magnetization, is shown for comparison. (D) Field dependence of the integrated intensities of the (001) reflections for the PM-phase and FM-phase at 255 K, showing that the FM-phase fraction tracks the magnetization data and normalized magnetic entropy change $|\Delta S_M|$. (E) Fraction of the FM-phase at 255 K as the field increases. The FM-phase fraction increases smoothly to $\approx 86\%$. Data normalized from $|\Delta S_M|$ are shown for comparison. (F) $|\Delta S_M|$ increases linearly with the FM-phase fraction. $|\Delta S_M|$ is projected to be ≈ 103 J/Kg K if the transition went to completion for this sample.

The present results directly demonstrate that the transition from the PM-phase to the FM-phase and the associated huge magnetocaloric effect are directly controlled by the first-order structural phase transition between these two phases, and, moreover, that a completed phase conversion will increase the MCE up to ≈ 100 J/Kg K in a field of 5 T in this system. The transition can be driven by temperature or applied magnetic field, and for use as a magnetic refrigerant the field-dependent properties are critical. The improved properties and overall advantages of this material open the possibility for its use in magnetic refrigerant applications.

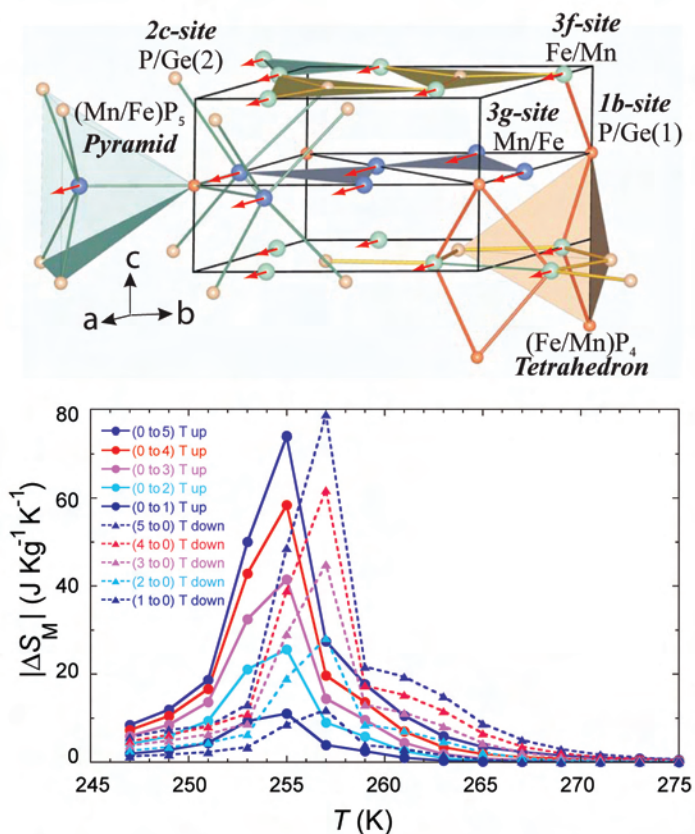


FIGURE 2: The Magnetocaloric Effect. Temperature dependence of the entropy change of the bulk $Mn_{1.1}Fe_{0.9}P_{0.8}Ge_{0.2}$ compound as a function of applied magnetic field up to 5 T. The upper panel shows the crystal structure for the FM-phase which differs from that in the PM-phase in the ordering of the spins and the lengths of a , b , and c .

This material also exhibits a large magnetoelastic effect—the change in the lattice constants with magnetic field—and this useful property also originates from the structural changes associated with the first-order transition. Furthermore, our investigations suggest a number of ways in which the magnetothermal properties can be tuned by chemical doping or mechanical treatment. For example, we have found that an applied field can induce substantial preferred crystallographic orientation, which results in improved field-dependent properties. We also expect that the magnetic and structural properties can be further optimized by selective chemical substitutions and processing techniques. The time dependence associated with the transition does tend to reduce the practical MCE available for applications, but the overall improvements and prospects for further advances in performance make this material the magnetic refrigerant of choice to enable a wide range of commercial magnetorefrigerant applications.

References

- [1] D. Liu, M. Yue, T. M. McQueen, J. W. Lynn, X. Wang, Y. Chen, J. Li, R. J. Cava, X. Liu, Z. Altounian, and Q. Huang, (submitted).

Electric Field Controlled Magnetism

I. Cabrera^{2,1}, M. Kenzelmann³, G. Lawes⁴, Y. Chen^{1,5}, W.C. Chen^{1,6}, R. Erwin¹, T.R. Gentile⁷, J. Leão¹, J.W. Lynn¹, N. Rogado⁸, R.J. Cava⁸, C. Broholm^{2,1}

Systems that are simultaneously magnetically ordered and ferroelectric—multiferroics—are very rare in nature. The reason is that typical ferroelectrics such as BaTiO_3 develop their electric polarization via hybridization of empty d -orbitals on the Ti ion with occupied p -orbitals of the octahedrally coordinated oxygen ions, which causes the off-centering displacement of the Ti ion and hence the net electric polarization. Magnetism such as for iron, on the other hand, requires electronically occupied d -orbitals, and thus magnetism and ferroelectricity are mutually exclusive phenomena through the standard ferroelectric mechanism. Nevertheless, the tremendous technological possibilities that would be enabled with a material in which the magnetic state can be switched with an electric field has driven research in multiferroics, and the recent discovery of a new class of multiferroic materials that feature strongly-coupled spontaneous magnetic and electric order [1] has reignited this dream of materials engineers.

The novelty of these new multiferroic materials is that ferroelectricity is generated by the magnetic structure itself, and so ferroelectricity can be easily switched when the magnetic structure is tuned by magnetic fields [2,3]. More importantly, here we show that, reciprocally, electric fields can also be used to control magnetic properties, and that the magnetic chirality or handedness can be directly controlled with the electric field—the first step towards electric field control of the macroscopic magnetic properties for device applications.

The model multiferroic system that was chosen to demonstrate this property is $\text{Ni}_3\text{V}_2\text{O}_8$, whose magnetic and electric properties we have extensively characterized previously [4-6]. The magnetism in $\text{Ni}_3\text{V}_2\text{O}_8$ arises from weakly-coupled, buckled Kagome planes of $S = 1$ quantum spins that are localized on the Ni^{2+} sites, while the V ions are nonmagnetic. $\text{Ni}_3\text{V}_2\text{O}_8$ is an insulating material (as all ferroelectrics must be) and the spin interactions are

mediated through electronic orbital overlap and the exchange of electrons in quantum mechanically entangled states. The corner-shared geometry of Ni^{2+} triangles and antiferromagnetic next-nearest neighbor interactions lead to strong magnetic fluctuations even below the temperature where simpler magnets would order, and the competition of these interactions stabilizes a series of distinctly different ordered structures with decreasing temperature.

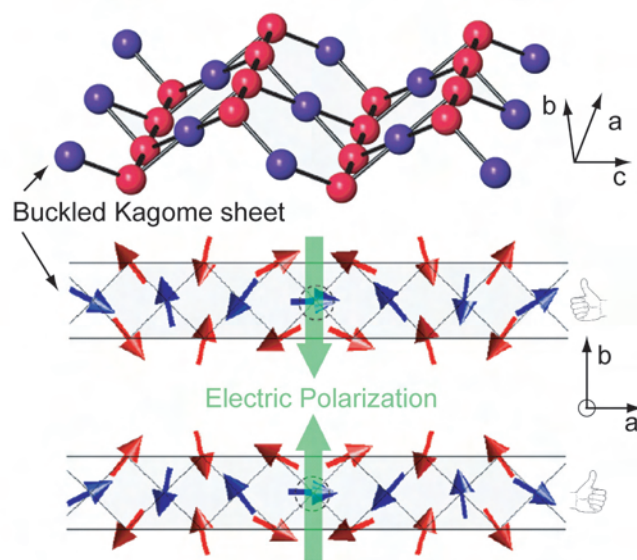


FIGURE 1: (top) Single layers of a Ni^{2+} Kagome lattice that are buckled along the c -axis, and that in $\text{Ni}_3\text{V}_2\text{O}_8$ are stacked along the b -axis. (Center/Bottom) spiral magnetic structure that is only possible because of a crystal distortion that also leads to macroscopic electric polarization, either up or down depending on the sense of rotation of the spiral.

Quite generally, all magnetic materials attempt to minimize magnetic disorder or entropy at low temperature. This is usually achieved with a static long-range order of the quantum degrees of freedom such as the spin. For incommensurate magnetic order, this is best done in a spin spiral structure with a maximally ordered moment on each site. However, in $\text{Ni}_3\text{V}_2\text{O}_8$, the crystal structure and the interactions favor incommensurate magnetic order for which the size of the ordered magnetic moment varies sinusoidally from one Ni^{2+} site to next, leading to a great amount

¹NIST Center for Neutron Research, National Institute of Standards and Technology, Gaithersburg, Maryland 20899

²Johns Hopkins University, Baltimore, Maryland 21218

³ETH Zurich, CH-8093 Zurich, Switzerland and Paul Scherrer Institute, CH-5232 Villigen, Switzerland

⁴Wayne State University, Detroit, Michigan 48201

⁵University of Maryland, College Park, MD 20742

⁶Indiana University Cyclotron Facility, Bloomington, IN 47408

⁷Physics Laboratory, National Institute of Standards and Technology, Gaithersburg, Maryland 20899

⁸Princeton University, Princeton, New Jersey 08544

of magnetic disorder near the nodes of the wave. One way to lower the magnetic entropy further is via a crystal distortion, and we have previously shown (see Fig. 1) that $\text{Ni}_3\text{V}_2\text{O}_8$ is one of the few known materials where the resulting crystal distortion involves a macroscopic electric polarization that is magnetically driven.

The ferroelectric polarization in $\text{Ni}_3\text{V}_2\text{O}_8$ can be turned on and off by simply applying a magnetic field, because a magnetic field induces different magnetic structures, some of which allow an electric polarization. The more interesting question is whether the inverse coupling can also be achieved in $\text{Ni}_3\text{V}_2\text{O}_8$, namely, can the magnetic structure be controlled with an electric field?

To test such a scenario, we prepared a single crystal of $\text{Ni}_3\text{V}_2\text{O}_8$ that was a 1 mm thin platelet normal to the ferroelectric axis. A capacitor was made by evaporating an electrode [(4 nm Cr)/(40 nm Au) layer] on each of the two faces, and then attaching Au wires using silver epoxy. The sample was held by a sapphire plate in a cryostat. During cool-down an external electric field was applied using an electrometer to obtain a macroscopic electrical polarization. We also surveyed *in-situ* the ferroelectric polarization during the neutron diffraction measurements, which were performed on BT-7 utilizing large ^3He polarizer cells to achieve the neutron polarization and analysis. The neutron polarization \mathbf{P} was chosen to be parallel to the momentum transfer wave-vector \mathbf{Q} under investigation, [$\mathbf{P} \parallel \mathbf{Q}$]. In this case the neutron polarization is reversed, or “flipped”, when the neutrons magnetically scatter from the sample, while structural Bragg peak scattering never flips the neutron spin. Then the magnetic scattering is observed when the incident neutron spin is either parallel (+) and/or antiparallel (-) to the momentum transfer wave-vector \mathbf{Q} , and since the spin is reversed on scattering we measure either the (+ -) or (- +) magnetic cross sections.

For typical magnetic materials these two cross sections would have equal intensities, but in the ferroelectric phase of $\text{Ni}_3\text{V}_2\text{O}_8$ the incommensurate magnetic order has a chirality, or handedness. The modulation wave-vector is along the \mathbf{a} axis, $(q,0,0)$ where $q \approx 0.265$, and hence the magnetic Bragg peaks occur at satellite positions such as $\mathbf{Q} = (1+q,1,1)$. Our experimental results are shown in Fig. 2, where we see that the spin-flip neutron diffraction intensity of the $(1+q,1,1)$ magnetic Bragg peak depends on the incoming neutron spin polarization. For an applied electric field of +300 kV/m the Bragg peak is only observed for the (- +) configuration; the small peak observed for the (+ -) configuration is simply due to the imperfect polarization of the instrument. More importantly, by reversing the electric field the magnetic Bragg peak is only observed in the (+ -) configuration, demonstrating in a simple and elegant way that the magnetic structure in $\text{Ni}_3\text{V}_2\text{O}_8$ can be tuned with an electric field.

It can be shown that the reversal of the neutron diffraction intensity with electric field results from an electrically induced switching of the magnetic chirality—the “handedness” of the spiral. It is believed that the microscopic coupling between the magnetic structure and the ferroelectric polarization is mediated by the Dzyaloshinskii-Moriya antisymmetric exchange interaction of the form $\mathbf{D} \times (\mathbf{S}_i \times \mathbf{S}_j)$, where \mathbf{D} changes sign when the electric polarization is switched. Switching the electric polarization of the ferroelectric domain thus changes the sense of rotation of the spin spiral.

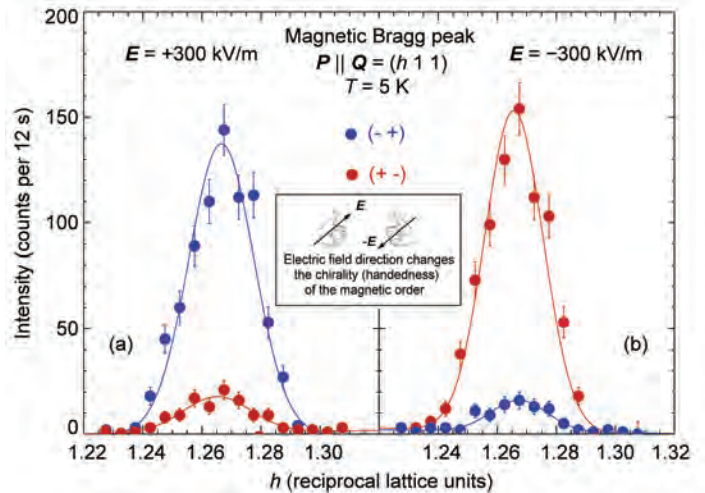


FIGURE 2: Full polarized neutron magnetic diffraction. The neutron polarization \mathbf{P} is parallel to \mathbf{Q} , [$\mathbf{P} \parallel \mathbf{Q}$], so that all the magnetic scattering is spin-flip. (a) A +300 kV/m electric field selects one chiral domain, and then the magnetic peak is only observed in the (- +) configuration; the small peak in the (+ -) configuration is due to the imperfect instrumental polarization. (b) With the ferroelectric polarization reversed by applying -300 kV/m, the magnetic Bragg peak is only observed in the (+ -) configuration.

$\text{Ni}_3\text{V}_2\text{O}_8$ illustrates the great potential for multifunctionality that can be obtained from materials with competing interactions. The most important lesson to draw from studies of these magnetically-induced ferroelectrics is that the competing magnetic interactions not only lead to novel magnetic ground states of interest to the community of condensed matter scientists, but that they also have the potential to be key components for the design of next-generation electronics, data storage and computing applications.

References

- [1] T. Kimura *et al.*, Nature **426**, 55 (2003).
- [2] M. Kenzelmann *et al.*, Phys. Rev. Lett. **95** 087206 (2005).
- [3] A.B. Harris, Phys. Rev. B **76**, 054447 (2007).
- [4] G. Lawes *et al.*, Phys. Rev. Lett. **93** 247201 (2004).
- [5] G. Lawes *et al.*, Phys. Rev. Lett. **95** 087205 (2005).
- [6] M. Kenzelmann *et al.*, Phys. Rev. B **74** 014429 (2006).

Killing Cancer Cells with Magnetic Nanoparticles

C.L. Dennis¹, A.J. Jackson^{2,3}, J.A. Borchers², R. Ivkov⁴, A.R. Foreman⁴, and C. Grüttner⁵

Fevers offer an effective system-wide defense against pathogens like bacteria by disrupting their biochemical processes, rendering the pathogens more susceptible to attack by the immune system. However, if the fever gets too high (> 45 °C in humans), then damage occurs to healthy tissue, and if left too long at elevated temperatures, the healthy tissue will die. In an analogous manner, cancer cells can be treated with heat to disrupt their biochemical processes. A key difference is that cancer cells start to experience damage at 42 °C, which leaves a 3 °C temperature window in which cancers can be killed with little or no damage to the surrounding healthy tissue. Similar to a fever, nanoparticle mediated hyperthermia is a prospective cancer therapy that destroys tumors by locally heating tumor cells.

Although hyperthermia is not a new idea, there are two distinguishing aspects of nanoparticle mediated hyperthermia as compared to “conventional” hyperthermia (i.e., a fever): 1) the heat is generated locally at the tumor cells by the magnetic nanoparticles subjected to an alternating magnetic field, and 2) the temperature change can be correlated with the energy deposited and therefore to the amount or “dose” of nanoparticles used. The primary benefit of this technology is a significant reduction in the severity and duration of side effects that are common with conventional cancer treatments like chemo- and radiation therapy because of the reduction in damage to surrounding healthy tissue.

In designing these nanoparticle systems, the primary requirement is a biologically stable material that allows control of the total amount of heat deposited in order to kill the tumor while minimizing damage to the surrounding healthy tissue. To design more effective systems, NIST researchers in collaboration with their industrial partners examined two candidates with significantly different heating characteristics. Contrary to accepted practice, we found that strongly interacting systems heat significantly better than weakly or non-interacting systems, with the degree of interaction controlled by the spacing between nanoparticles.

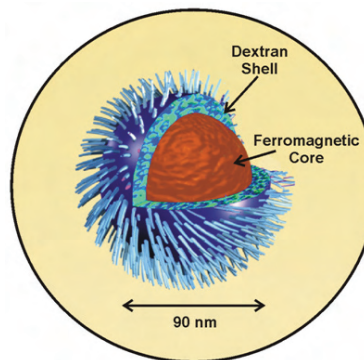


FIGURE 1: – Schematic of the magnetic nanoparticle developed for hyperthermia treatment used in these studies: The iron oxide core generates the heat while the surrounding dextran shell stabilizes the nanoparticles in solution.

The nanoparticles studied consist of a magnetic iron oxide core, surrounded by a dextran shell, with the dextran controlling the spacing between of nanoparticles (see Fig. 1). The difference between the two systems examined lies in the dextran shell (the cores are similar): the “single dextran” sample was coated once with dextran whereas the “double dextran” sample was coated twice. To properly compare these two systems their physical and magnetic properties were extensively characterized. First, the iron oxide core of both systems was determined by Mossbauer spectroscopy to be composed of magnetite (Fe_3O_4), except for < 2 % of iron hydroxide. This hydroxide most likely originates from the storage of the nanoparticles in water and is assumed to be limited to the surface of the nanoparticle core. Analytical Ultra-Centrifugation (AUC) yielded a size distribution of (44 ± 13) nm for the nanoparticle cores for the double dextran sample. Transmission electron microscopy images also confirm a core diameter ≈ 50 nm for both samples. Photon Correlation Spectroscopy (PCS) yielded a combined size and size distribution for the iron oxide core and dextran together of (92 ± 14) nm for the double dextran sample and (96 ± 32) nm for the single dextran sample. We can thus estimate the dextran thickness to be ≈ 25 nm for both samples – in good agreement with the 40,000 Da dextran used. This may indicate that the addition of the second dextran layer increases the density of the dextran coating.

From the magnetization vs. field (hysteresis) loops at room temperature of the two colloidal systems (normalized to the mass of particles present in the colloid), the most prominent result is that the saturation magnetization of the double dextran sample

¹Materials Science and Engineering Laboratory, National Institute of Standards and Technology, Gaithersburg, MD 20899

²NIST Center for Neutron Research, National Institute of Standards and Technology, Gaithersburg, MD 20899

³University of Maryland, College Park, MD 20742

⁴Triton BioSystems, Inc., Chelmsford, MA 01824

⁵Micromod Partikeltechnologie GmbH, 18119 Rostock-Warnemuende, Germany

is (41.08 ± 0.03) kA m²/g, 33 % less than that of the single dextran sample which is (61.64 ± 0.03) kA m²/g. Other than this difference in magnitude, the shapes of the two hysteresis loops are nearly identical (see Fig. 2).

The Specific Absorption Rate (SAR) values were measured for $H = 86$ kA/m (1080 Oe) and $f = 150$ kHz using colloids of nominally equal concentrations which are corrected for the thermal properties of the calorimeter, coil, and water and then normalized to iron concentration. (The iron concentration is different for the two samples, but the variation in SAR with concentration for each sample is about 10 % for the concentrations probed here.) Here we see the most striking difference – the double dextran sample has a measured SAR of 1075 W/(g of Fe) while the single dextran has a measured SAR of 537 W/(g of Fe) – a factor of 2 smaller.

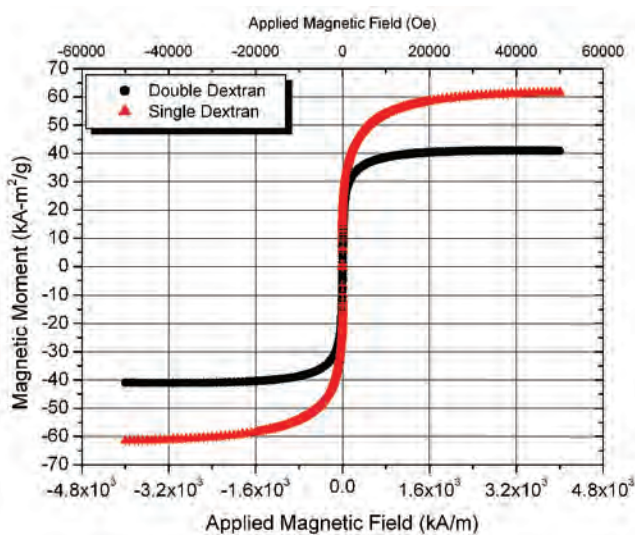


FIGURE 2: – Magnetization vs. field loops show the same shape except for a 33 % difference in saturation magnetization between the double and single dextran samples.

Since the SAR has the opposite trend from what we would expect based on the saturation magnetization data, the question is: if the nanoparticles are physically and magnetically nearly identical, what is the origin of this difference? Only Small Angle Neutron Scattering (SANS) and Ultra-SANS experiments could directly probe the separation between the nanoparticles to show that the effect of the dextran layer is to change the hard sphere interaction radius (separation) from > 698 nm for the single dextran layer to 157 nm for the double dextran layer – a factor of four smaller (see Fig. 3). This decrease in the interaction radius for the double layer is not due to a change in average diameter (as determined earlier by both AUC and PCS), nor by a change in volume fraction [1].

This smaller separation in the double dextran sample would have a two-fold effect: (1) the dipolar interactions would be significantly stronger, enabling the nanoparticles to couple their behavior under an alternating field (thereby amplifying

the heating), and (2) the smaller interaction radius would mean that more particles are grouped closer together, enhancing the local heat output in a smaller area. This increased heating effect shows significant enhancement in the efficacy of these particles in pre-clinical (mouse) trials at Dartmouth College [2], where the doubling time of the tumor – an aggressive mammary tumor – after one treatment increases to an average of 60 d from an average doubling time of 2 d for an untreated tumor.

In conclusion, we have recently determined that strongly interacting coated magnetic nanoparticles yield large increases (by a factor of two) in heat output as compared to nominally identical particles which are only weakly interacting. This heating enables larger localized temperature changes that can kill cancer cells without damaging the surrounding healthy tissue. This finding is a significant departure from “common knowledge” in the medical community, which has long contended that non-interacting magnetic nanoparticles are the ideal material for hyperthermia treatment. This interaction strength may be controlled by varying interparticle distance using different coatings, and varying the magnetic strength of the nanoparticles by nanoparticle chemistry. This result is expected to provide improved guidance to industry for the development of new nanoparticles for hyperthermia cancer treatment.

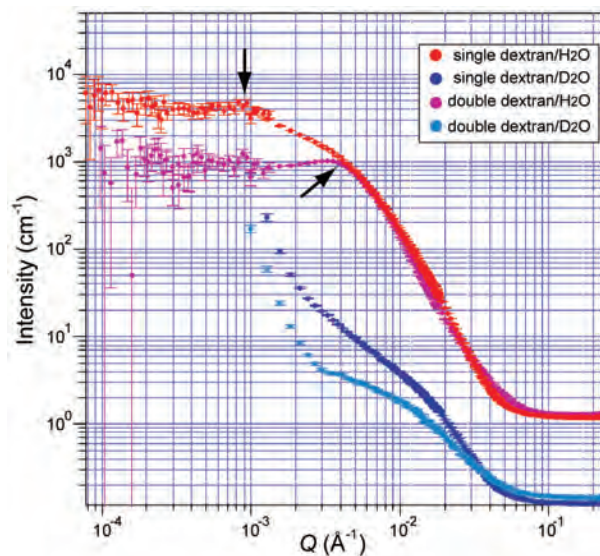


FIGURE 3: – SANS/USANS data showing the interaction peak in the double dextran sample with a concentration of 25.6 mg/ml at $Q = 4.1 \times 10^{-3} \text{ \AA}^{-1}$ (radius = 157 nm), and the possible interaction peak in the single dextran layer sample with a concentration of 21.8 mg/ml at $Q = 9.1 \times 10^{-4} \text{ \AA}^{-1}$ (radius = 698 nm).

References:

- [1] C.L. Dennis, A.J. Jackson, J.A. Borchers, R. Ivkov, A.R. Foreman, J.W. Lau, E. Goernitz, and C. Gruettner, *J. Appl. Phys.*, **103**, 07A319 (2008).
- [2] C.L. Dennis, A.J. Jackson, J.A. Borchers, R. Ivkov, A.R. Foreman, P.J. Hoopes, R. Strawbridge, Z. Pierce, E. Goernitz, J.W. Lau, and C. Gruettner, *J. Phys. D: Appl. Phys.*, **41**, 134020 (2008).

Protein Folding in Membranes

X. Han¹, K. Hristova¹, W. C. Wimley², M. Mihailescu³

In any organism, roughly a quarter of all proteins assemble into their biologically active conformation only when they are embedded in a lipid bilayer membrane [1]. The basic physical principles that drive membrane protein folding have been known for some time; the bilayer is a two dimensional fluid with a symmetric normal profile characterized by a hydrophobic (water-repelling) core and two hydrophilic bilayer-water interfaces. However the influence of transmembrane anisotropy, dynamic gradients and chemical heterogeneity on protein folding remains poorly explored. Furthermore, the degree to which proteins

understood. (Hydrophobic complementarity is a measure of how well hydrophobic regions of one molecular segment line up with hydrophobic regions on another molecular segment). Recently, neutron diffraction was used to address these questions in studies utilizing peptide model systems related to several classes of membrane proteins [2,3]. The results reveal the surprising degree to which hydrophobic complementarity can be compromised by protein-protein interactions.

The studies described here were the result of a long-standing common interest in protein folding in membranes between

the researchers at Johns Hopkins and the Tulane group which has developed peptide model systems for studying protein folding in membranes. One of these model systems, designed and studied at the Tulane lab, is a hydrophobic hexapeptide, Acetyl-Tryptophan-(Leucine)₅ (AcWL₅) that spontaneously and reversibly self-assembles in membranes into highly ordered β -sheet oligomers [4]. Although the binding and energetics of this membrane protein model are well understood, structural details of the membrane-embedded β -sheets were lacking until a study of deuterium labeled AcWL₅ oligomers in oriented bilayers using the Advanced Neutron Diffractometer/Reflectometer (AND/R) at the NCNR [3].

Previous studies of the assembly of AcWL₅ into β -sheets in membranes have provided insights into membrane protein folding. Yet, the exact structure of the oligomer in the lipid bilayer is still unknown. Based on numerous biophysical experiments, a hypothetical model was proposed in which AcWL₅ forms transmembrane antiparallel β -sheets that are centered in the hydrocarbon core in the bilayer [5]. While hydrogen bonding is known to be

the main driving force for folding of AcWL₅ in membranes, this model also contains the implicit assumption that hydrophobic

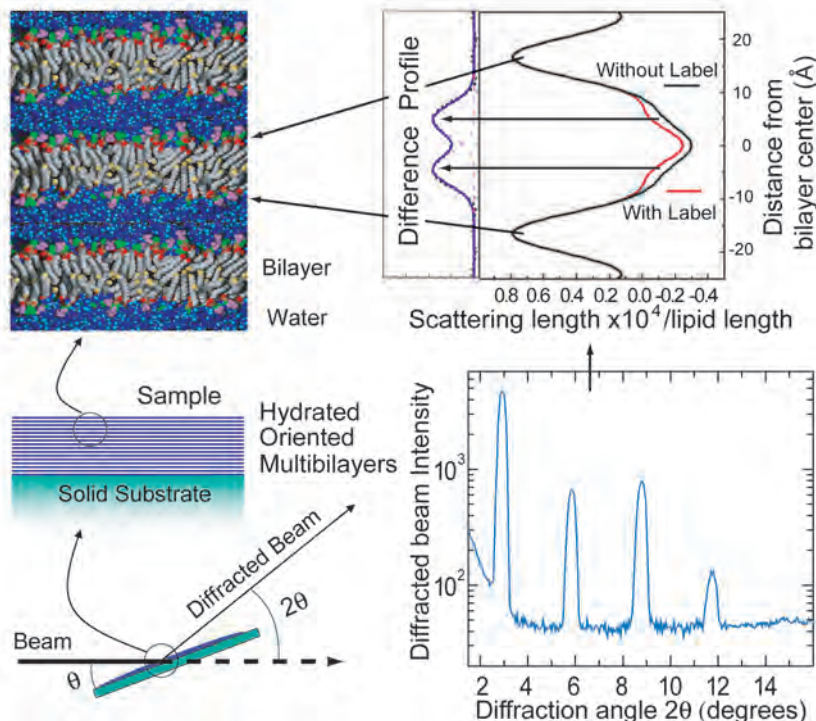


FIGURE 1: A lipid film containing 1 peptide per 25 lipids was deposited on a glass substrate and hydrated through the vapor phase to generate oriented fluid multibilayers, *left*. The oriented sample was placed in the AND/R beam, and Bragg diffraction peaks were collected in a θ - 2θ scan, *bottom*. The bilayer scattering length profiles, *upper right*, are generated from the diffraction peaks using a Fourier transform. Isomorphous replacement of lipids or peptides in the bilayer with specifically deuterated variants allows for the localization of the labels in the bilayer using difference profiles, *top*. Bilayer image courtesy of Dr. Scott Feller.

and bilayers must/can modulate their hydrophobicity profiles to achieve hydrophobic complementarity is not well

¹Johns Hopkins University, Baltimore MD 21218

²Tulane University Health Sciences Center, New Orleans, LA 70112

³University of California at Irvine, Irvine, CA 92697

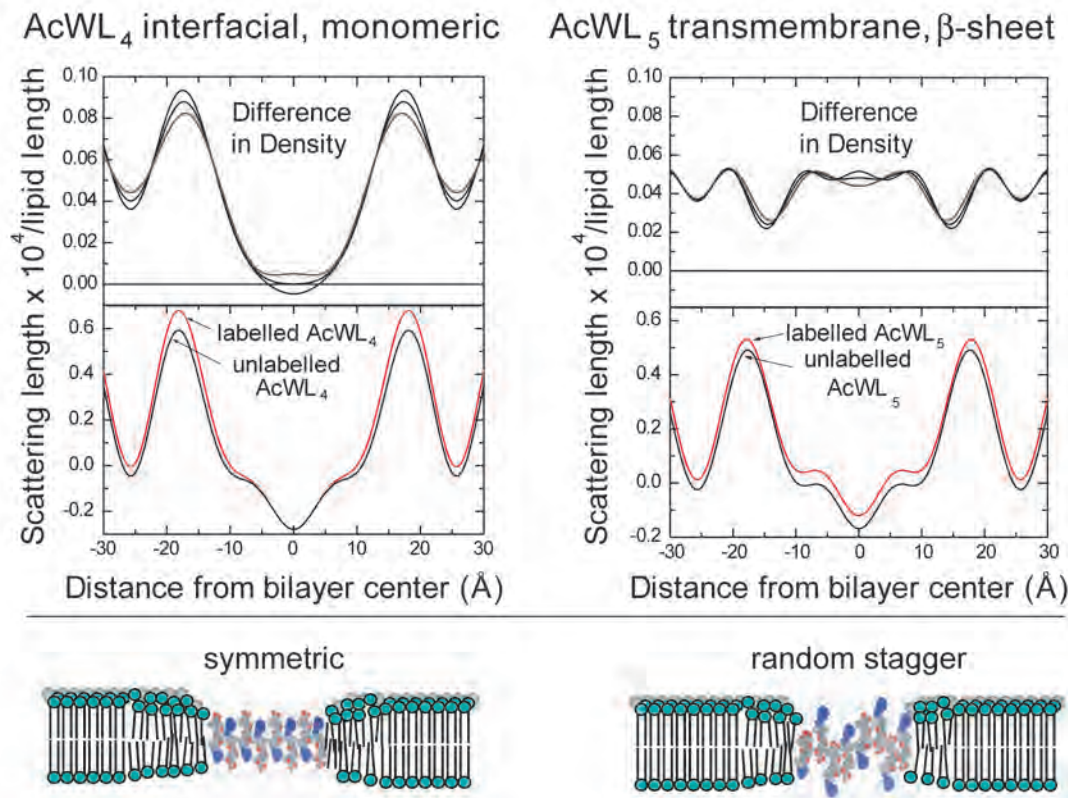


FIGURE 2: Transbilayer scattering length profiles of fluid bilayers containing either the monomeric, interfacial peptide AcWL₄, *left*, or the oligomeric, transmembrane β -sheet peptide AcWL₅, *right*. Experiments were done with 1 peptide per 25 lipids. Isomorphous replacement was achieved by substituting protonated peptide with peptide containing two consecutive deuterated leucine residues. The difference profiles, *top*, show the average location of deuterium labeled leucines in the bilayer +/- experimental uncertainty. While AcWL₄ shows the expected interfacial localization, the oligomeric AcWL₅ deuterons are present all across the membrane. Thus the transbilayer disposition of the peptide β -sheets must be randomly staggered rather than regular and symmetric as in existing models, *bottom*

complementarity drives a regular, symmetric transbilayer disposition of the peptide (Fig. 2, bottom left.) This model was tested using neutron diffraction of fluid lipid bilayers containing peptides (Fig. 1). Isomorphous replacement of peptides with variants that were selectively deuterated on two consecutive leucine residues, either the L2L3 leucines or the L5L6 leucines, was used to study the disposition of the peptides in bilayers and compare the measured distribution with that predicted by the model.

Unexpectedly, the pairs of adjacent deuterium-labeled leucines in AcWL₅ have no well-defined peak or dip in the transmembrane distribution profiles, but instead are distributed all across the membrane (Fig. 2). The result was the same for L2L3 labeled peptides and for L5L6 labeled peptides. This result indicated that there is heterogeneity in the depth of membrane insertion, implying that the β -strands are staggered along the transmembrane direction. At the same time, the monomeric homolog, AcWL₄, exhibits a homogeneous, well-defined,

interfacial location in neutron diffraction experiments and is strongly excluded from the hydrocarbon core. Thus, while the bilayer location of monomeric AcWL₄ is determined by hydrophobicity matching, or complementarity, within the bilayer, the AcWL₅ molecules in the oligomers are positioned at different depths within the bilayer because they assemble into a staggered transmembrane β -sheet. The details of AcWL₅ assembly are thus dominated by protein-protein interactions rather than by hydrophobic complementarity [3]. These results have implications for understanding and predicting the structure and folding of membrane proteins in their native membrane environment and highlight the importance of the interplay between hydrophobic complementarity and protein-protein interactions in determining the structure of membrane proteins.

References

- [1] E. Wallin, G. von Heijne, *Protein Sci.* **7**, 1029 (1998).
- [2] X. Han, M. Mihailescu, K. Hristova, *Biophys. J.* **91**, 3736 (2006).
- [3] X. Han, K. Hristova, W.C. Wimley, *Biophys. J.* **94**, 492 (2008).
- [4] W.C. Wimley, K. Hristova, A.S. Ladokhin, L. Silvestro, P.H. Axelsen, S.H. White, *J. Mol. Biol.* **277**, 1091 (1998).
- [5] C.M. Bishop, W.F. Walkenhorst, W.C. Wimley, *J. Mol. Biol.* **309**, 975 (2001).

Insights into Viral Assembly: Conformational Changes of HIV-1 Gag on the Membrane

H. Nanda¹, F. Heinrich², S. Datta³, A. Rein³, S. Krueger¹

The type 1 Human Immunodeficiency Virus (HIV-1) is responsible for the AIDS pandemic and has infected over 30 million people worldwide. Effective public health policy can play an important role in drastically reducing the spread of AIDS. However, a rise in the number of patients infected by drug resistant strains of HIV has made treatment more difficult. Patients with drug-resistant strains are often out of options and have greatly reduced life expectancies. Although treatments often involve a “cocktail” of drugs targeting different stages of the viral life-cycle simultaneously, currently there are no therapeutic agents that target the assembly stage.

Formation of HIV-1 is mediated by the viral Gag polyprotein. Expressed in the cellular cytoplasm, Gag eventually targets the inner surface of the cellular membrane of the infected host cell where viral assembly occurs. Molecular insight from early cryo-electron microscopy data showed Gag in the immature spherical virus as elongated rods radiating from the membrane with one end tightly bound to the viral genome [1]. However, in a recent study using small angle neutron scattering as well as other techniques, it was found that the properties of monomeric Gag in solution are incompatible with an extended structure [2]. Rather, Gag likely exists in several compact conformations in solution, most likely due to the presence of several unstructured, flexible domains in the protein. These results imply that the protein must undergo a large conformational change when it assembles into a virus particle. Understanding the mechanism of this conformational change would give important insights into retroviral assembly.

Our work has elucidated some of the factors that contribute to conformational changes of the HIV-1 Gag protein from a compact structure in solution to an extended structure in the immature virus. The size of Gag bound to the bilayer interface was studied in a well-defined *in vitro* system. The bio-mimetic environment for observing Gag association consisted of a supported membrane attached to a gold surface via a polymer tether. This ‘sparsely tethered’ bilayer lipid membrane (tBLM) provided a highly fluid lipid system decoupled from the solid substrate that supports it [3]. Membranes were prepared by

the rapid solvent exchange method [4]. Structural characterization of the bilayer:protein system was done by neutron reflectivity (NR) on the AND/R instrument at the NCNR [5].

Viruses acquire their membranes by budding from the host cell membrane. Lipid extracts of purified HIV-1 particles identified an abundance of lipids present only at small concentrations in uninfected cells [6]. Among these are included negatively charged, anionic lipids that are thought to associate with the n-terminal domain of the Gag protein (known as the Matrix or MA domain). Our experiments involve a simplified lipid mixture that still captures the negative surface charge density of the native viral membrane.

To test if the membrane targeting domain of Gag would associate with our model system, we first used NR to examine just the MA construct. Figure 1a shows the reflectivity curves of the neat bilayer and the membrane exposed to two different concentrations of the MA protein. Differences between the pure membrane system and the membrane with MA protein are clearly seen at the bottom of the panel. In Fig. 1b the reflectivity data were fitted using a simple box model to represent the Au substrate, tBLM and the MA domain. In this model, the MA protein is represented by a single slab of fixed neutron scattering length density (nSLD). The data indicates that the MA domain of Gag extends 40 Å from the membrane surface and that this extension is invariant with concentration.

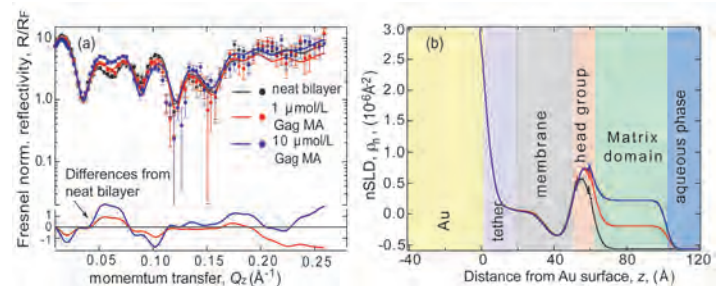


FIGURE 1: (a) Fresnel normalized neutron reflectivity profile of the pure tethered bilayer (black circles), bilayer exposed to 1 $\mu\text{mol/L}$ of Gag MA protein (red circles), and to 10 $\mu\text{mol/L}$ of Gag MA (blue circles). Fits to the experimental data are shown as solid lines. The differences in the normalized reflectivity profile between pure bilayer and bilayer with MA are shown at the bottom of the graph. (b) Neutron SLD profile that best fits the reflectivity data.

¹ NIST Center for Neutron Research, National Institute of Standards and Technology, Gaithersburg, MD 20899-8562

² Carnegie Mellon University, Pittsburgh, PA 15213

³ National Cancer Institute, NCI- Frederick, Frederick, MD 21702-1201

Because MA is a rigid domain, a fixed dimension in our NR modeling suggests that the protein binds in a specific orientation with regard to the bilayer surface, in agreement with NMR and x-ray measurements [7]. Using an atomic resolution structure of the MA domain, a refined nSLD profile was used in place of the single box representation. Figure 2a shows the volumetric and nSLD profile for MA using the suggested binding orientation from previous studies. The resulting best fit model is shown in Fig. 2b where only the volume fraction and position in z of the protein layer are free parameters. The high quality of fit to the NR data strongly suggests that the orientation of MA on the membrane is correct. These experiments also show that the volume fraction of protein, which can be related to surface coverage, doubles from 15 % to 30 %. This doubling happens while increasing the concentration of MA in solution 10-fold, hence suggesting the surface coverage of MA is saturated. Finally, it seems that MA insertion into the lipid layer is slight ($< 1 \text{ \AA}$) with minimal perturbation to the membrane structure.

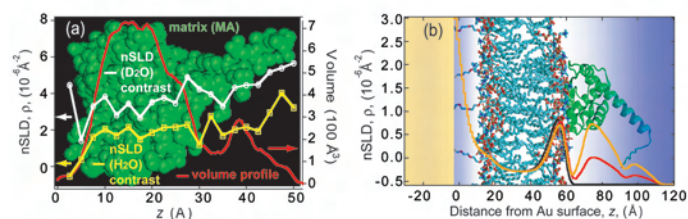


FIGURE 2: (a) Matrix (MA) domain oriented with membrane binding region on the left hand side. Volumetric profile and nSLD profiles were calculated using 2.5 Å slabs of MA along z taking into account exchangeable hydrogens on the protein. (b) Best fit nSLD profile of the tBLM system with no MA protein (black line), and bound MA protein at 1 mmol/L (red line) and 10 mmol/L (orange line) concentrations.

Having verified MA binding, measurements were made using the full length Gag protein. A series of measurements were made under different conditions thought to affect Gag conformation. 1) Purified Gag protein was introduced to the membrane and allowed to associate. 2) The bound protein was exposed to a short DNA strand (TGx7) known to bind the c-terminal nucleocapsid (NC) domain of Gag and long enough to span approximately three molecules. The NC domain is normally responsible for associating with the viral genome. 3) A high salt buffer rinse of 500 mmol/L NaCl was flushed through the system, potentially screening the electrostatically driven interactions between the protein and DNA.

Due to the lack of a well-defined structure, owing to the protein's flexible segments, modeling the full-length protein provided a difficult challenge. A series of boxes extending 240 Å from the membrane surface was used. Because of the large number of parameters introduced by our model, a Monte-Carlo error analysis was performed to determine the statistical variability

in the nSLD profiles. Figure 3a shows the nSLD profile of the different measurements where line thickness represents 95% confidence intervals in our fits. The neat bilayer is seen as the black solid line. Full-length Gag protein bound to our bio-mimetic membrane system, in red, is best modeled by an 80 Å structure from the lipid surface. Upon exposure to TGx7 the protein layer dramatically extends out to 200 Å. Finally, upon rinsing with the high salt buffer the original Gag nSLD profile is nearly recovered.

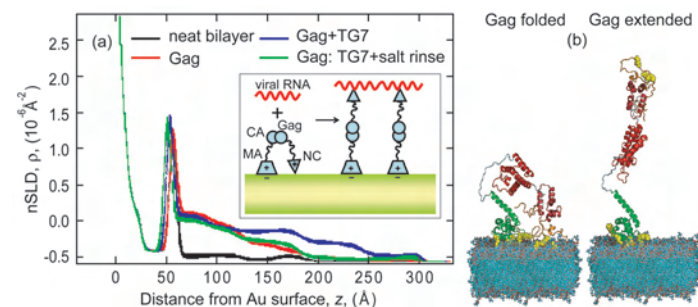


FIGURE 3: (a) nSLD profile of full-length HIV-1 Gag protein on a tBLM. Neat lipid bilayer (black), bound Gag protein (red), Gag + TGx7 DNA strand (blue), Gag: TGx7 500 mmol/L NaCl salt rinse (green). The inset cartoon illustrates how the charged ends of the Gag cause it to fold toward the surface, and then how the viral strands attach to NC, extending and crosslinking the Gag molecules. (b) Illustrative models of folded and extended conformations of Gag on a membrane surface.

This extension of Gag in the presence of both the membrane and the TGx7 nucleic acid strand provides a model for conformational changes in Gag. This model, illustrated in the inset of Fig. 3a, shows the MA and the NC domains associating with the negatively charged surface of the lipid membrane. The NC domain also contains several basic residues which aid in its association with the viral RNA. However in the absence of RNA and given the flexible regions of the protein, the NC domain is free to bend down and associate with the membrane. Only when nucleic acid of significant binding strength is present does the NC domain disassociate with the membrane and bind to the RNA strand. This causes extension of the protein molecule in part due to crosslinking several Gag molecules together. This work provides highly suggestive insight into the mechanism by which extension occurs. Our model unifies earlier in vivo and solution studies [1,2]. An understanding of virus assembly may lead to the development of therapeutics that inhibit proper virus formation.

References

- [1] S.D. Fuller, *et al.*, *Current Biology*, **7**, 729 (1997).
- [2] S.A.K. Datta, *et al.*, *J. of Molecular Biology*, **365**, 812 (2007).
- [3] D.J. McGillivray, *et al.*, *Biointerphases* **2**, 21 (2007).
- [4] B.A. Cornell, *et al.*, *Nature* **387** 580 (1997).
- [5] J.A. Dura, *et al.*, *Rev. Sci. Instrum.* **77**, 074301 (2006).
- [6] B. Brugger, *et al.*, *PNAS* **109**, 2641 (2006).
- [7] C.P. Hill, *et al.*, *PNAS* **93**, 3099 (1996).

Precision Measurement of the Spin-Dependent Neutron–Helium-3 Scattering Length (b_1)

M. G. Huber¹, F. E. Wietfeldt¹, T. R. Gentile², W. C. Chen^{3,4}, D. S. Hussey², M. Arif², L. Yang⁵, D. A. Pushin⁶, and T. C. Black⁷

Quantum chromodynamics, which describes the strong interaction between quarks, is non-perturbative, making rigorous direct calculations at low energies intractable. Instead, complex, multi-parameter theoretical models have been developed to tackle nucleon–nucleon (NN) interactions. Combinations of computational and theoretical advances in recent years have led theoretical models to predict properties of few nucleon systems with an uncertainty of less than one percent. In systems larger than two nucleons less phenomenological and more poorly understood three nucleon (3NI) interactions must be included along with NN models. Neutron scattering lengths, which describe a neutron's S -wave interaction with a target nucleus, are predicted by NN+3NI models, and therefore provide crucial benchmarks in the testing of various theoretical approaches. Scattering lengths also play an important role in effective field theories since they use low-energy observables to constrain mean-field behavior. In this highlight our measurement of the spin-dependent, incoherent neutron–helium-3 (n - ^3He) scattering length, b_1 , is described.

The NIST neutron interferometer and optics facility (NIOF) has provided measurements of neutron scattering lengths for neutron–hydrogen and neutron–deuterium, and the spin-independent scattering length for n - ^3He with relative uncertainties below one percent [1]. This is only the second experimental attempt to directly measure the spin-dependent scattering length in ^3He . The previous measurement [2] was done using a spin-echo apparatus at the Institut Laue-Langevin which achieved a result inconsistent with any theoretical prediction. Using an interferometer to measure b_1 introduces a completely separate set of systematics. This experiment marks the first time a polarized gas sample has been used in a neutron interferometer experiment.

Upstream of the interferometer a CoFe supermirror was used to polarize the neutrons to nearly 93 % polarization. The neutron's spin could be flipped 180° after the supermirror with almost 100 % accuracy using a pair of coils tuned to the neutron's Larmor frequency. After the supermirror, the

neutron's polarization was preserved by a guide field made up from a series of permanent magnets. To confirm that the neutron polarization (P_n) was not changing during the experiment, the polarization was measured periodically. This was done by replacing the interferometer with an optically thick ^3He cell which could provide analyzing power up to 99 %. Two different techniques that were used to measure P_n and the spin flipper efficiency (s) are shown in Fig. 1.

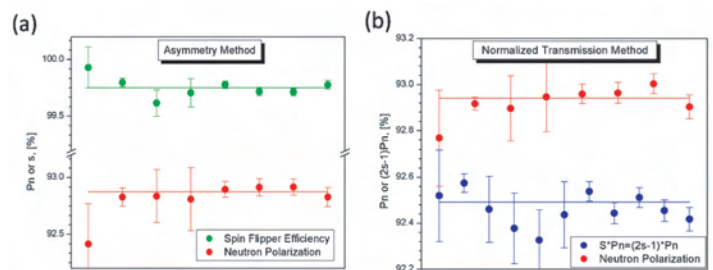


FIGURE 1: Polarization analysis using two different techniques. (a) The results from the Asymmetry Method for both the neutron polarization, P_n , and the spin flipper efficiency, s in percent versus measurement instance. (b) The polarization results using the Normalized Transmission Method. Here the spin flipper efficiency is not directly measured but instead the product $(2s-1)*P_n$ is. In both cases drawn lines are fit to the data. Both techniques agree with each other with a relative uncertainty of less than 0.001.

The NIST glass shop [3] fabricated four boron-free target cells for use in this experiment. Each cylindrical cell had outer dimensions 25.4 mm x 42 mm and was sealed with approximately 1.5 bar of ^3He gas. The cells were made optically thin to allow for some neutron transmission even during strong absorption when the ^3He and neutron spins were aligned anti-parallel. The ^3He gas was polarized to approximately 65 % using spin-exchange optical pumping at a separate facility. This procedure eliminated the added complexity and heat loads to the interferometer setup and provided the experiment with viable target samples. Helmholtz coils placed around the interferometer provided a uniform magnetic field of $15 \times 10^{-4} \text{ T}$ to limit the loss of helium polarization due to magnetic gradients. Cell lifetimes in the interferometer were up to 175 h.

The interferometer crystal is isolated from vibrations and temperature controlled to $\pm 5 \text{ K}$ which enables exceptional phase stability and contrast as high as 80 %. The skew symmetric interferometer consists of 3 silicon blades on a common base. The

¹Tulane University, New Orleans, LA 70118

²Physics Division, National Institute of Standards and Technology, Gaithersburg, MD 20899

³NIST Center for Neutron Research, National Institute of Standards and Technology, Gaithersburg, MD 20899

⁴Indiana University Cyclotron Facility, Bloomington, IN 47408

⁵Stanford Linear Accelerator, Menlo Park, CA 94025

first blade uses Bragg reflection to coherently split the neutron's wavefunction into two spatially separated paths, I and II. When a neutron passes through a ^3He cell in Path I the nuclear potential of the helium atoms causes a change in phase ($\Delta\chi$) of the neutron's wavefunction. Beams along the two paths are brought together in the final blade where they interfere with one another. Relative differences in the neutron's phase ($\Delta\chi_I - \Delta\chi_{II}$) along each path modify the count rates at two detectors, labeled O- and H-, located behind the interferometer.

A thin quartz sample called a phase flag is rotated to controllably vary the phase along the beam paths to construct an interferogram (see Fig. 2c) that is used to determine the phase of the target cell. The spin-dependent scattering length is proportional to the phase difference between when the neutron and ^3He spins are parallel to when they are anti-parallel. Boron-free glass was placed in Path II in order to compensate for the phase shift caused by the cell windows.

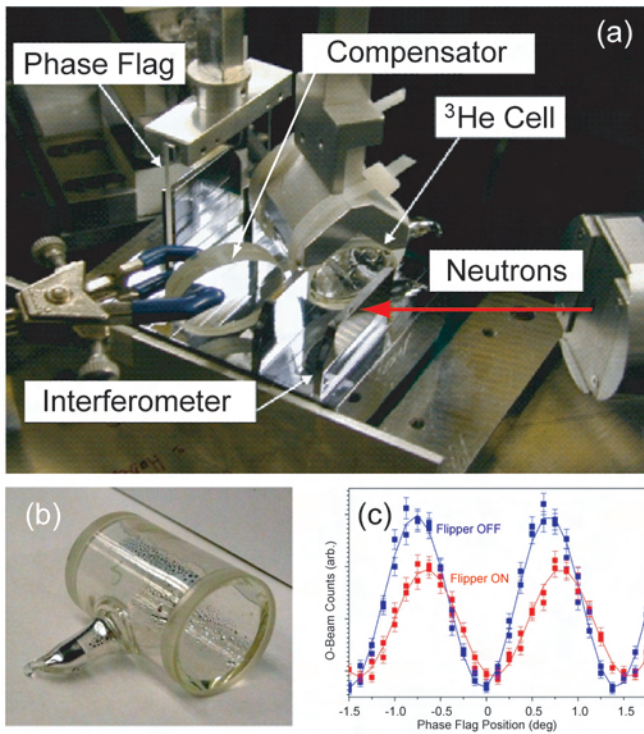


FIGURE 2: Experimental setup. (a) Neutrons enter from the right of the picture. One can see the compensation glass, the target cell, and the quartz phase flag. (b) One of the target cells used. Solid rubidium which is heated and used in Spin-Exchange Optical Pumping can be seen in the picture as dark spots along the cell walls. (c) A typical interferogram. The blue curve (lines are fits) is the O-beam intensity for when the neutron and ^3He spins are aligned parallel. The red curve is for when the neutron spin has undergone a spin flip. Lower intensity in the red curve is due to increased neutron absorption in that case. A phase shift around 30° can be seen by comparing the two curves.

The target cell's polarization was monitored throughout the experiment. A third detector labeled C4 was placed after the interferometer and directly behind the ^3He cell. C4 measured

the transmission of neutrons through the ^3He for both neutron spin states. A ratio of the count rates for both cases gave the polarization of the helium gas.

Our (preliminary) result, $b_1 = -2.410(19)$ fm, is in good agreement with the previous measurement (Fig. 3) of the spin-dependent ^3He scattering length [2]. The present result and the previous one are systematically limited by the small but nonzero spin-parallel absorption (σ_+) known only to one percent. Better experimental determination of σ_+ is needed and would greatly improve the current error bars. Known NN+3NI models do not match our results, showing the need for improved theoretical work. Four nucleon interactions are not included into the models due to the difficulty in handling long-range coulomb forces, but should constitute a tiny correction to any NN+3NI predictions. This measurement is part of the ongoing exploration into few body systems by the NIOF.

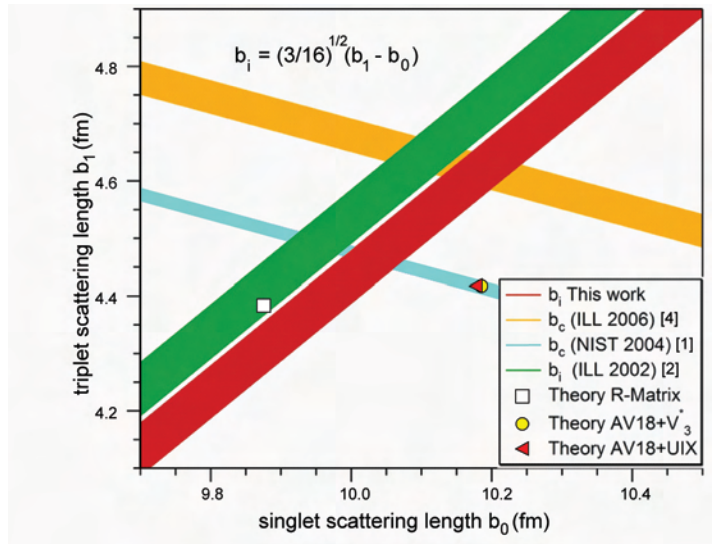


FIGURE 3: Experimental results found in [1], [2], and [4] compared with predicted values of some NN+3NI theoretical models [5]. The coherent scattering length measured in Refs. 1 and 4 is given by $b_c = 3/4 b_1 + 1/4 b_0$. The results are shown as bands representing the result \pm one standard deviation, σ .

References

- [1]. P.R. Huffman, D.L. Jacobson, K. Schoen, M. Arif, T.C. Black, W.M. Snow, and S. A. Werner, Phys. Rev. C **70**, 014004 (2004).
- [2]. O. Zimmer, G. Ehlers, B. Farago, H. Humblot, W. Ketter, and R. Scherm, Euro. Phys. J. direct A **1**, 1 (2002).
- [3]. Special thanks to John Fuller and Jeff Anderson.
- [4]. W. Ketter, W. Heil, G. Badurek, M. Baron, E. Jericha, R. Loidl, and H. Rauch, Euro. Phys. J. A., **27**, 243 (2006).
- [5]. H.M. Hofmann, and G.M. Hale, Phys. Rev. C, **68**, 021002 (2003).

Neutron Diffraction Measurement of the Load Response of Concrete

T. Gnäupel-Herold¹, H.J. Prask¹, J. Biernacki², S. Mikel²

Concrete based on portland cement is the most widely used building material in the world. Due to the importance and long history of cement-based materials, a large body of research has been assembled about behavior and properties relevant to civil engineering applications. This research includes the macroscopic response to mechanical and thermal loads and the interaction with chemical agents. However, concrete is a material of considerable complexity consisting of several phases both amorphous and crystalline, and it has structural heterogeneities such as capillary pores and micro-cracks. Currently, there is no comprehensive theory that explains the mechanical and chemo-mechanical responses associated with cement-based concretes. The advances in the simulation of concrete behavior so far are hampered by insufficient experimental data for model calibration and validation. This work is part of an extensive effort to develop experimental strategies aimed at gaining insight into how micro- and macro-scale phenomena are linked in the mechanical responses of cement-based materials under mechanical loading and drying environments.

The vast majority of cement and concrete experimental research is based on macro-level, bulk responses to stressors by means of strain gauges or other similar techniques which do not observe or explain the internal micromechanics of the system which is where failure actually originates [1]. In order to observe mechanical responses on the micro- and macro-scale, probing techniques need to be developed for obtaining quantitative measurements within these complex composites. There is much work in the fields of neutron and x-ray diffraction that demonstrates that these techniques can be used as phase resolving, non-destructive probes [2,3]. The novelty of these methods is that diffraction provides a means by which the strains within native crystalline components of the cement and aggregate can be used as internal strain gauges, thereby providing detailed information concerning the load transference mechanism(s) within and between individual components of the composite. Since the major hydrated portland cement reaction product (calcium silicate

hydrate) has an amorphous structure, suitable coherently scattering crystalline components are limited to the minority constituents calcium hydroxide (CH) and un-reacted cement phases such as tri-calcium silicate (C_3S).

In recent synchrotron experiments lattice strains were measured within the native CH phase of hydrated portland cement. Strains were induced through compressive uniaxial loading of cement samples. Proof of concept was demonstrated with a strain accuracy 1×10^{-5} and sufficient strain sensitivity for resolving the anisotropic response of different crystallographic directions in $Ca(OH)_2$ grains. However, the scope of these results was limited by the low penetration ($< 50 \mu m$) of x-rays which presents difficulties for comparing surface behavior – which is affected by wetting and drying effects – and bulk behavior that is susceptible to the same effects but on a much longer time scale.

In the research presented here, neutrons were utilized in order to investigate bulk behavior for comparison with synchrotron x-ray results as part of the multi-scale hierarchy of novel experimental results needed to gain new insight to the broader spectrum of micro and macro-scale mechanical responses in hydrated portland cement when subjected to mechanical loads. Also, due to the penetration of neutrons in the range of $10^{-3} m$ (x-ray: $10^{-6} m$) neutron diffraction provides improved volume average and grain statistics. In order to improve the substantial incoherent scattering background from hydrogen, all cement paste specimens were cured for at least one year, then machined and stored in deuterium oxide D_2O .

Two types of experiments were performed: (1) the strain response resulting from uniaxial, compressive mechanical loading; and (2) the strain response due to shrinkage induced stresses. The second was needed since the samples were kept in the $Ca(OD)_2$ -saturated D_2O until the time that the diffraction experiment began. Thus, the effects of drying became relevant since this phenomenon was occurring simultaneously during all experiments. The measured strains are lattice strains that characterize the response of crystalline $Ca(OD)_2$. In order to separate the strain responses from simultaneous drying and loading, the experiment was performed as a series of loading-unloading cycles as shown in Fig. 1.

¹NIST Center for Neutron Research, National Institute of Standards and Technology, Gaithersburg, MD 20899

²Tennessee Technological University, Cookeville, TN 38505

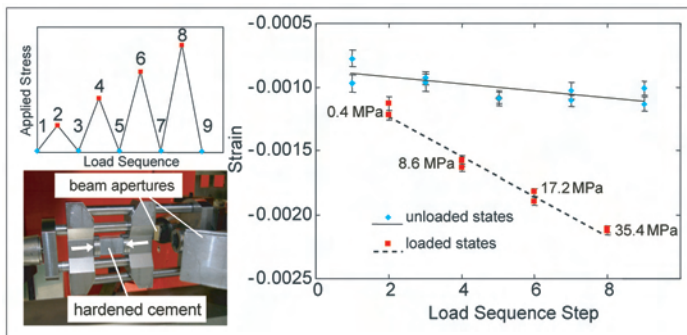


FIGURE 1: Compressive tests of cement paste prisms (10 mm × 10 mm × 15 mm) in loading-unloading cycles. The strain follows the applied load in linear dependence. However, with increasing time and water evaporation the strains in the unloaded states [0.43 MPa] become more compressive. A subsequent drying measurement of an unloaded sample during water evaporation revealed that the strains in the unloaded states exhibit a similar rate as the shrinkage strains originating from dehydration/evaporation only (Fig.2).

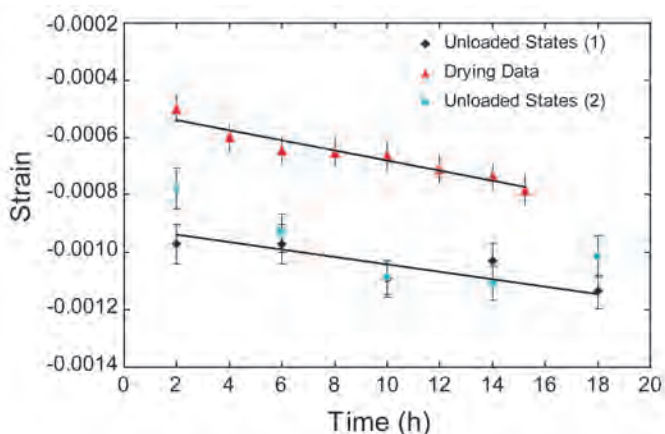


FIGURE 2: Comparison of strains from a drying test with the strains of the unloaded states. The measured $\text{Ca}(\text{OH})_2$ lattice strains characterize the behavior of a minority constituent; the behavior of the cement paste aggregate as a whole is better captured with surface attached strain gages. The comparison of suitably normalized lattice strains and macroscopic strains is shown in Fig. 3.

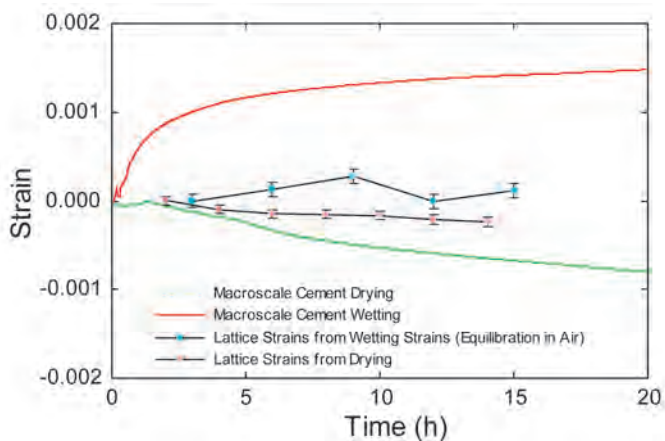


FIGURE 3: Comparison between macro-strain and lattice strain measurements for in both the wetting and drying environment. The lattice strains from wetting are for a dry sample being equilibrated in room air.

The rates of change differ substantially between macro- and lattice strains. Lattice strains represent elastic changes and as such they are a fraction of the macroscopic strain change which consists of, among other contributions, the deformation of the pore and capillary structure and the opening and closing of micro-cracks driven by hydration of hygroscopic constituents. A notable difference between lattice strains in wetting and drying is that the drying strains are decreasing and they qualitatively follow the macroscopic strains. The wetting strains are increasing but see a drop after 10 h, indicative of the very low tensile strength (compared to its compressive strength) of cement paste and the onset of micro-crack propagation and inhomogeneous stress relief. The macro-strain data in Fig. 3 represent surface strains, and their changes have different consequences for the stresses present in the bulk (where the neutron measurements are done). In wetting, the near surface regions experience swelling first which creates a tensile stress in the interior, some of which is reflected in the lattice strains from wetting. As the hydration/wetting gradient progresses deeper into the bulk, the macro-strains at the surface begin to saturate and, with the swelling now uniformly present in the bulk, the bulk tensile stresses vanish. This accounts for the drop in the lattice strains from wetting several hours later. The rate of change is much lower for the drying strains, hence lattice and macro-strains are qualitatively similar.

Overall, results obtained from neutron diffraction contribute to the growing base of experimental data that measure the mechanical response of single constituents in concrete. Such data is essential for improved understanding of the material and for advanced simulation [4] of this complex heterogeneous system.

References

- [1] R. Livingston, D. Neumann, A. Allen, S. Fitzgerald and R. Berliner, Neutron News, **11**, 18 (2000).
- [2] S. Clark and P. Barnes, Cem. Concr. Res. **25**, 639 (1995).
- [3] J. Biernacki, C. Parnham, J. Bai, T. Watkins and C. Hubbard, J. Am. Ceram. Soc., **89**, 2853 (2006).
- [4] C.J. Haecker, E.J. Garboczi, J.W. Bullard, R.B. Bohn, Z. Sun, S.P. Shah and T. Voigt, Cem. Concr. Res. **35**, 1948 (2005).

Off-Shore Oil Pipelines: Residual Stresses in Girth Welds

T. Gnäupel-Herold, H. J. Prask¹; N. Thirumalai²

Offshore oil and gas extraction plays a vital role for the global energy supply. It is expected that much future development and exploration of major reserves will take place even farther offshore and in greater depths than today. With extraction and production systems installed at depths of 2000 m to 4000 m, riser pipeline systems that are used to transfer oil or gas from the wells on the seabed to the production structure have to withstand motion due to floating vessels as well as vortex induced vibrations in the marine environment, subjecting them to the axial bending/unbending cycles that give rise to accumulating local plastic deformation (fatigue) [1]. Because of residual stresses and geometric stress concentrations, the damaging effects are concentrated in the regions of circumferential girth welds that connect individual pipe sections. Therefore, the determination of these residual stresses is essential for understanding and estimating fatigue life and for maintaining pipeline integrity.

This highlight shows our results from neutron diffraction measurements on two welds, one with a ferritic weld metal and one with a fully austenitic weld where different stress profiles are formed due to different cooling conditions, phase transformation and deformation behavior upon cooling of the weld metal. The two weld metals were chosen based on preliminary fatigue testing of full-scale pipes showing that girth welds with nickel-based weld metal exhibit improved fatigue performance [2].

Failure due to fatigue has not been of much importance in design and safety analysis of land-based pipeline systems because they are mostly subjected to static loading. However, many new oil and gas reserves are found offshore at increasing depths and distance from land with fatigue in riser pipelines arising from motion as noted above. Major factors affecting fatigue life include the yield strength of the material and, with respect to welds, the residual stress state, the applied stress, and the number of loading/unloading cycles to which they are subjected. Interest is focused on the girth welds for pipelines in general, with a number of recent neutron experiments targeting the residual stresses in the girth weld region [3,4]. It is critical to characterize the residual stress state of welds in order to develop complete mechanistic understanding of fatigue performance and to guide the fatigue design of welded joints. We measured residual stresses in the girth weld regions of two sections of X65 (minimum yield strength 451 MPa) pipe: one with ferritic weld metal and another with a fully austenitic, nickel-based alloy weld metal.

Important differences between the two weld metals are in the solidus-liquidus ranges and in the microstructure. The temperature range between the fully liquid state and the fully solidified state is between 1250 °C and 1350 °C for the austenitic weld metal and between 1500 °C and 1520 °C for the ferritic weld metal. The microstructural differences are also significant. The ferritic welds exhibit a solid state phase transition of γ -Fe (face centered cubic austenite) to α -Fe (body centered cubic ferrite) at $\approx 720^\circ\text{C}$. There is a volume expansion associated with this phase transformation that alters the residual stress generated.

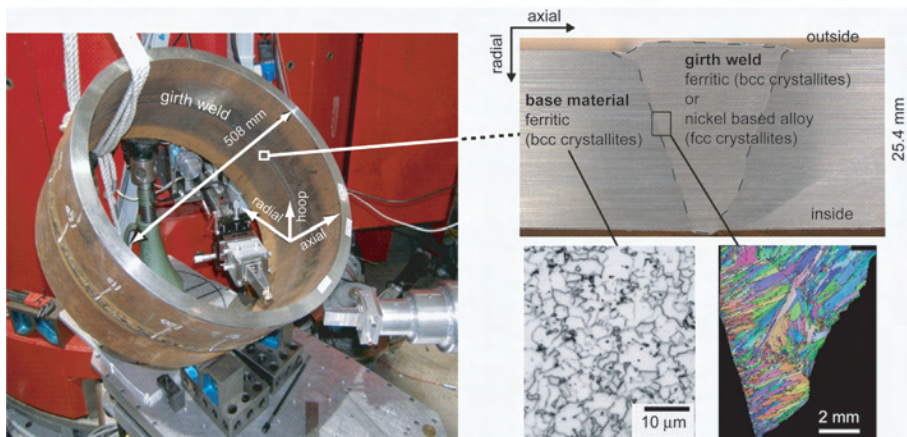


FIGURE 1: Neutron diffraction geometry for a large pipe section with girth weld in the tangential measurement direction. The right side shows the cross section of the fully austenitic girth weld and micrographs. Note the sharp boundary between the crystallographically different base metal and the weld metal (outlined by the dashed line). The micrograph for the ferritic weld metal is not shown, but grains sizes are of the same order of magnitude as the base metal.

¹NIST Center for Neutron Research, National Institute of Standards and Technology, Gaithersburg, MD 20899

²ExxonMobil Research and Engineering Company, Annandale, NJ 08801

Also, in the ferritic welds the phase transformation refines the as-solidified grain structure to small, often needle shaped crystallites with typical sizes up to 20 μm , whereas the austenitic nickel-based alloy weld metal retains the as-solidified columnar grain structure with often millimeter size grains (lower right, Fig. 1). The austenitic grains retain the face centered cubic crystal structure from solidification to room temperature, thus allowing for these large grains. As the heat transfer conditions change from weld pass to weld pass, grain growth direction and local texture change as well, which makes neutron strain measurements very difficult in the weld region.

A fundamental underlying requirement of neutron diffraction strain measurements is that the grains contributing to a diffraction peak should be uniformly distributed within the gage volume. With gage volume sizes of 3 mm \times 3 mm \times 3 mm, in the case of the austenitic weld metal with large grain size very few or no grains at all may fulfill the diffraction condition at a given specimen orientation. Therefore, the grain average has to be improved by oscillating the sample through rotation or translation such that the oscillation does not introduce additional smoothing of the strain gradient to be measured. This requirement represents a considerable challenge when confronted with a pipe section of 508 mm diameter and 25.4 mm wall thickness. For example, the specimen orientation shown in Fig. 1 allows a possible range of oscillation that is limited to a rotation of the sample table ($\pm 5^\circ$) and a small tangential translation (± 5 mm).

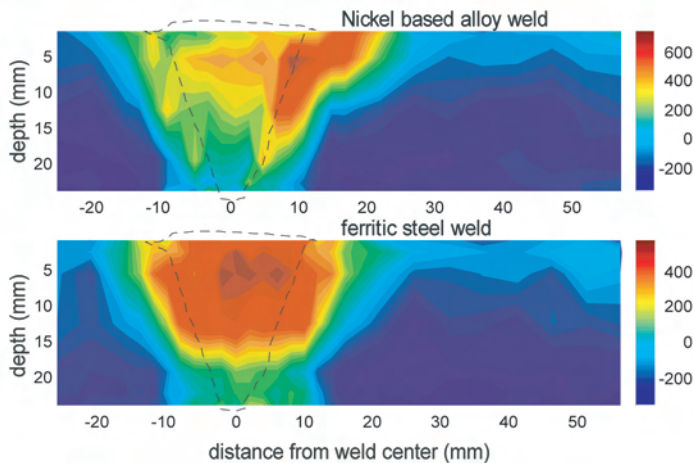


FIGURE 2: Comparison of hoop stresses between the nickel-based alloy (top) and the ferritic weld (bottom). Stress levels are given in MPa. The dashed line corresponds to the girth weld region.

The principal stresses obtained from the two pipes along the three principal directions (hoop, axial, radial) show the effects of the aforementioned differences between weld metals. Butt welds of the above shape have tensile hoop stresses (Fig. 2) that peak at the level of the yield stress. While this is the case for both weld metals, the nickel-based weld with the lower melting range shows considerably less hoop stress since it does not build up shrinkage stresses to the magnitude of the ferritic weld which has a much higher melting range.

However, this shrinkage difference is not reflected to the same extent in the axial stresses shown in Fig. 3. The near-surface tensile stress band is similar for both welds in distribution and magnitude. Both have magnitudes significantly lower than the hoop stress, thus offering a buffer to the peak tensile stresses arising from bending. However, no reduction in stress levels comparable to the hoop direction was found in the nickel alloy weld metal.

These are among the first measurements of residual stresses in full-scale thick section pipes. One result of this work is that the improved fatigue life in nickel-based weld metal compared to ferritic weld metal cannot be ascribed to a reduction in axial stress. It remains to be seen whether the explanation involves the large differences in hoop stress. Another remaining question is the role of microstructural differences in resisting fatigue crack growth. This work provides high quality experimental data which will aid in developing and calibrating finite element models for predicting residual stresses in weld joints.

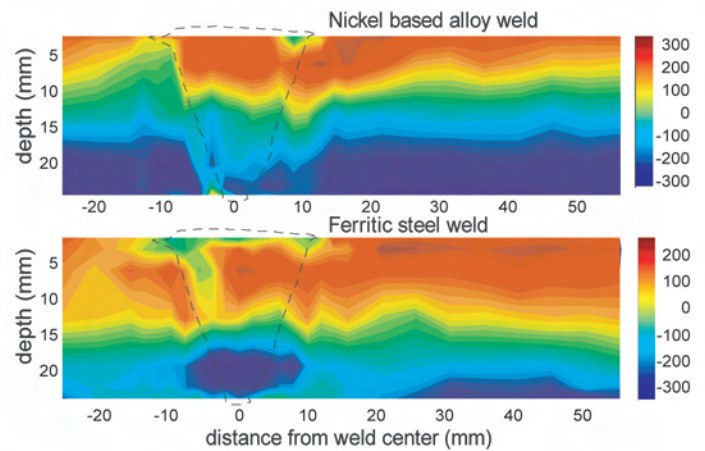


FIGURE 3: Comparison of axial stresses between the nickel-based alloy (top) and the ferritic weld (bottom). Stress levels are given in MPa. The dashed line corresponds to the girth weld region.

NT would like to acknowledge D. Lillig, M.D. Crawford and G. Dunn, ExxonMobil Development Company for providing the welded pipes used in this investigation and the support of Dr. R. Ayer, ExxonMobil Research and Engineering.

References

- [1] J. Buitrago, M.S. Weir, and W.C. Kan, Offshore Mechanics and Arctic Engineering Conference, Cancun, Mexico, OMAE 2003-37492 (2003).
- [2] D.B. Lillig, M.S. Weir, W.C. Kan and D.S. Hoyt, Deep Offshore Technology Conference, Vitoria, Espirito Santo, Brazil, (2005).
- [3] T. Gnäupel-Herold, D. Liu, H.J. Prask, *NIST Center for Neutron Research 2007 Accomplishments and Opportunities*, p 30.
- [4] M. Law, H. J. Prask, V. Luzin, T. Gnäupel-Herold, *Materials Science and Engineering A* **437**, 60 (2006).

Denser than Solid Hydrogen: Improving Hydrogen Storage

C. M. Brown,¹ Y. Liu,^{1,2} H. Kabbour,³ D. A. Neumann,¹ C. C. Ahn⁴

With the strong dependence on other countries as sources of fossil fuels, the high prices for oil, and concerns about environmental impact of using these fuels, there is intense interest in migrating to an environmentally benign, low cost alternative. One research thrust is investigating the use of clean-burning hydrogen. Specifically, one of the key engineering challenges to building a clean, efficient, hydrogen-powered car is how to design the fuel tank. Here we describe a candidate storage metal-organic-framework (MOF) material that displays high surface density for physisorbed hydrogen.

Storing enough hydrogen to allow a driving range equivalent to a gasoline powered car requires either large tanks or high pressures of gaseous hydrogen. While there are promising mechanisms for storing large amounts of hydrogen in solid materials that take up much less space than the equivalent amount of gas, there remain several roadblocks to commercialization. For instance, when stored on high surface area materials, hydrogen is weakly bound and generally requires low temperatures to achieve significant storage capacities. In order to achieve technologically relevant levels of gravimetric density, the density of adsorbed H₂ must be increased beyond levels attained for typical high surface area carbons. In this highlight we report our work showing a strong correlation between exposed and coordinatively unsaturated metal centers (CUMCs) and enhanced hydrogen surface packing density in many framework structures. In particular, we show that the MOF-74 framework structure with open Zn²⁺ sites displays the highest surface density for physisorbed hydrogen in framework structures.

A key and challenging aspect of hydrogen storage research is the ability to control the H₂ binding energy that governs the adsorption in materials ranging from microporous solids to metal hydrides. In this regard, a very attractive property of metal-organic frameworks (MOF), comprised of metal ions linked via organic ligands into porous three-dimensional solids, is that their pores can be engineered at the atomic scale, thereby enabling some control over the H₂ binding interaction. Previously we have shown that hydrogen binds

directly to the unsaturated metal coordination sites within certain classes of MOF materials. The highest observed enthalpies of hydrogen adsorption known in physisorption systems are a direct consequence of the attraction of hydrogen to these unsaturated, or open, metal sites [1]. This increase in adsorption enthalpy is necessary to increase the operating temperature of the storage medium and may ultimately result in a room temperature storage capability [2]. Despite this progress, there still remains the requirement that large amounts of hydrogen need to be stored, yet the low hydrogen surface packing density (*SPD*) of many carbon-based materials has limited their adsorption capabilities.

The metal organic framework MOF-74 resembles a bundle of hexagonally packed drinking straws with edge sharing ZnO₆ octahedra along the intersecting walls of three neighboring tubes and the remaining 'straw' composed of the organic ligand linking the metal oxide clusters. Unlike many MOF materials, MOF-74 contains exposed Zn²⁺ metal ions that can coordinate to solvents or even hydrogen. Gas adsorption studies indicate a rather large hydrogen enthalpy of adsorption of -8.8 kJ/mol, and a relatively large excess hydrogen uptake capacity of 2.8 % mass fraction for a modest surface area of 870 m²/g.

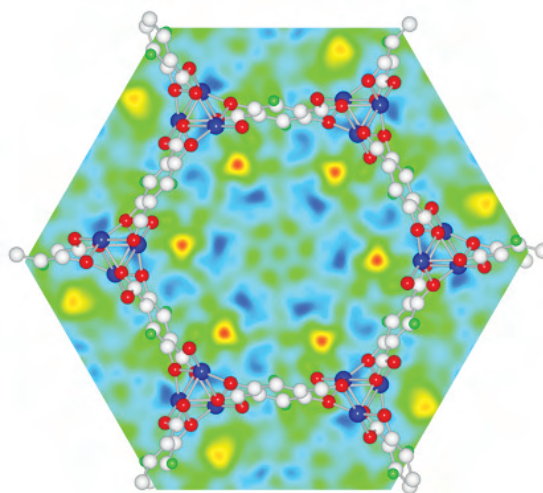


FIGURE 1: A [001] view of the real-space Fourier-difference scattering-length density superimposed with hexagonal pore structure of MOF-74, indicating the location of the first adsorption sites (red-yellow regions) and the second adsorption sites (yellow regions).

¹NIST Center for Neutron Research, National Institute of Standards and Technology, Gaithersburg, MD 20899

²University of Maryland, College Park, MD 20742

³Institut des Matériaux Jean Rouxel, CNRS-Université de Nantes, BP32229, 44322 Nantes, France

⁴California Institute of Technology, Pasadena, CA 91106

Neutron powder diffraction experiments, using the BT-1 diffractometer, were performed to understand the local H₂ environment at and around the exposed Zn²⁺ sites in MOF-74 [3]. A diffraction pattern was collected for the desolvated material prior to adding D₂. Subsequent Fourier difference mapping (Fig. 1) and Rietveld analysis indicated the existence of extra neutron scattering length density close to the Zn²⁺ ions in the framework skeleton, as expected for hydrogen initially adsorbed at the CUMC, with an interaction distance of 2.6 Å. Upon additional loading of deuterium we can further identify two more sites that generate a densely packed tube of hydrogen within the pores of MOF-74 (Fig. 2). A more detailed study of the packing geometry of the deuterium molecules reveals that the second site lies above an oxygen triangle while the third site is associated with the benzene ring of the linker with deuterium-framework distances larger than 3 Å, as is typical for the weak hydrogen interactions. Surprisingly, the second and third adsorbed deuteriums both exhibit tremendously short distances of 2.85 Å and 2.90 Å to the first adsorbed deuterium, respectively. These individual distances are much shorter than the 3.6 Å intermolecular distance found for solid D₂ under similar measurement conditions and without the application of pressure in both cases. Although the diffraction measurements were performed at 4 K, the D₂-D₂ intermolecular spacings between the first three adsorption sites shed light on the relatively large SPD in MOF-74 at 77 K.

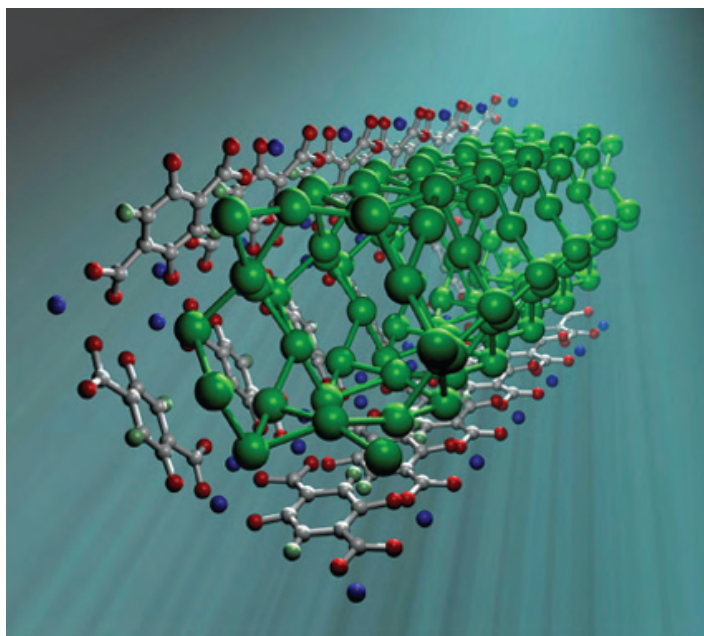


FIGURE 2: One dimensional nanoscale tube-like structure formed from adsorbed D₂. D₂ molecules [large green spheres] adsorbed in the hexagonal pores of MOF-74 [partial cross-section shown for clarity. Zn : blue, C : grey, O : red, H : pale green] form a one-dimensional nanoscale tube-like structure from the first three adsorption sites. Deuterium molecules are connected if the distance between D₂ molecules is less than 3.65 Å.

In order to evaluate the hydrogen surface density properties of different adsorbents, we use the experimental surface packing density obtained from gas adsorption studies. We can define the SPD as the saturated excess mass adsorption of H₂ per unit surface area measured at 77 K (e.g., the nitrogen derived Brunauer-Emmett-Teller ‘BET’ or Langmuir surface areas). A plot of the SPD value for MOF-74 and a selection of other framework materials is given in Fig. 3. Evidently, the presence of unsaturated metal centers in MOFs not only increases the enthalpy for hydrogen adsorption, but also allows for hydrogen molecules to be held closer together when adsorbed. Surprisingly, in the case of MOF-74 the hydrogen molecules are even closer together at 77 K than in solid hydrogen at 4 K, in agreement with the diffraction data.

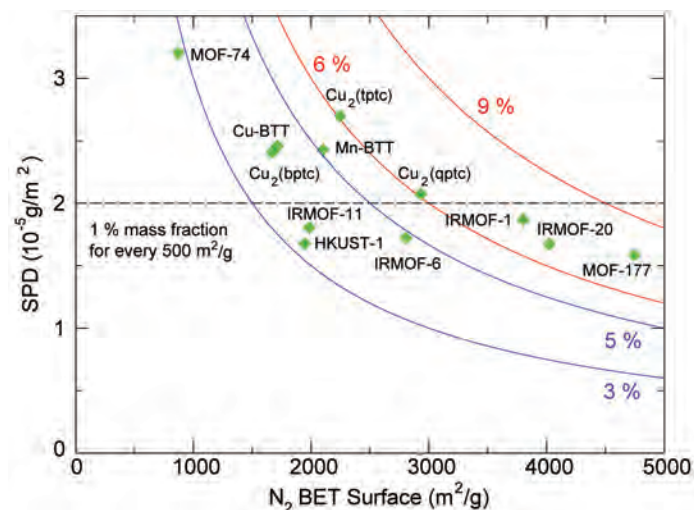


FIGURE 3: The surface packing density [SPD] of hydrogen in metal-organic frameworks is typically less than that obtained in activated carbon adsorbents [dashed black line]. MOFs with SPD values above the line contain CUMCs. Excess hydrogen adsorption capacities are indicated by the dashed blue and solid green curves.

In this study, we have demonstrated a strong correlation between exposed CUMCs in framework structures and larger associated SPD's. These observations provide an avenue to improve the gravimetric H₂ uptake by increasing the surface-packing density of hydrogen. The study of MOF-74 with neutron powder diffraction alongside isotherm measurements shows that H₂ adsorbed on the MOF-74 surface has a higher surface density at 77 K than that of solid H₂ at ≈ 4 K and zero pressure.

References

- [1] M. Dincă, A. Dailly, Y. Liu, C.M. Brown, D.A. Neumann, J.R. Long, J. Am. Chem. Soc. **128**, 16876 (2006).
- [2] S.K. Bhatia, A.L. Myers, Langmuir **22**, 1688 (2006).
- [3] Y. Liu, H. Kabbour, C.M. Brown, D.A. Neumann, C.C. Ahn, Langmuir, **24**, 4472 (2008).

Structure of $\text{Li}_2\text{Ca}(\text{NH})_2$ and Hydrogen Storage Mechanisms in the Amide-Hydride System

Hui Wu¹

Suitable hydrogen storage materials with the on-board operating capabilities for fuel-cell vehicular applications is one of the major challenges to widespread use of hydrogen as a primary fuel and to reduce dependence on fossil fuel and emissions of greenhouse gases. LiNH_2 with a hydrogen storage potential up to 10.4 % mass fraction has been viewed as a promising hydrogen storage system [1]. However, its practical application for hydrogen storage is limited because of its low hydrogen equilibrium pressure (< 0.01 bar) and high desorption temperature ($T_{\text{des}} > 320$ °C). Another feature of this system that complicates the decomposition mechanism is the competing release of ammonia from LiNH_2 at high temperature. To reduce the desorption/absorption temperatures ($T_{\text{des}}/T_{\text{abs}}$) of pure $\text{LiNH}_2/\text{Li}_2\text{NH}$, in addition to the use of catalysts and reduced particle size, several investigations have been conducted on the effects of hydride additives (LiH , MgH_2 , CaH_2) on the ratio $T_{\text{des}}/T_{\text{abs}}$ and the amount of ammonia released [2,3]. In some cases it has been claimed that the ratio $T_{\text{des}}/T_{\text{abs}}$ of the mixed amide/hydride systems can be significantly reduced compared to the results for pure LiNH_2 . However, the hydrogen storage and release mechanism of these amide/hydride mixed systems has not been established mainly due to the lack of accurate crystallographic information on the ternary imides formed after dehydrogenation.

In our recent study in $\text{LiNH}_2\text{-CaH}_2$ system [4], we have determined the crystal structure of $\text{Li}_2\text{Ca}(\text{ND})_2$ by neutron powder diffraction (NPD), and proposed a mechanism for the hydrogenation/dehydrogenation of the mixed amide and hydride system. This finding holds the key to understanding the hydrogen storage mechanism in such systems, and is critical for rational development of better candidates for hydrogen storage.

Figure 1 shows the crystal structure of $\text{Li}_2\text{Ca}(\text{ND})_2$ with D randomly distributed on one of the three sites around each N atom. In this structure each Ca is coordinated with six ND^{2-} anions forming a nearly regular $\text{Ca}[\text{ND}]_6$ octahedron with six equal Ca-N bonds (2.527 Å); each Li is bonded with four ND^{2-} anions with Li-N bond lengths in a range of

2.167 Å to 2.291 Å. The large difference in the size and coordination preference of Li and Ca drives the formation of an ordered arrangement of alternating $\text{Ca}[\text{NH}]_6$ -octahedra and $\text{Li}[\text{NH}]_4$ -tetrahedra along the *c* axis. Therefore, $\text{Li}_2\text{Ca}(\text{NH})_2$ can actually be viewed as a combined-imide structure consisting of two different imide layers. Alternatively, $\text{Li}_2\text{Ca}(\text{NH})_2$ can be described as a layered structure consisting of infinite 2D slabs of edge-shared $\text{Ca}[\text{NH}]_6$ -octahedra, which are separated by the motif of Li cations (Fig. 2), as in many “Li-intercalated” layered oxides.

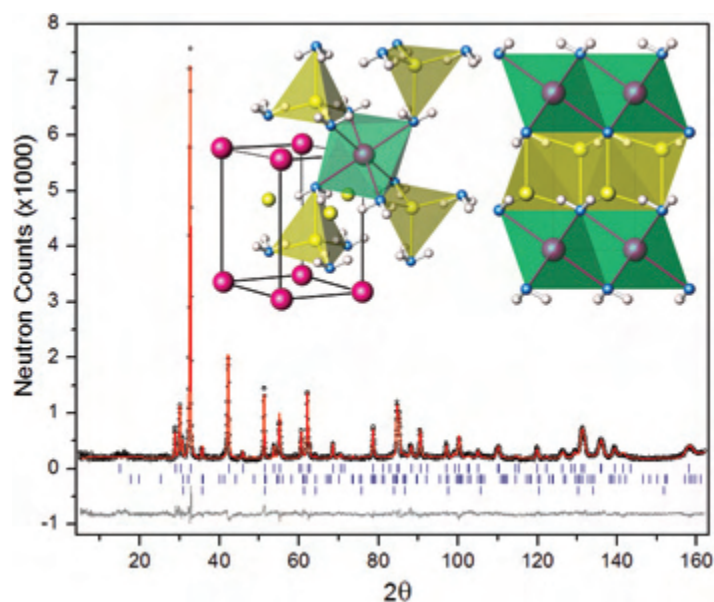


FIGURE 1: Experimental (circles), calculated (red line), and difference (grey line) NPD profiles for $\text{Li}_2\text{Ca}(\text{ND})_2$ at 15 K. The patterns also contain peaks from small amounts of LiND_2 (1.09 % mass fraction) and CaND (2.98 % mass fraction). Vertical bars indicate the calculated positions of Bragg peaks for $\text{Li}_2\text{Ca}(\text{ND})_2$, LiND_2 and CaND (from the top), respectively. $\lambda = 1.5403$ Å. Inset: (Left) off-[110] view of the trigonal structure of $\text{Li}_2\text{Ca}(\text{NH})_2$ ($P3m1$). $\text{Ca}[\text{NH}]_6$ -octahedra are in green; $\text{Li}[\text{NH}]_4$ -tetrahedra are in yellow. Ca, Li and N atoms are represented by large pink, yellow, and blue spheres, respectively. H atoms are randomly distributed at one of the three white sites around each N atom. (Right) Layered structure of $\text{Li}_2\text{Ca}(\text{NH})_2$ viewed as a “combined imide” consisting of ordered CaNH -layer and Li_2NH -layer.

To understand the formation of the $\text{Li}_2\text{Ca}(\text{NH})_2$, intermediate products at different dehydrogenation stages of $2\text{LiNH}_2 + \text{CaH}_2$ mixture were monitored using x-ray diffraction (XRD), and the hydrogen contents were determined by the prompt gamma neutron activation (PGAA) technique. In the early stage of

¹NIST Center for Neutron Research, National Institute of Standards and Technology, Gaithersburg, MD 20899-6102, and University of Maryland, College Park, MD 20742-2115

desorption the sample contains a multi-phase mixture, including CaNH , Li_2NH , CaH_2 , and LiNH_2 . Upon further desorption, CaNH , Li_2NH and LiNH_2 remain, with the continued presence of $\text{Li}_2\text{Ca}(\text{NH})_2$ and the absence of CaH_2 . After complete dehydrogenating, the product contains single-phase $\text{Li}_2\text{Ca}(\text{NH})_2$. Rehydrogenating this product results in a mixture of CaNH , LiNH_2 and LiH , differing from the initial mixture $2\text{LiNH}_2 + \text{CaH}_2$. From these results, we proposed a mechanism for dehydrogenation of the $2\text{LiNH}_2 + \text{CaH}_2$ mixture, hydrogenation of $\text{Li}_2\text{Ca}(\text{NH})_2$, and desorption of the rehydrogenated product, which we believe best explains our structure results and the chemistry of the system.

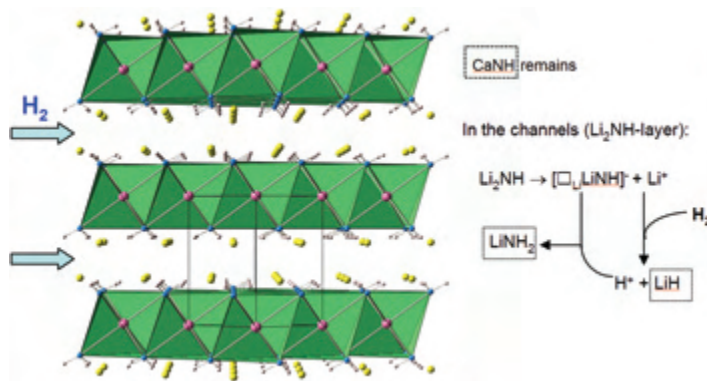
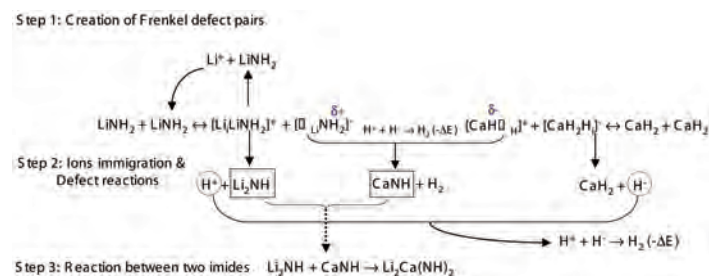


FIGURE 2: Structure of $\text{Li}_2\text{Ca}(\text{NH})_2$ viewed as an “intercalated” layered structure consisting of 2D slabs of $\text{Ca}[\text{NH}]_6$ -octahedra separated by Li ion motifs. Ca, Li, N and H atoms are colored as in Fig. 1. The facile motion of Li assists the hydrogenation process with totally 1 H_2 absorbed and final products of CaNH , LiNH_2 and LiH .

Previous study in LiNH_2 indicated the presence of Frenkel defect pairs (a charged interstitial $[\text{LiLiNH}_2]^+$ and a lithium vacancy $[\square_{\text{Li}}\text{NH}_2]^-$) and the resulting motion of Li^+ and H^+ [5]. CaH_2 with an anti- PbCl_2 structure is known as an electrolyte material with highly mobile H^- ions (also created by the Frenkel defect pair interstitial $[\text{CaH}_2\text{H}_i]^-$ and vacancy $[\text{CaH}\square_{\text{H}}]^+$). Therefore, both mobile Li^+ and H^+ in LiNH_2 and H^- in CaH_2 are involved in the dehydrogenation at high temperature. Upon dehydrogenation of $\text{LiNH}_2/\text{CaH}_2$ (see scheme 1 below), the highly mobile, free H^- anion in CaH_2 and protonic H^+ in LiNH_2 can very easily combine to create H_2 gas thanks to a very high reaction enthalpy. The fast combination of H^+ and H^- leaves $[\square_{\text{Li}}\text{NH}_2]^-$ and $[\text{CaH}\square_{\text{H}}]^+$ in LiNH_2 and CaH_2 , respectively, and drives the reaction between these two defects on the surface of adjacent particles. When these processes occur, a mixture of $2\text{LiNH}_2 + \text{CaH}_2$ will release 2H_2 in total, consistent with the hydrogen amount observed. More importantly, the participation of H^- enhances interaction between H^- and H^+ that promotes hydrogen to be released at lower temperature, and suppresses the interaction between H^+ and NH_2^- that produces NH_3 .

During hydrogenation of the layered structure $\text{Li}_2\text{Ca}(\text{NH})_2$ (Fig. 2), in the layer of Li_2NH , mobile Li^+ reacts rapidly with H_2 , forming LiH and a proton. The proton produced will then react

with the negatively charged Li-vacancy and bond with NH^- to form a NH_2^- group. In the layers of CaNH there is no mobile species, i.e., protons in NH^- groups are covalently bonded and Ca^{2+} cations are too heavy and too large to migrate. Consequently, the “inert” CaNH remains. Continuous ion movement and interactions in Li_2NH -layer will finally dissociate $\text{Li}_2\text{Ca}(\text{NH})_2$ into LiNH_2 , LiH and unreacted CaNH , as observed in our XRD/NPD results [4]. $\text{Li}_2\text{Ca}(\text{NH})_2$ could absorb H_2 at temperatures $\approx 130^\circ\text{C}$ lower than that of Li_2NH [3,4]. Considering the structural characteristics of the ternary imide, we believe that it is the special layered structure with “intercalated” mobile Li ions that is mainly responsible for the dramatically lowered T_{abs} . The facile mobility of Li within the 2D channels is also confirmed by the observed increasing nonstoichiometry at Li lattice sites with elevated temperature.



Scheme 1: Dehydrogenation of $2\text{LiNH}_2 + \text{CaH}_2$ with a total of 2H_2 released and products of CaNH , Li_2NH and/or $\text{Li}_2\text{Ca}(\text{NH})_2$ observed at various desorption steps.

In summary, the structure of ternary imide $\text{Li}_2\text{Ca}(\text{NH})_2$ was determined using NPD on a deuterated sample. $\text{Li}_2\text{Ca}(\text{NH})_2$ crystallizes in a layered structure consisting of infinite 2D slabs of edge-shared $\text{Ca}[\text{NH}]_6$ -octahedra separated by the motif of Li cations. The movement of small mobile species such as Li^+ , H^+ and H^- has been shown to play a key role in both decomposition and hydrogenation of $\text{LiNH}_2/\text{CaH}_2$. The major benefit of the participation of H^- is the enhanced interaction between H^- and H^+ that promotes hydrogen release at a lower temperature, and a reduction in the ammonia-producing interaction between H^+ and NH_2^- . The resultant ternary imide with a layered structure allows a rapid Li^+ movement, leading to a much lower T_{abs} compared to Li_2NH . Therefore, we conclude that the differently charged small mobile species are primarily responsible for the reduced $T_{\text{des}}/T_{\text{abs}}$ and for the reduced ammonia release in the mixed amide / hydride system.

References

- [1] P. Chen, Z. Xiong, J. Luo, J. Lin, K. L. Tan, Nature **420**, 302 (2002).
- [2] W. Luo and S. Sicafoose, J. Alloys Comp. **407**, 274 (2006).
- [3] Z.T. Xiong, G.T. Wu, J.J. Hu, and P. Chen, Adv. Mater. **16**, 1522 (2004).
- [4] H. Wu, J. Am. Chem. Soc. **130**, 6515 (2008).
- [5] W.I.F. David, M.O. Jones, D.H. Gregory, C.M. Jewell, S.R. Johnson, A. Walton, P.P. Edwards, J. Am. Chem. Soc. **129**, 1594 (2007).

Melilite as an Interstitial Oxygen Conducting Electrolyte

X. Kuang¹, M.A. Green^{2,3}, H. Niu¹, P. Zajdel^{2,4}, C. Dickinson¹, J.B. Claridge¹, L. Jantsky¹, M.J. Rosseinsky¹

Fuel cells date to the mid-19th century when the concept was first proposed by the Swiss chemist, Schonbein. They have been widely applied through the years, including providing both electricity and drinking water (as a by-product) in NASA space programs. As opposed to batteries which generate electricity from stored chemical energy, fuel cells generate electricity directly by electrochemically combining fuel and oxygen. Electricity is produced as hydrogen moves from the anode side to combine with oxygen moving from the cathode side. The reaction product is environmentally benign water. Although they have greatly improved since the alkali-based cells used in the Apollo space program, fuel cells are still not competitive in cost or power output with the ubiquitous internal combustion engine.

The development of more efficient systems requires the identification of new materials. The ceramic Solid Oxide Fuel Cell (SOFC) is a particularly promising variety and is characterized by very favorable power output but at the cost of high operating temperature (≈ 850 °C), a prerequisite to generating sufficient oxygen mobility. The time presently taken to heat a typical commercial fuel cell to its operating temperature is around 45 min and the US Department of Energy would like this to fall to less than 2 min. Oxide mobility in solids is associated with defects. Although anion vacancies are the charge carriers in most cases, excess (interstitial) oxide anions give high conductivities in isolated polyhedral anion structures such as the apatites. The development of new families of interstitial oxide conductors with less restrictive structural constraints requires an understanding of the mechanisms enabling both incorporation and mobility of the excess oxide.

Neutron diffraction (ND) allowed us to show how the two-dimensionally connected tetrahedral gallium oxide network in the melilite structure, $\text{La}_{1.54}\text{Sr}_{0.46}\text{Ga}_3\text{O}_{7.27}$ (Fig. 1), stabilizes oxygen interstitials by local relaxation around them, affording an oxide ion conductivity of 0.02 S cm^{-1} to 0.1 S cm^{-1} over the 600 °C to 900 °C temperature range [1].

To identify the mobile oxygen species in $\text{La}_{1.54}\text{Sr}_{0.46}\text{Ga}_3\text{O}_{7.27}$, we collected ND data on the BT-1 diffractometer at the NCNR. Refinement showed that all sites were fully occupied. Difference Fourier map calculations showed positive scattering density within the tetrahedral layers at the Ga1-Ga2 level between the La/Sr cations along the c-axis direction (labeled O4 in Figs. 1 and 2) the occupancy of which was refined to 0.136(5). The refined total oxygen content of 7.27(1) per formula unit agrees well with the oxygen over-stoichiometry obtained through other measurements. Refinement of anisotropic atomic displacement showed a considerable amount of positional disorder, presumably associated with the interstitial oxygen.

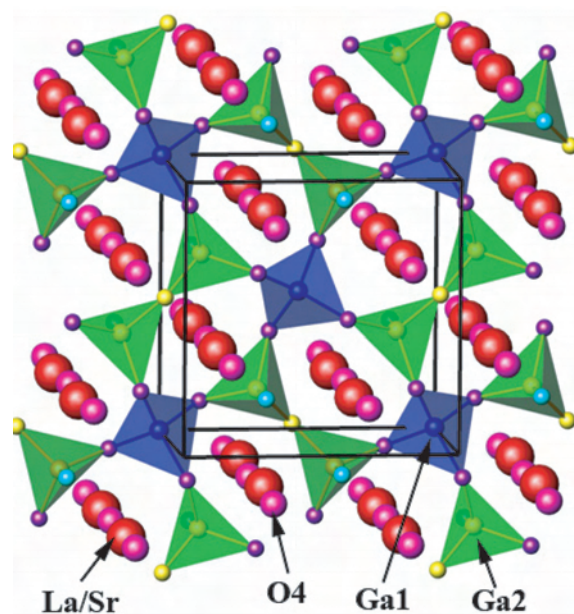


FIGURE 1: Structure of $\text{La}_{1.54}\text{Sr}_{0.46}\text{Ga}_3\text{O}_{7.27}$ which stabilizes in the melilite structure. The O4 positions indicate additional interstitial oxygen ions, not found in the parent structure.

Further, we performed maximum-entropy method (MEM) analysis, known to minimize a bias imposed by the structural model within Rietveld refinement, which confirmed the existence of the oxygen interstitial (see Fig. 2). The additional scattering density around all the atom sites is assigned to positional disorder associated with the local structural relaxations required to

¹The University of Liverpool, Liverpool, UK

²NIST Center for Neutron Research, National Institute of Standards and Technology, Gaithersburg, MD 20899

³University of Maryland, College Park, MD 20722

⁴University College London, London WC1E 6BT, UK

accommodate the interstitial oxygen.

In order to address the possible oxide diffusion pathway, a comparison can be made between the ambient and high temperature (800 °C) ND data. Rietveld refinement of the 800 °C ND data reveals the interstitial oxygen is essentially constrained around the 4e sites in the tunnels. But the thermal parameters for O4 are now extremely flattened within the layer, reflecting predominant motion within the gallate layer. The scattering density of the framework oxygen atoms shows elongation in the MEM-derived density compared with that at ambient temperature. At 800 °C, the additional scattering density in the MEM analysis is due to the gallate framework vibrational motion with no apparent additional scattering density between the neighboring O4 sites and between O4 and bulk oxygen sites. This is consistent with a direct interstitial (single particle) mechanism for the oxygen diffusion rather than the direct involvement of framework oxygen atoms.

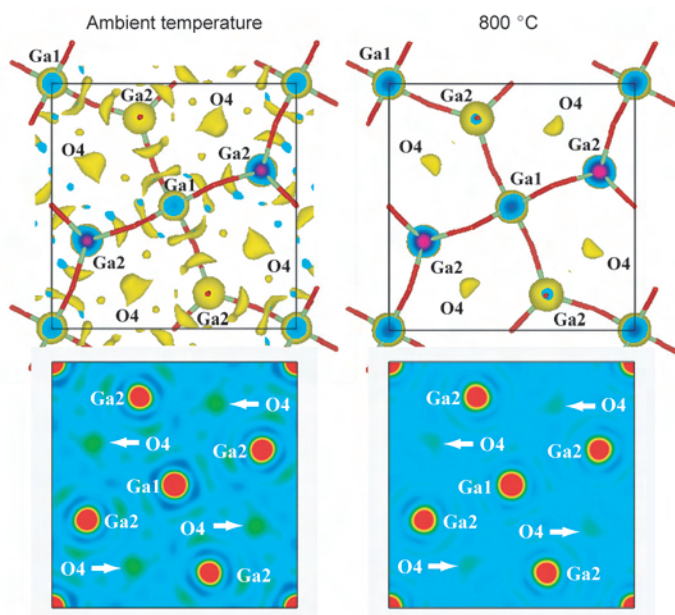


FIGURE 2: Comparison of the nuclear scattering density of $\text{La}_{1.54}\text{Sr}_{0.46}\text{Ga}_3\text{O}_{7.27}$ as obtained from maximum entropy analysis maps. The $[001]$ projections (top) and corresponding scattering density at $z = 0$ (below) are shown at ambient (left) and 800 °C (right).

A simple model for relaxation around the defect that involves those Ga2, La/Sr O1 and O3 species neighboring O4 being displaced to $(\text{Ga}2)_L$, $(\text{La}/\text{Sr})_L$, $(\text{O}1)_L$ and $(\text{O}3)_L$ sites was refined. The resulting bulk structure and the local defect structure at the O4 interstitial oxygen are shown in Figs. 3a and 3b, respectively. O4 is accommodated by the synergy of the change in bonding geometry at Ga2, modification of polyhedral internal and bridging angles, and counterion displacement. The displacement of $(\text{Ga}2)_L$ towards O4 shortens this gallium-oxygen bond from 2.13(2)Å in the average structure to 1.81(2)Å, clearly showing that the interstitial O enters the coordination environment of one of the two distinct framework gallium centers. This relaxation process shows the ability of the melilite structure to accommodate the interstitial oxygen ion via local lattice relaxation as well as to sustain oxygen mobility, which opens up many new structural families of materials as candidate interstitial oxide conductors.

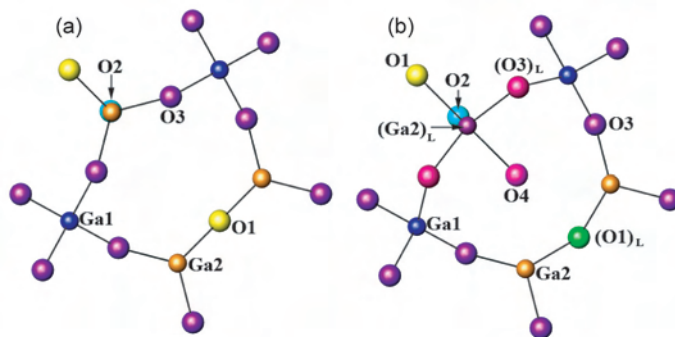


FIGURE 3: Structural relaxation around the interstitial oxide. The bulk structure (a) and local defect structure (b) around the oxygen interstitial O4. $(\text{O}1)_L$ is, unlike $(\text{O}3)_L$, not directly bound to $(\text{Ga}2)_L$ but relaxes away from interstitial O4, accommodated by a change in bond and bridging angles at Ga2. The O2 above the two Ga2 centers was omitted for clarity.

References

- [1] X. Kuang, M. A. Green, H. Hiu, P. Zajdel, C. Dickerson, J. B. Claridge, L. Jantsky and M. J. Rosseinsky, *Nature Materials* 7, 498 (2008).

Quasi-free Methyl Rotation in Zeolitic Imidazolate Framework-8 (ZIF8)

W. Zhou^{1,2}, H. Wu^{1,2}, T. J. Udovic¹, J. J. Rush^{1,2}, and T. Yildirim^{1,3}

In general, the accurate determination of interatomic potentials in solids is very challenging. However, there are cases where molecules within solids undergo sharp quantum tunneling transitions which, because they depend exponentially on these potentials, provide a stringent test of modern computational methods. Direct measurement of these transitions by neutron spectroscopy thus provides a very powerful probe of interatomic potentials. Especially rare and important are those cases where a low barrier to rotational tunneling provides exquisite sensitivity to the interatomic potential. Here we highlight our recent work on such a system, ZIF8 [1].

Zeolitic imidazolate frameworks (ZIFs) [2,3] are a recently developed class of compounds made up of MN_4 ($M = Co, Cu, Zn, \text{etc.}$) clusters linked together with imidazolate ligands to provide tunable nanosized pores. ZIF8 ($Zn[MeIM]_2$, MeIM = 2-methylimidazolate) is a prototypical ZIF compound [4]. An intriguing feature of the ZIF8 structure (Fig. 1a) is its methyl groups, bound to the imidazolate ligands (Fig. 1b). The relatively isolated methyl group in ZIF8 is oriented toward the large cavity of the porous ZIF8 structure and thus exhibits quasi-free rotation, restricted only slightly by interatomic barriers. Tunneling of the methyl groups through these barriers at low temperatures probes the interatomic potential in detail.

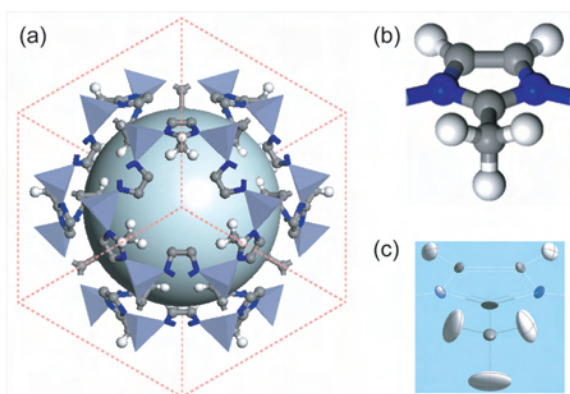


FIGURE 1: (a) ZIF8 crystal structure of (space group $I4\bar{3}m$). The 3-D open framework consists of ZnN_4 clusters (the tetrahedra) connected by 2-methylimidazolate [MeIM] linkers. The central space-filling sphere denotes the pore structure. For clarity, only the H atoms associated with the methyl groups are shown. (b) The structure of the MeIM linker. (c) The ellipsoids of the MeIM linker obtained from ZIF8 neutron-diffraction data at 3.5 K.

Neutron diffraction measurements of ZIF8 and deuterated ZIF8 (D-ZIF8) using the BT-1 diffractometer indicated that the host lattice maintains the same structure between 3.5 K and 300 K. It should be noted that the torsional amplitudes of the methyl groups are quite large (Fig. 1c), but they suggest a mainly 3-fold character for the rotational potential. Torsional energies E (≈ 2.9 meV for CH_3 and ≈ 1.7 meV for CD_3 at 3.5 K) were estimated from diffraction-derived torsional amplitudes within the harmonic approximation, (although the “harmonic assumption” is clearly questionable for large rotational amplitudes).

For 1-D rigid rotation, it is well established that the quantum rotational levels are determined by the stationary Schrödinger equation. For a free CH_3 rotor, the $J = 0 \rightarrow 1$ transition energy (splitting of the ground state rotational level) is equal to 0.655 meV. For a non-zero rotational barrier, this transition energy decreases with increasing barrier height. To quantitatively probe the methyl-group rotations, we measured the $0 \rightarrow 1$ rotational transition of ZIF8 by neutron spectroscopy at 334 ± 1 μeV (Fig. 2). The lack of mode-splitting indicates little methyl-methyl coupling. The corresponding CD_3 tunneling transition in D-ZIF8 was measured with both the HFBS and DCS spectrometers at 33 ± 1 μeV (at much lower energy due to the $2\times$ -higher CD_3 moment of inertia compared to CH_3). Additional DCS measurements for ZIF8 showed a broad peak at $\approx 2.7 \pm 0.1$ meV, which we tentatively assigned to the $J = 0 \rightarrow 2$ level, although framework modes could also contribute here. If we assume a pure 3-fold barrier to rotation, the 334 μeV tunnel splitting for ZIF8, combined with a second rotational level of 2.7 meV, predicts a very low barrier height of 6 meV. The 33 μeV tunnel splitting for D-ZIF8 suggests a slightly higher barrier of about 8 meV for the CD_3 groups.

At higher temperatures (≈ 30 K and above), the tunneling gives way to classical jump reorientation as the peaks shift toward the elastic line and broaden (Fig. 2 inset). Figure 3 shows the temperature dependence of the quasielastic linewidths (Γ) for ZIF8 plotted in an Arrhenius fashion. The activation energy E_a for 3-fold jump reorientation can be estimated from the slope under the assumption that the methyl groups reorient through a jump diffusion process by thermal activation over the barrier.

¹NIST Center for Neutron Research, National Institute of Standards and Technology, Gaithersburg, MD 20899

²University of Maryland, College Park, MD 20742

³University of Pennsylvania, Philadelphia, PA 19104

The transformation from 3-fold jump to rotational diffusion is manifested by the nonlinear nature of the Arrhenius plot with increasing temperature. We estimated an activation energy of ≈ 3 meV from the slope associated with the data between 30 K and 40 K. (At higher temperatures (> 50 K), this model loses its validity as the thermal energy is comparable to the barrier height.) Further assuming that this E_a was a measure of the distance from the first-excited rotational ($J = 2$) level (tentatively assigned at 2.7 meV) to the top of the potential barrier, and estimating a zero-point energy of $\frac{1}{2}(2.7 \text{ meV})$, led to a barrier height of about 7 meV, close to that predicted above for a 3-fold potential.

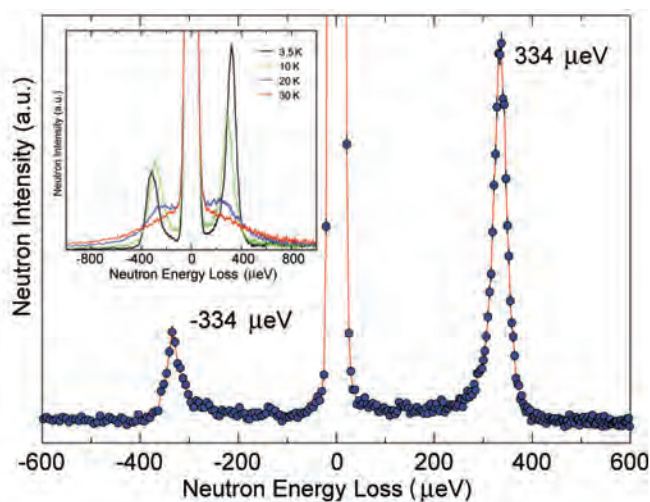


FIGURE 2: ZIF8 tunneling spectrum at 1.4 K using the DCS spectrometer with 7 Å neutrons ($\approx 18 \mu\text{eV}$ resolution). [inset] Evolution of the tunneling spectrum with temperature using the FCS spectrometer with 6 Å neutrons ($\approx 70 \mu\text{eV}$ resolution).

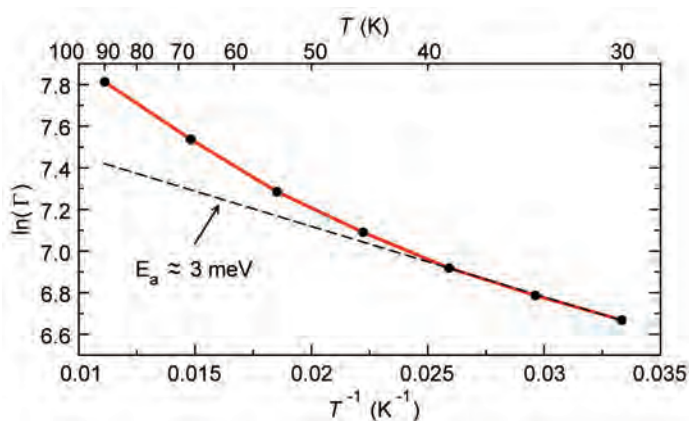


FIGURE 3: A plot of $\ln(\Gamma)$ vs. T^{-1} for ZIF8 between 30 K and 90 K, where Γ [in μeV] is the full-width-at-half-maximum quasielastic linewidth.

To obtain further insight, we calculated the rotational barrier using density functional theory (DFT). From the optimized structure, we performed total-energy calculations as a function of the rotational angle of the methyl group. For simplicity, we only rotated one methyl group in the unit cell. Interestingly, the calculated results (Fig. 4), which can only be considered qualitative, predict a shape of the potential that includes both 3-fold and smaller 6-fold terms and a barrier height of ≈ 6.6 meV, consistent with the value determined from the various neutron scattering measurements.

Thus, all the results of our study show the existence of an unusual (for a solid) quasi-free rotational potential for CH_3 groups in ZIF8. The high methyl-group tunneling energies and low hindered rotational transitions combined with the results of quasielastic neutron scattering provide a rotational barrier of about 7 meV, largely 3-fold and consistent with first-principles calculations. Two previous examples of quasi-free methyl rotation are 4-methyl pyridine [5] and Li acetate dehydrate [6], which have high tunneling transitions and low rotational barriers. Yet, both show methyl-methyl coupling effects, which result in complex tunneling spectra. In contrast, the ZIF8 spectrum shows no evidence of sidebands, which indicates “independent” rotation of CH_3 groups and therefore provides a “textbook” example of rotational tunneling in a low-barrier system.

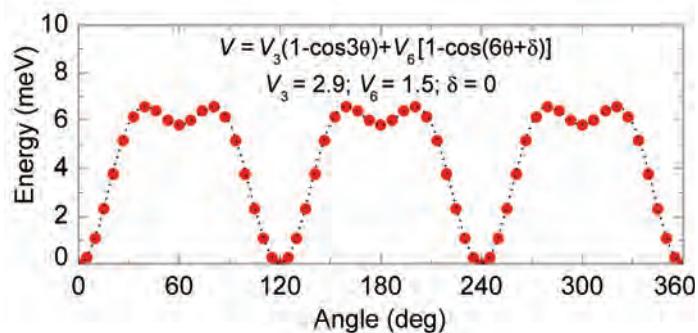


FIGURE 4: Rotational potential of the methyl group in ZIF8, obtained from DFT calculations. Dotted lines are the fit to a 3-fold/6-fold mixed potential.

References

- [1] W. Zhou, H. Wu, T. J. Udovic, J. J. Rush, T. Yildirim, J. Phys. Chem. A (submitted).
- [2] X. C. Huang, Y. Y. Lin, J. -P. Zhang, X. M. Chen, Angew. Chem. Int. Ed. **45**, 1557 (2006).
- [3] K. S. Park, Z. Ni, A. P. Cote, J. Y. Choi, R. Huang, F. J. Romo, H. K. Chae, M. O’Keefe, O. M. Yaghi, Proc. Natl. Acad. Sic. U.S.A. **103**, 10186 (2006).
- [4] H. Wu, W. Zhou, T. Yildirim, J. Am. Chem. Soc. **129**, 5314 (2007).
- [5] B. Nicolai, A. Cousson, F. Fillaux, Chem. Phys. **290**, 101 (2003).
- [6] F. Fillaux, C. J. Carlile, G. Kearley, J. Phys. Rev. B **58**, 11416 (1998).

Understanding the Origin of Toughness in Double-Network Hydrogels

S. Lee, V. R. Tirumala, T. Tominaga, E. K. Lin, W.-L. Wu¹; M. Nagao^{2,3}

Recent advances in the synthesis of hydrogels have resulted in materials with fracture toughness comparable to that of articular cartilage [1]. The toughness arises from the combination of a stiff but brittle crosslinked polyelectrolyte (poly-2-acrylamido-2-methyl-1-propanesulfonic acid, PAMPS) and a soft and pliable neutral linear polymer (polyacrylamide, PAAm). This class of hydrogels has been named double-network hydrogels (DN-gels). Although many polymer pairs have been tested, only a few give rise to hydrogels with superior toughness. This observation suggests that some specific composition-dependent associations between polymer pairs in the DN hydrogel may play an important role in shaping the toughness of DN-gels.

In our previous work, small angle neutron scattering was used to measure the molecular structure of DN-gels under static conditions as well as under deformation [2, 3]. The surprising outcome of these experiments is that both the PAMPS and the PAAm become more homogeneous when in the presence of each other than in pure water by themselves. This result suggested that there could be associations such as hydrogen bonding between the charged and uncharged molecules [4]. We further noticed that even within DN-gels made of PAMPS and PAAm, only those with a volume ratio near 1:7 (PAMPS : PAAm) exhibit extraordinarily tough mechanical strength [2]. This result suggests that the interchain association strength depends not only on the chemical structure of the constituents but also on the molar ratio between these two components.

In order to clarify the nature and the origin of interchain associations between PAMPS and PAAm, we performed a neutron spin-echo (NSE) study to determine the chain dynamics over a broad scale of frequency and length in the PAMPS and PAAm solution blends. The solution blends were prepared by mixing linear polymer solutions of PAMPS and *d*₃PAAm at various volume ratios. Pure PAMPS and *d*₃PAAm solutions were prepared by UV-initiated free-radical polymerization of their monomers in D₂O with 2-oxoglutaric acid. By adjusting the ratio between D₂O and H₂O, we

brought the neutron scattering contrast between *d*₃PAAm and the solvent to zero, thus the dynamics of PAMPS chains could be measured using NSE. In this study, the total polymer concentration of the mixtures is kept constant (0.5 mol/L) while the concentration of PAMPS and PAAm are varied (PAMPS: (0.375, 0.125, 0.0625, 0.03125) mol/L). NSE measurements were conducted at 25 °C on the NG5-NSE beamline at the NCNR using a 6 Å wavelength incident beam.

Figure 1 shows the intermediate scattering functions for the pure 0.5 mol/L aqueous PAMPS solution. Over the entire *q*-range the results can be modeled as a single exponential function, i.e., the relaxation time ($\tau_{aa}(q)$) can be obtained by fitting the equation

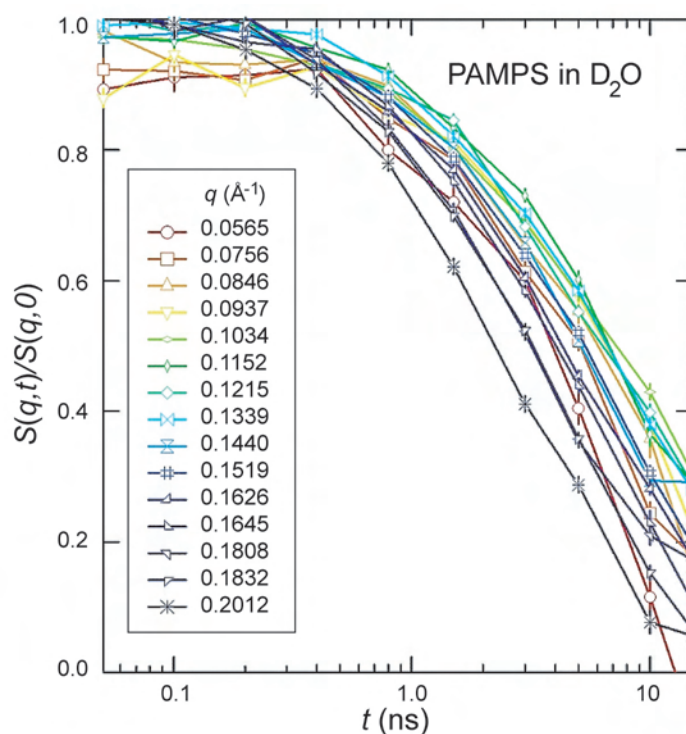
$$\frac{S_{aa}(q,t)}{S_{aa}(q,0)} = A \exp(-t/\tau_{aa}(q)).$$


FIGURE 1: Partial intermediate scattering function of PAMPS in 0.5 mol/L PAMPS solution.

In all solution blend samples, the intermediate scattering functions are also single exponential functions similar to that of

¹Polymers Division, National Institute of Standards and Technology, Gaithersburg, MD 20899

²NIST Center for Neutron Research, National Institute of Standards and Technology, Gaithersburg, MD 20899

³Indiana University Cyclotron Facility, Bloomington, IN 47408

the pure PAMPS solution. This observation indicates that the presence of neutral polymers does not induce any unexpected dynamics of the PAMPS chain over all the q -range probed. The q -dependent relaxation spectrum of PAMPS chain in PAMPS/ PAAm solution blends seems to follow qualitatively the static structure $S_{aa}(q)$ measured by small angle neutron scattering (SANS). However, it is interesting to note that the relaxation time measured at the lowest accessible $q \approx 0.05 \text{ \AA}^{-1}$ (Fig. 2) exhibits a maximum in the solution blend with 0.0625 mol/L PAMPS. This result is surprising since the static structure revealed by SANS does not exhibit an anomaly at this composition; the normalized low q intensity of SANS simply increases gradually with a decrease in PAMPS concentration [2]. The slower relaxation at 0.0625 mol/L PAMPS concentration is significant because it is close to the PAMPS:PAAm ratio at which a maximum in the toughness of DN-gels was observed [2]. Using the experimentally measured q -dependent relaxation time, the static structures measured by SANS, and Akcasu *et al.*'s theoretical model [5] for chain dynamics in a multi-component polymer solution, we calculated the effective solvent viscosity. Again, the effective solvent viscosity for the PAMPS chain within the solution blends exhibits a maximum at the 0.0625 mol/L PAMPS concentration (Fig. 3). It is noteworthy that the high q portion of the data of the relaxation spectrum dictates the value of the effective viscosity, whereas the result given in Fig. 2 arises from just the low q data. The above observation suggests that the interchain association between PAMPS and PAAm manifests itself throughout the entire q range probed by NSE.

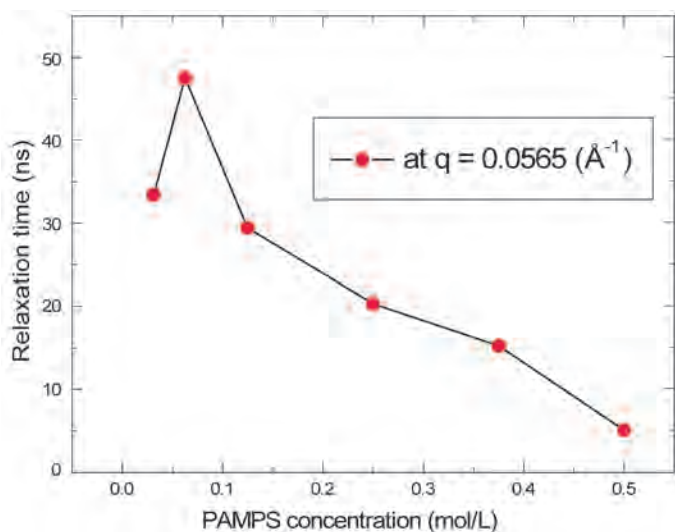


FIGURE 2: A maximum in the relaxation time of PAMPS (τ_{app}) is observed to locate at a PAMPS/ PAAm molar ratio of 1 to 7. [The line is a guide to the eye.]

In summary, both the relaxation time at the large length scale and the segmental diffusion coefficient / the effective solvent viscosity at the short length scale measured by NSE in PAMPS/PAAm solution blends are in accord with the rheological and mechanical behavior of the PAMPS/PAAm double network hydrogels. To the best of our knowledge, this work represents one of the first NSE measurements of polyelectrolyte solutions containing neutral polymer. The NSE results can be modeled adequately with the mean-field theory of Akcasu *et al.* [5] after it was modified to include polyelectrolytes.

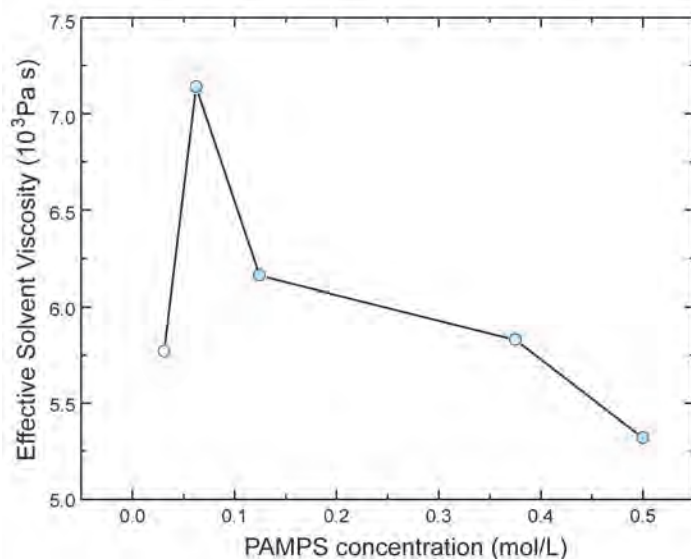


FIGURE 3: Effective solvent viscosity seen by PAMPS segment within PAMPS/PAAm solution blends. A maximum is also located at a PAMPS/ PAAm molar ratio of 1/ 7. [The line is a guide to the eye.]

References

- [1] J. P. Gong, Y. Katsuyama, T. Kurokawa, Y. Osada, *Adv. Mater.* **15**, 1155 (2003).
- [2] T. Tominaga, V. R. Tirumala, E. K. Lin, J. P. Gong, H. Furukawa, Y. Osada, W.-L. Wu, *Polymer* **48**, 7449 (2007).
- [3] T. Tominaga, V. R. Tirumala, S. Lee, E. K. Lin, J. P. Gong, W.-L. Wu, *J. Phys. Chem. B* **112**, 3903 (2008).
- [4] Y. D. Zaroslov, V. I. Gordeliy, A. I. Kuklin, A. H. Islamov, O. E. Philippova, A. R. Khokhlov, G. Wegner, *Macromolecules* **35**, 4466 (2002).
- [5] A. Z. Akcasu, "Dynamic Light Scattering. The Method and Some Applications" W. Brown, ed.; Oxford University Press: London, (1992).

Nanoparticle-directed Self-assembly of Block-copolymers: Measurement of 3D Order

K. G. Yager¹, B. C. Berry¹, K. Page¹, D. Patton¹, R. Jones¹, A. Karim¹, B. Akgun², S. Satija², P. Butler², E. J. Amis³

Self-assembly is a promising route for creation of high-fidelity and high-density nanostructures but many questions regarding the fundamental behavior of self-assembly remain unanswered. Quantifying the three-dimensional order of self-assembled nanostructures, especially in the interior of thin films, remains challenging. We present a simple and robust strategy for directing the self-assembly of block-copolymers. The technique uses nanoparticles with tunable surface energy (via ultraviolet-ozone (UVO) oxidation), cast onto flat substrates, where the spin-casting conditions can be tuned to control roughness. These surfaces can induce block-copolymer lamellae to orient either parallel or perpendicular to the substrate. In order to quantify the order within these thin films, we used rotational small-angle neutron scattering in combination with neutron reflectometry to reconstruct the sample reciprocal space. We demonstrate that by carefully modeling the data, we can extract quantitative information regarding the angular distribution of lamellae.

Block-copolymers are an archetypal self-assembling system, and are being actively pursued for a variety of applications, from microporous membranes to lithographic resists [1]. Crucial to many applications is control of the orientation of the well-ordered phases that develop in block-copolymers during annealing. Hashimoto and collaborators [2] demonstrated the use of rough substrates to bias the orientation of block-copolymer assembly. Building upon this work, we investigated the use of nanoparticle surface treatments as a means of generating substrates of controlled roughness. In particular, spin-casting conditions (solution concentration and spin speed) can be used to control the roughness of the resulting layer. The organic-coated silica nanoparticles (20 nm diameter) are amenable to UVO oxidation treatment, which converts the hydrophobic particles to hydrophilic. Thus, the average surface energy can be tuned over a wide range by UVO exposure time. This dual control of roughness and surface energy allows us to select the substrate conditions most conducive to a desired kind of self-assembled order.

We investigated the well-studied lamellar-forming block-copolymer polystyrene-poly(methyl methacrylate) (PS-PMMA). By casting a film thickness gradient of copolymer over the nanoparticle substrate, we were able to investigate the interplay between film thickness and substrate interactions. Remarkably, we discovered that the surface orientation of lamellae cast on the rough nanoparticle substrates oscillated with film thickness (see Fig. 1). Atomic force microscopy indicated that the orientation of lamellae at the surface was horizontal for some thicknesses (lamellae sheets lying parallel; flat along substrate and air interfaces) and vertical for others (sheets perpendicular; ‘standing up’ with respect to the substrate). This theoretically-implicated, but now experimentally verified, oscillation between orientations points to the key role of film confinement and interfacial interaction in determining the final order. However, atomic force microscopy measurements are fundamentally limited to measuring surface morphology, and cannot probe within a thin film. For instance, the fingerprint pattern assigned as ‘vertical lamellae’ in Fig. 1 could conceivably arise from a section through a randomly-orientated lamellar phase.

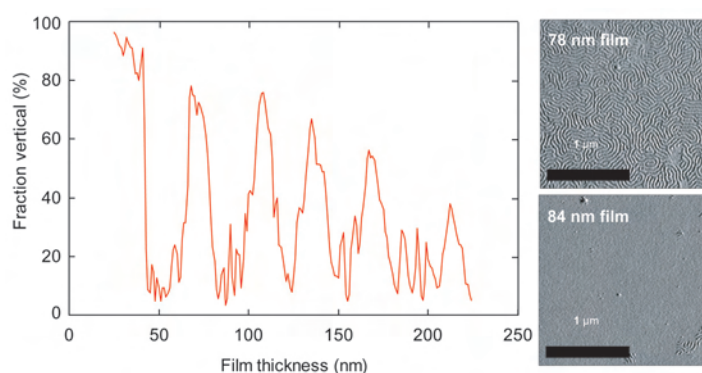


FIGURE 1: As a function of film thickness, the orientation oscillates between vertical and horizontal states. Typical atomic-force micrographs of ‘vertical’ (top) and ‘horizontal’ (bottom) lamellae orientations formed on nanoparticle-roughened substrates.

Neutron scattering measurements can provide the missing information about the internal arrangement of nanostructured thin films. We used semi-deuterated block-copolymers, where one block has hydrogens replaced with deuteriums, which scatter neutrons strongly and yield characteristic patterns in a small-

¹Polymers Division, National Institute of Standards and Technology, Gaithersburg, MD 20899

²NIST Center for Neutron Research, National Institute of Standards and Technology, Gaithersburg, MD 20899

³Materials Science and Engineering Laboratory, National Institute of Standards and Technology, Gaithersburg, MD 20899

angle neutron scattering (SANS) geometry. We further employed the ‘rotational SANS’ variant, whereby we acquire a scattering image across a wide range of sample rotation angles. Each angle measures a ‘slice’ through the three-dimensional reciprocal space of the sample, and the angular sweep thus reconstructs the full reciprocal space. Since the scattering pattern at each angle arises from periodic order along a particular plane in the sample, the reconstructed reciprocal space in principle contains information about the order in every possible orientation. Figure 2 shows a Q_x - Q_z slice through the reconstructed sample reciprocal space, for three representative thin films. The z -axis points along the sample normal, with the sample lying in the xy -plane. Scattering intensity along the x -axis thus originates from in-plane periodic structures, whereas intensity along the z -axis originates from nanostructures whose periodicity is along the film normal. The Q_x - Q_z slices provide information about the range of lamellae orientations from vertical to horizontal (note that the y -direction is essentially identical to the x -direction since the samples had no preferred in-plane direction). The peak at $Q_x = 0.16 \text{ nm}^{-1}$ occurs due to vertical lamellae, whereas the scattering intensity near the Q_z axis arises from horizontal lamellae. Importantly, the data allow us to rule out a completely random internal arrangement of lamellae, since this would lead to uniform isotropic scattering for all $Q = \sqrt{Q_x^2 + Q_z^2} = 0.16 \text{ nm}^{-1}$. It is also clear that the extent of vertical order is affected by film thickness. A small variation in the thickness of the film causes the vertical peak to nearly disappear.

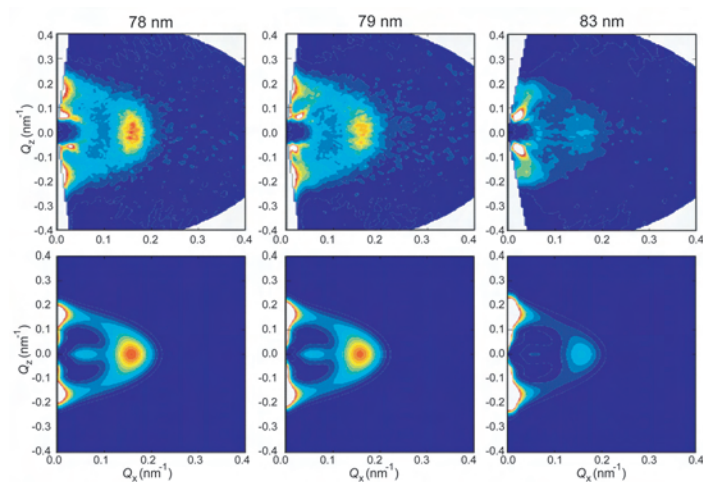


FIGURE 2: Rotational SANS reciprocal-space reconstructions for three different film thicknesses (top row) show varying intensity of the vertical peak. The associated best-fit models (bottom row) provide insight into the angular distribution of the lamellae.

We can quantify the order by fitting the data to a model for the scattering from lamellar structures. We extend a literature model [3], where the angular distribution can be decoupled from the scattering of a lamellar ‘stack’, and explicitly include the instrumental broadening [4]. By minimizing the sum of the squared-residuals between the model and the experimental data, we can determine the angular distribution of lamellae that best describes our samples. Figure 3 shows extracted angular

distributions for the three samples shown in Fig. 2, along with schematics of the inferred ordering. Variations in film thickness change the proportion between vertical and horizontal ordering. The rotational SANS technique cannot acquire data at near-grazing angles due to strong reflection from the substrate interface. However, neutron reflectometry is perfectly complementary in this regard, since it is sensitive to order in the film normal direction (the horizontal lamellae stacking). By using neutron reflectometry, we were able to corroborate the best-fit models obtained from the rotational SANS data: for some thicknesses, the horizontal lamellae form, whereas for other thicknesses their formation is suppressed. Moreover, the reflectometry makes it clear that the formation of horizontal lamellae is disrupted near the rough substrate interface.

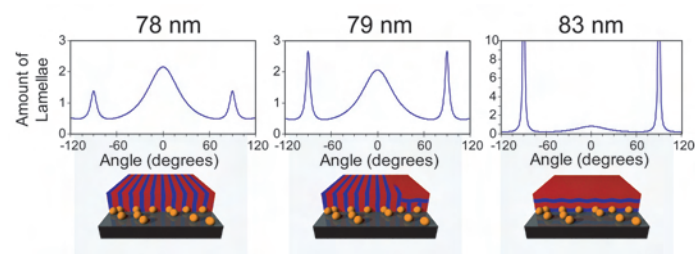


FIGURE 3: Best-fit orientational distribution of lamellae for the samples shown in Figure 2 (top row). The vertical peaks (0°) are broader than the horizontal peaks ($\pm 90^\circ$). Schematics of orientational order (bottom row) can be constructed from the distribution.

This analysis of the three-dimensional order helps elucidate the origin of the orientational changes. Block-copolymer lamellae on flat substrates always form horizontal sheets due to the strong wetting at the substrate interface. By introducing roughness, this wetting is disrupting, thereby making the vertical state energetically accessible. The oscillation as a function of thickness arises due to commensurability. When the film thickness is equal to a whole number of lamellae sheets, this arrangement is energetically favored. However, when the film thickness is incommensurate, and a whole number of layers cannot be formed, the horizontal state is unstable and the vertical state is instead the energy minimum. Combining the atomic force microscopy, neutron reflectometry, and rotational SANS thus gives a remarkably thorough picture of the film structure. By modeling the rotational SANS data, we can obtain quantitative angular distributions for the nanostructures, which are found to be consistent with the atomic force microscopy and neutron reflectometry data. This represents a general strategy that can be applied to a wide variety of nanostructures that assemble in thin films.

References

- [1] M. J. Fasolka and A. M. Mayes, *Annu. Rev. of Mater. Res.* **31**, 323 (2001).
- [2] E. Sivaniah *et al.*, *Macromol.* **38**, 1837 (2005); Y. Tsori *et al.*, *Macromol.* **38**, 7193 (2005); E. Sivaniah *et al.*, *Macromol.* **36**, 5894 (2003).
- [3] W. Ruland and B. Smarsly, *J. Appl. Cryst.* **37**, 575 (2004).
- [4] J. S. Pedersen, D. Posselt, and K. Mortensen, *J. Appl. Cryst.* **23**, 321 (1990).

Investigating the Structural Mechanisms of Shear Banding Using Spatially-resolved Flow-SANS

Matthew E. Helgeson and Norman J. Wagner¹; Lionel Porcar²

Shear banding is a flow-induced phenomenon observed in a wide variety of materials, including highly entangled polymers, self-assembled surfactants, colloidal suspensions, and pastes. Its rheological and macroscopic signatures have been well-studied for over a decade, yet surprisingly little is known about the underlying microstructural mechanism(s) that give rise to shear banding in soft matter. In this report, we demonstrate the capabilities of a new shear cell for spatially-resolved small angle neutron scattering (SANS) measurements in the flow-gradient (1-2) plane to elucidate the microstructural mechanisms by which shear banding occurs in a model wormlike micellar surfactant solution.

Perhaps the most well-studied fluids that exhibit shear banding are viscoelastic wormlike micelle (WLM) solutions, comprised of long, entangled threadlike aggregates of amphiphilic molecules [1]. Shear banding in these systems was originally observed visually as birefringent bands near the rotating wall of a Couette flow geometry [2]. The signature of banding is segregation of the flow field into two fluid layers, one at a high shear rate and one at a low shear rate, that span the flow geometry. These bands coincide with a stress plateau in steady state shear rheological measurements, (Fig. 1).

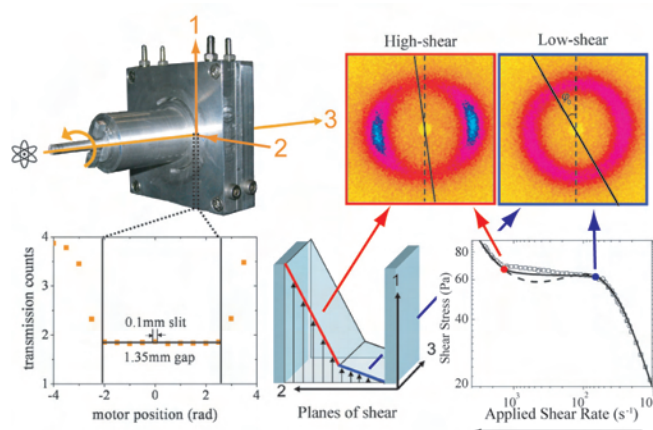


FIGURE 1: Diagram of the 1-2 plane flow-SANS shear cell. A plot of the neutron transmission demonstrates the gap resolution obtainable. The illustration shows the ability to probe gap-resolved structure in the two different shear bands.

Rheological theories that explain this behavior assume a non-monotonic constitutive stress-rate relationship, similar to a van der Waals loop equation of state for first order phase transitions [3]. This has led many investigators to propose that shear banding coincides with an underlying shear-induced phase transition. For example, the cationic surfactant CTAB in D₂O is known to shear band in the vicinity of an equilibrium isotropic-nematic (I-N) transition [4]. However, rigorous validation of this mechanism remains elusive, due to challenges in measuring separately the surfactant aggregate microstructure in both the high-shear and low-shear bands.

Recently, we have developed the ability to measure spatially-resolved microstructure under shear via SANS by using a short gap Couette cell and collimating the incident neutron beam down the gap (vorticity axis). A slit aperture enables collecting SANS from slices in the flow-gradient (1-2) plane of shear [5]. These 1-2 plane flow-SANS measurements provide several capabilities lacking in other techniques to measure structure under shear, namely: (1) the size ranges accessible by SANS cover the relevant microstructural scales of WLM solutions (e.g., micelle radius, persistence length, mesh size, etc.); (2) measurements in the 1-2 plane allow quantification of both the segmental orientation and degree of alignment, whereas more common measurements in the 1-3 plane measure only a projection of the segmental alignment [4]; (3) the slit aperture provides gap-resolved measurements of the structure, which allows discrimination between the high-shear and low-shear bands. Figure 1 shows a diagram of the shear cell and demonstration of these capabilities.

In this highlight, we report results for a model shear banding WLM of the cationic surfactant CTAB at 0.49 mol/L (490 mM) and 32 °C, for which the rheology and shear banding are well-characterized [6]. Flow-SANS measurements are performed at seven positions across the 1.35 mm Couette gap using a 0.1 mm slit. Figure 2 displays a visual summary of the results, where the intensity ring is a correlation peak due to segment-segment interactions. Anisotropy in this ring indicates segmental flow alignment, with high alignment typical for a nematic phase. A significant difference in scattering anisotropy is observed between positions in the low-shear and high-shear bands (also shown in Fig 1.)

¹University of Delaware, Newark, DE 19716

²NIST Center for Neutron Research, National Institute of Standards and Technology, Gaithersburg, MD 20899

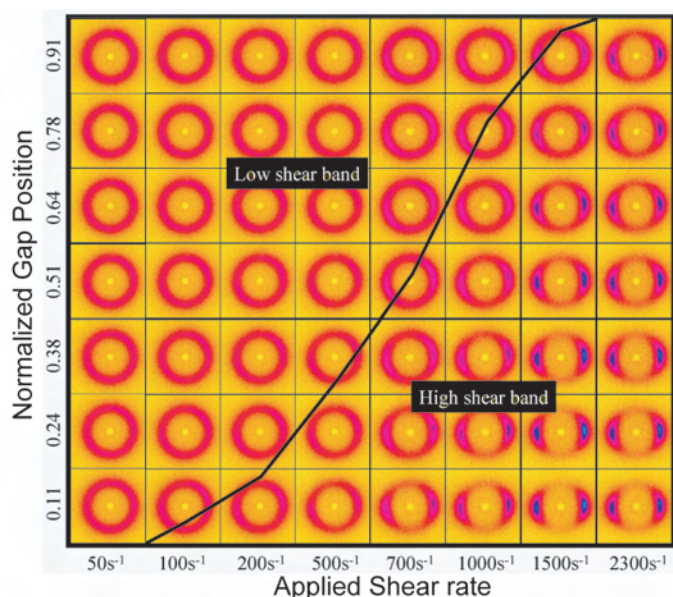


FIGURE 2: Two-dimensional scattering plots for nominal applied shear rates and normalized gap positions spanning the shear banding transition for the CTAB sample. The black line indicates the measured location of the interface between the high-shear and low-shear bands.

The average segmental orientation, φ_o , of the micelles relative to the flow direction is defined in Fig. 1, where $0^\circ < \varphi_o < 45^\circ$. Similarly, the net segmental alignment is given by the alignment factor, A_f , which characterizes the orientational order in the fluid [6]. As the average shear rate at each gap position is known from independent velocimetry measurements [6], all of the data can be plotted as master curves of φ_o and A_f versus the local shear rate (Fig. 3). Doing so demonstrates a clear transition at $\varphi_o \approx 10^\circ$ and $A_f \approx 0.15$, where a jump in orientation and alignment occurs between the low-shear and high-shear bands. Predictions from a constitutive model that couples the fluid's rheology and micellar orientation order are in excellent quantitative agreement in both low and high shear states.

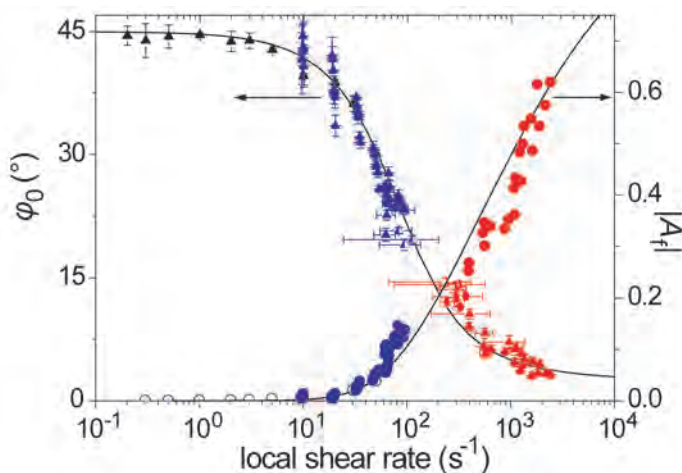


FIGURE 3: Orientation angle [closed] and alignment factor [open] versus local shear rate measured by velocimetry in the high-shear (red) and low-shear (blue) bands. Half filled symbols are for measurements with contributions from both bands. Data are augmented at low shear rates using flow-birefringence measurements [black]. Lines give predictions from the Giesekus model [solid].

The high degree of microstructural order observed at the highest shear rates is consistent with a flow-aligned nematic order, significantly less order is observed for non-banding WLM solutions at comparable shear rates [6]. This is further confirmed through sector-averaged plots of the intensity in the flow-aligned direction (Fig. 4), which show that the low shear band has a nearly identical structure to the fluid at rest, whereas the high-shear band shows an increase in sharpness and location of the structure peak similar to what is observed for an equilibrium nematic phase (shown for reference.) This confirms the hypothesis that shear banding results from a shear-induced I-N transition for CTAB. This is in contrast to some other surfactant systems that show a transition to a biphasic network structure [5]. Nonetheless, in both systems, the underlying thermodynamic phase behavior plays a critical role in determining how and when a fluid will exhibit shear banding.

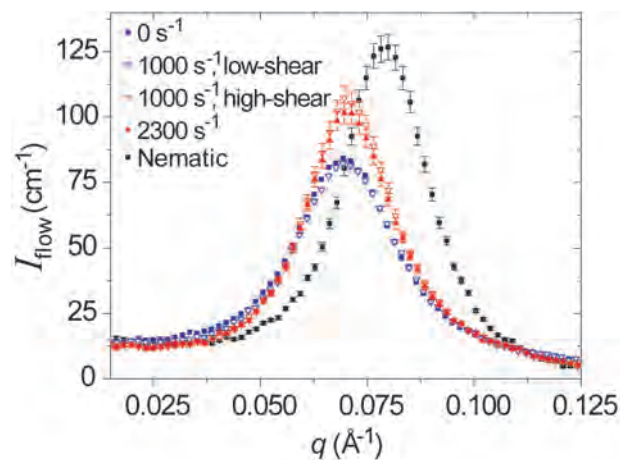


FIGURE 4: Sector-averaged intensity in the flow direction for the shear rates indicated. Open symbols show structure in the high-shear (red) and low-shear (blue) bands. The sharpening of the peak at high rates is similar to what is observed for a flow-aligned nematic phase at rest [black].

In conclusion, spatially-resolved 1-2 plane flow-SANS measurements enable direct measurement of the mesophase microstructure and orientational order of WLMs in each shear band under flow. The results provide critical information that is being used to test and refine microstructure-based models of shear banding [6]. This technique is unique in its ability to resolve local structure in non-homogeneous flows and as such is a powerful tool for quantitative interrogation of the nonlinear behavior of soft matter under shear.

References

- [1] H. Rehage and H. Hoffmann, *Molec. Physics* **74**, 933 (1991).
- [2] J. P. Decruppe, R. Cressely, R. Makhlofi, E. Cappelaere, *Coll. and Poly. Sci.* **273**, 346 (1995).
- [3] J. K. G. Dhont and W. J. Briels, *Rheol. Acta* **47**, 257 (2008).
- [4] J. F. Berret, in *Molecular Gels*, ed. R. G. Weiss and P. Terech (Springer, Netherlands, 2005), p. 663.
- [5] M. W. Liberatore, F. Nettesheim, N. J. Wagner, L. Porcar, *Phys. Rev. E* **73**, 020504 (2006).
- [6] M. E. Helgeson, E. W. Kaler, N. J. Wagner, P. A. Vasquez, L. P. Cook, *J. Rheol.*, Submitted (2008).

A Facile Route for Creating Reverse Vesicles in Organic Liquids

S.-H. Tung¹ and S. R. Raghavan¹

Vesicles are nanoscale containers formed in water and enclosed by a bilayer of lipid molecules. They are of great interest in drug delivery and nanomedicine due to their ability to encapsulate hydrophilic solutes in their aqueous interior. Much like such “normal” vesicles in water, one can also envision their counterparts in organic, nonpolar solvents (“oils”), which could be then termed “reverse” vesicles. If reverse vesicles could be formed easily and reproducibly, it is easy to imagine that they too could find numerous applications such as encapsulation and controlled delivery of hydrophobic solutes [1,2]. Here, we highlight our recent work [3] on a simple route to forming stable unilamellar reverse vesicles in nonpolar solvents such as cyclohexane. Our method also offers a general framework for tuning reverse aggregate geometry from reverse spherical micelles to reverse cylindrical micelles and finally to reverse vesicles.

Figure 1 schematically contrasts normal and reverse vesicles and also describes our method for forming the latter [3]. As is well-known, normal vesicles are formed in water by the self-assembly of long-tailed phospholipids such as L- α -phosphatidylcholine (lecithin), a natural two-tailed lipid with an average tail length of 17 carbons and an unsaturation in one of the tails. In the figure, lecithin is shown with a blue head (hydrophilic) and two red tails (hydrophobic). Note the structure of the bilayer in normal vesicles: here, the hydrophobic tails are in the interior of the bilayer so that they are shielded from water. To form reverse vesicles, we combine lecithin with a short-chain phospholipid, 1,2-dibutyroyl-*sn*-glycero-3 phosphocholine (C₄-lecithin) – a lipid with two four-carbon saturated tails. When added

to an oil (cyclohexane) at a high molar ratio R_0 of C₄-lecithin to lecithin, the lipids assembled into reverse vesicles. Note that the reverse vesicles have an oil core, and their shell is a reverse bilayer in which the hydrophobic portions of the lipids are exposed to the oil both in the core and in the exterior.

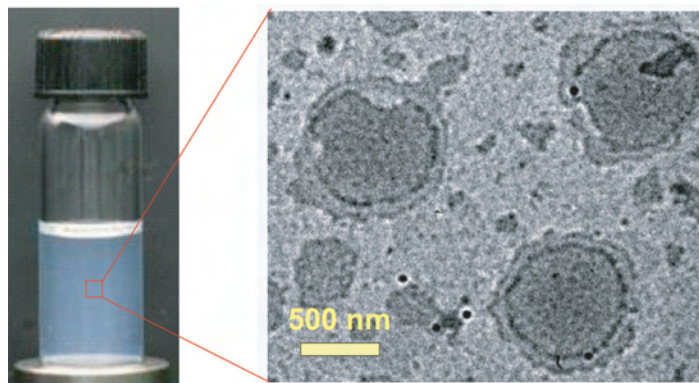
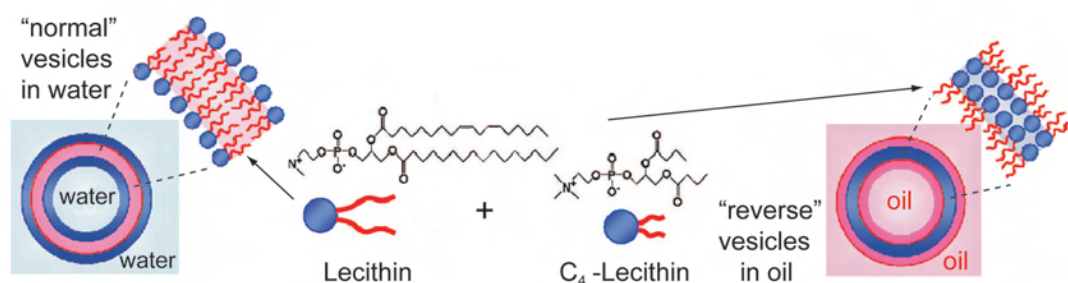


FIGURE 2: Photograph of sample vial and TEM micrograph of structures present in a C₄-lecithin + lecithin sample at $R_0 = 2.6$ (total lipids = 20 mmol/L, [NaCl] = 3.5 mmol/L).

Evidence for the presence of reverse vesicles in the mixed lipid solutions was obtained by a combination of dynamic light scattering (DLS), small-angle-neutron scattering (SANS) and transmission electron microscopy (TEM) [3]. The reverse vesicle sample ($R_0 = 2.6$) has a clear, bluish tinge, as seen from the photograph in Fig. 2. The bluish color is a manifestation of the Tyndall effect, *i.e.*, it is due to large scatterers in solution, and is a general feature of vesicles in water as well. DLS gives a hydrodynamic radius of 130 nm for the structures in the sample. Fig. 2 shows a TEM micrograph of the sample: here ammonium molybdate was added as a positive stain that would bind with the headgroups of lipids and thus clearly reveal the bilayers. The

FIGURE 1: Molecular structures of lecithin and C₄-lecithin, and schematics of their assemblies. Lecithin alone when added to water forms normal vesicles, which are illustrated schematically on the left. The present study shows that mixtures of lecithin and C₄-lecithin added into oil form reverse vesicles, as depicted on the right.



¹University of Maryland, College Park, MD 20742

TEM image shows a number of spherical structures with distinct shells, much like micrographs of normal vesicles. The diameters of these structures range from ≈ 300 nm to 1 μm . While these structures are larger than those expected from DLS, we believe this disagreement is due to the collapse or fusion of the reverse vesicles as the solvent is evaporated from the TEM grid.

To further elucidate the structure, we chose SANS, which was conducted on the NG-3 beamline at the NCNR [3]. Samples were made in deuterated cyclohexane to achieve the needed contrast between scatterers and solvent. SANS spectra (intensity *I* vs wave vector *q*) for 20 mmol/L lipid solutions are shown in Fig. 3 at varying R_0 . The data for $R_0 = 0$ and $R_0 = 0.5$ are both asymptotic to a plateau at low *q* and essentially correspond to micelles. In contrast, there is no plateau at $R_0 = 2.6$, with the data showing a q^{-2} decay of the intensity at low *q*. Such decay is a signature of scattering from vesicles. The SANS data thus indicate a transition from reverse micelles to reverse vesicles with increasing R_0 . We modeled the SANS data using appropriate form factors and the fits are shown as solid curves through the data. For lecithin in cyclohexane ($R_0 = 0$), the reverse micelles are ellipsoids with radii of 2.2 nm and 3.0 nm, respectively, for their minor and major axes. Upon the addition of small amounts of C_4 -lecithin, the micelles grow axially, and for $R_0 = 0.5$, they can be modeled as rigid cylinders (radius of 2.2 nm and length of 19.8 nm). For $R_0 = 2.6$, the data are fit to the polydisperse unilamellar vesicle model. An average reverse vesicle diameter of 234 nm is obtained, along with a bilayer thickness of 3.7 nm, and a polydispersity of 0.22. In sum, the SANS data confirm the evolution of self-assembled reverse structures from nearly spherical micelles to cylindrical micelles to vesicles with increasing molar ratio of C_4 -lecithin to lecithin.

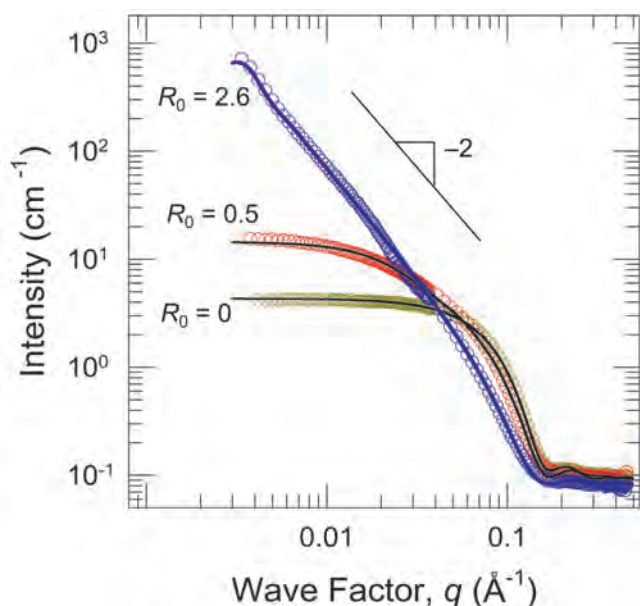


FIGURE 3: SANS spectra from lipid mixtures in deuterated cyclohexane for different C_4 -lecithin:lecithin molar ratios R_0 . The samples contain 20 mmol/L total lipid and 3.5 mmol/L NaCl.

Why does the addition of C_4 -lecithin induce the formation of reverse vesicles? It is known that the shape of self-assembled structures formed by amphiphiles is governed by their geometry [4]. This connection is usually expressed in terms of the critical packing parameter $p = a_{\text{tail}}/a_{\text{hg}}$, where a_{tail} and a_{hg} are the cross-sectional areas of the amphiphile's tail and headgroup, respectively. In the case of organic solvents, the formation of reverse micelles requires a packing parameter p much larger than 1, and spherical reverse micelles correspond to an inverse cone shape. For these spheres to transform into cylinders or vesicles, the packing parameter p has to decrease. We believe that such a decrease is caused by the binding of C_4 -lecithin to the lecithin headgroups. That is, since C_4 -lecithin has the same headgroup as lecithin but much shorter tails, it increases the headgroup area a_{hg} , while the overall tail area remains about the same. The net effect is to decrease p , and at high values of R_0 , the effective geometry is altered to a cylinder shape ($p \approx 1$), thus leading to reverse vesicles. Thus, our results can be placed within a general framework (or rules of thumb) for tuning reverse aggregate geometry.

One aspect that we have not discussed thus far is that, in addition to the two lipids, we must also add a trace amount of salt (e.g., NaCl) to ensure the stability of the reverse vesicles. Otherwise, the reverse vesicles become unstable and phase-separate. However, in the presence of a few mmol/L of salt, the reverse vesicles are very stable and robust, retaining their size and structure over a period of many months. Why is salt necessary? We believe that the salt ions (e.g., Na^+ and Cl^-) bind with the negative and positive charges on the lipid headgroups through short-range electrostatic interactions and thereby serve as a "glue" between the lipids [3].

In conclusion, we have demonstrated a new approach for creating reverse unilamellar vesicles in oils – it involves mixing short and long-chain lecithins along with a small amount of a salt such as NaCl. The components involved are commercially available and the reverse vesicles thus formed are stable and robust. Future experiments will examine the ability of reverse vesicles to encapsulate solutes in their interior. We hope that our approach will stimulate new interest into this fascinating class of self-assembled structures.

References

- [1] H. Kunieda *et al.*, *J. Am. Chem. Soc.* **113**, 1051 (1991).
- [2] H. Mollee *et al.*, *J. Pharm. Sci.* **89**, 930 (2000).
- [3] S.-H. Tung, H. Y. Lee and S. R. Raghavan, *J. Am. Chem. Soc.* **130**, 8813 (2008).
- [4] J. N. Israelachvili, *Intermolecular and Surface Forces*; Academic Press: New York, 1992.

Dispersions of Carbon Nanotubes in Polymers: Hierarchical Structure and Viscoelastic Properties

T. Chatterjee¹, A. Jackson^{2,3}, and R. Krishnamoorti¹

Nanoparticles demonstrate a number of advantages over traditional inorganic fillers used in the polymer industry as a result of their huge surface area per mass and often very high aspect ratio. In particular, dramatic improvements in tensile strength and, electrical and thermal conductivity have been observed at much lower mass fraction than traditional inorganic fillers. Understanding the origins of these structural improvements and associated rheological phenomena is important for optimizing the properties of polymer nanocomposites and their processing.

At relatively high concentrations, dispersed nanoparticles form superstructures and networks which can dominate the mechanical and rheological properties of the nanocomposites in a way that is only weakly dependent on the nature of the nanoparticles or of the polymer matrix [1, 2]. Specifically, *semi-dilute* dispersions of spherical silica nanoparticles, fractal carbon black, rod-like nanotubes, and disk-like layered-silicates show remarkable similarity in their rheological properties. These dispersions have a concentration of nanoparticles (p) significantly larger than the percolation threshold or jamming transition (p_c). Such dispersions in oligomeric or low molecular weight polymers demonstrate linear viscoelastic properties that are time-temperature-composition superposable and are gel-like.

The low-frequency modulus of these dispersions displays a concentration scaling $\sim (p - p_c)^3$, which corresponds to the network properties, independent of the chemical and topological identity of the primary nanoparticles. Using small and ultrasmall angle neutron scattering (SANS and USANS respectively), and focusing on the nature of the network structure formed by dispersed single walled carbon nanotubes (SWNTs) in a polymer matrix, we have identified the relationship between the network structure and rheological properties of such dispersions [1], which we briefly describe in this highlight.

Dispersions of SWNTs in three matrices, namely the epoxy resin matrices bisphenol A (BA), bisphenol F (BF) and the higher molecular mass poly(ethylene oxide) (PEO), were

examined. The viscosities for these matrices are comparable and range from 0.7 Pa s to 2.2 Pa s. The concentrations of SWNTs in each of the dispersions were chosen to ensure correspondence with the semi-dilute region ($2 \leq p/p_c \leq 15$), a range of practical importance as well as largely unexplored in terms of structure. The sample preparation, dispersion state, and linear rheological behavior of some of these systems have been discussed elsewhere [1, 3].

On the basis of previous studies on other nanoparticulate polymer systems, we hypothesize that on a macroscopic length scale a matrix-spanning network, consisting of aggregated clusters (flocs) of dispersed SWNTs, is established. The scattering is dominated by the large flocs, characterized by the cluster/floc size (R). Inside the floc, individual or small bundles of tubes (depending on the dispersion state) overlap and the average distance between two adjacent contacts is the network mesh size (ζ). A schematic diagram of this hierarchical structure is presented in Fig. 1.

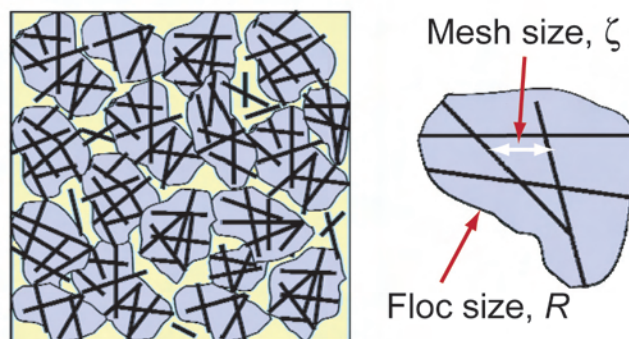


FIGURE 1: A schematic diagram of the hierarchical network structure showing two different length scales; we note that there can be quite a range of mesh sizes, ζ , and floc sizes, R .

The combination of SANS and USANS offers a broad range of scattering vector, q , ideal for the investigation of the hierarchy of length scales that are expected from dispersed SWNTs at concentrations in excess of the percolation threshold. The neutron scattering measurements were performed using the USANS instrument at BT-5 and the SANS diffractometer at NG-7 at the NCNR. The scattered intensity, when scaled by $p(1-p)$

¹University of Houston, Houston, TX 77204-4004

²NIST Center for Neutron Research, National Institute of Standards and Technology, Gaithersburg, MD 20899

³University of Maryland, College Park, MD 20742

(expected for disordered systems), superpose to form a master curve (Fig. 2), indicating the conservation of the structure over the concentration and length scales ($\sim q^{-1}$) examined. Scattering from a hierarchical fractal can be described by a unified equation with multiple structural levels [4].

$$I(q) = \sum_{i=1,2} G_i \exp\left(-\frac{q^2 R_{g,i}^2}{3}\right) + B_i \left(\left[\operatorname{erf}\left(\frac{q R_{g,i}}{\sqrt{6}}\right) \right]^3 / q \right)^{y_i}$$

In this description, $R_{g,1}$ gives a measure of the floc size R , and $R_{g,2}$ gives the mesh size ζ . G_1 gives a rough measure of floc number. The exponent y_1 corresponds to the average mass fractal dimension d_f of the floc, and y_2 to the fractal dimension d_{mesh} of the nanotube bundles.

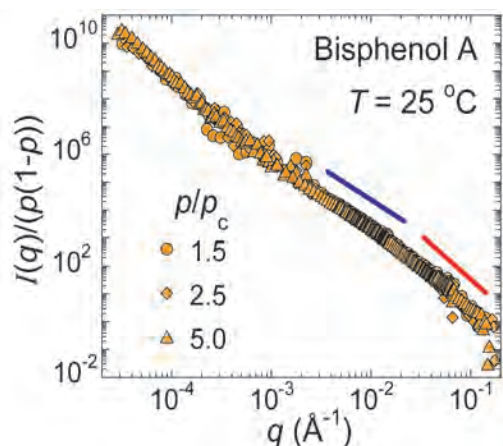


FIGURE 2: Concentration-effect corrected scattering data lead to a master curve indicating a hierarchical network structure over a wide range of length scales. The lines show slopes in two regions.

The d_f of the SWNTs network is found to be a function of the surrounding matrix. Matrices with a higher value of p_c exhibit a higher value of d_f and consequently denser aggregation within the flocs. The other relevant length scale of the network, the mesh size (ζ) shows a dependence on nanotube loading (Fig. 3). Increased loading corresponds to decreased ζ and exhibits a power law ($\zeta \sim p^{-\alpha}$) dependence with α values ranging between 0.3 (± 0.03) and 0.4 (± 0.05) for the systems studied here. These weak crowding values of α are consistent with diffusion-limited cluster formation [5].

Interestingly, the average floc size R is found to be $\approx 4 \mu\text{m}$ and almost independent of the surrounding matrix and particle concentration. The mesh fractal dimension, d_{mesh} , is found to be $\approx 2.8 \pm 0.1$ for all matrices, consistent with the formation of nanotube bundles as the basic unit of the SWNT network within the flocs.

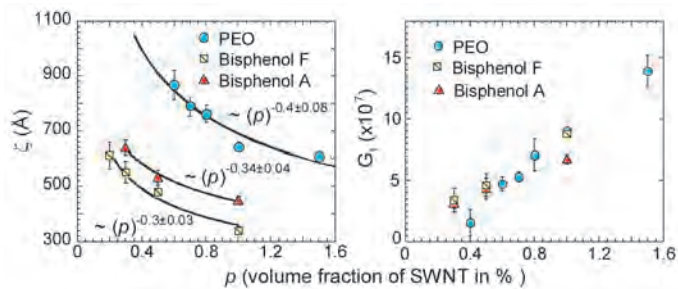


FIGURE 3: Concentration dependence of the network mesh size (ζ) and G_1 in different matrices. The scaling of ζ is consistent with diffusion limited floc formation while the nearly linear dependence of G_1 , roughly measuring floc number, suggests that the network primarily grows through new floc formation. Error bars are ± 1 standard deviation.

These structural results help in understanding the viscoelastic properties of these materials. The network elastic strength might be expected to be proportional to the number of stress-bearing junctions between nanotube bundles. But the high values of concentration scaling of the modulus observed for the three nanocomposite series (scaling exponents δ of 3.8 ± 0.3 , 2.5 ± 0.2 and 2.5 ± 0.4 for PEO, BA and BF systems, respectively) are not easily reconciled in the context of the composition-invariant floc size and the weak crowding of the mesh within a floc. On the other hand, G_1 demonstrates a nearly linear dependence with nanotube concentration ($\sim p^{1.1 \pm 0.1}$). Since for a 3D isotropic system the number of inter-floc contacts can be estimated to go as ($\sim p^{1.1 \pm 0.1}$)³, we suggest instead that the interactions between flocs (either directly or mediated by polymer), control the scaling dependence δ of the elastic strength of the network.

This study shows [6] that elastic properties in a variety of polymer nanocomposites may be primarily controlled by inter-floc interactions. The specific network elastic strength can thus be used as a quantitative tool to understand and compare nanoparticle dispersion in different matrices irrespective of the matrix, chemical and topological identity of the nanoparticle, and nanoparticle loading.

REFERENCES

- [1] T. Chatterjee, R. Krishnamoorti, Phys. Rev. E **75**, 050403 (2007).
- [2] T. Chatterjee, C. A. Mitchell, V. G. Hadjiev, R. Krishnamoorti, Adv. Mater. **19**, 3850 (2007).
- [3] T. Chatterjee, K. Yurekli, V. G. Hadjiev, R. Krishnamoorti, Adv. Funct. Mater. **15**, 1832 (2005).
- [4] G. Beaucage, J. Appl. Cryst. **29**, 134 (1996).
- [5] C. F. Schmidt, M. Barmann, G. Isenberg, E. Sackmann, Macromolecules **22**, 3638 (1989).
- [6] T. Chatterjee, A. Jackson, R. Krishnamoorti, J. Am. Chem. Soc. **130**, 6934 (2008).

Curved Neutron Guides: Phase Space Tailoring

J. C. Cook¹ and D. F. R. Mildner¹

Spectrometers that demand high Q -resolution or have long guide-free pre-sample drift paths, such as SANS or NSE instruments, require low divergence beams. To date at the NCNR, cold neutron beams have been delivered to these instruments either by straight guides with a cooled crystal filter, or by a neutron optical filter – a guide arrangement with one or more kinks that excludes direct lines of sight between the source and the instrument. The crystal filter is typically a liquid nitrogen-cooled, Be/Bi combination, with the Bi required because of the gamma sensitivity of area detectors. The main disadvantages of the crystal filter are that the minimum transmitted wavelength is set by the Be cutoff at about 4 Å, the filter materials attenuate the useful $\lambda > 4$ Å neutrons, the guide break for the filter cryostat generates additional losses, and the system is non-passive. Some of these problems are overcome using an optical filter; however, the transmission only tends to that of an unfiltered straight guide ideally in the long wavelength limit, and spatial-angular asymmetries in the beam may be present. We have developed a simple “phase-space tailoring” alternative whereby the guide transmission can ideally match that of an unfiltered straight guide of equivalent length with equivalent beam divergence for an extended wavelength range (often the entire operating range of the instrument) [1].

Consider first a two-dimensional unfiltered straight guide of length L , width W , and side coating critical angle ϑ , delivering a beam to an instrument whose minimum operating wavelength is λ_{min} . For idealized perfect reflectivity and guide entrance illumination, the emerging beam intensity is uniform across the guide width and uniform in angle between the limits $\pm\vartheta$, with unit transmission for the entire instrument wavelength range, provided that $L \geq W/\kappa\lambda_{min}$, with $\vartheta_c(\lambda) \approx \kappa\lambda$ where κ is a reflective coating-dependent constant. This situation would be ideal for the instrument except that excessive fast neutron and gamma transmission usually prohibits the use of an unfiltered straight guide. We propose, therefore, to precede the straight guide (whose critical angle is henceforth denoted by $\vartheta_{cstr} = \kappa_{str}\lambda$) with a circular-arc curved guide of radius ρ , width W , length L_c , and inner- and outer-curve surface coating critical angles, ϑ_{cin} and ϑ_{cout} respectively. The curved guide must function so as to (a) remove beam contaminants and (b) uniformly illuminate the straight guide within the required limits $\pm\vartheta_{cstr}$ for all wavelengths greater than λ_{min} . Satisfying both conditions is achieved by eliminating lines of sight within the curved section, which requires that $L_c \geq \sqrt{(8W\rho)}$. Condition (b) cannot be achieved

unless a beam entering at the inner surface just reaches the inner surface again upon exiting, which happens when $\vartheta_c \geq \sqrt{(2W/\rho)} = \psi_c$, the “characteristic angle”. The minimum wavelength, λ_c , for which this is possible occurs when $\lambda_c = \psi_c/\kappa_{out}$, where κ_{out} is the critical angle per unit wavelength of the outer surface coating. If $\psi(x)$ denotes the angle of a trajectory with respect to the guide axis at a transverse position x , the angular limits of neutrons transmitted through the curved guide for $\lambda > \lambda_c$ are described by the parabolas $\psi(x)^2 = \text{MIN}(\theta_{cin}^2 + \psi_c^2, \theta_{cout}^2) + \psi_c^2(x/W - 1/2)^2$, where $\vartheta_{cin} = \kappa_{in}\lambda$. From this equation and the definition of λ_c , it can be shown that when $\vartheta_{cin} < \vartheta_{cout}$, the divergence at the inner radius of the curved guide exit, $|\psi(x = -W/2)|$, “saturates” at ϑ_{cin} for all wavelengths exceeding $\lambda' = \lambda_c [\kappa_{out} / \sqrt{(\kappa_{out}^2 - \kappa_{in}^2)}]$ and increases parabolically to $|\psi(x = +W/2)| = \sqrt{\theta_{cout}^2 + \psi_c^2}$ at the outer radius (see dashed curve in Fig. 1). Note that for $\vartheta_{cin} \geq \vartheta_{cout}$ (i.e., $\lambda \rightarrow \infty$), or for $\lambda_c \leq \lambda < \lambda'$ this saturation is never achieved because $|\psi(x = -W/2)|$ is *always* less than ϑ_{cin} ; see solid parabola in Fig. 1.

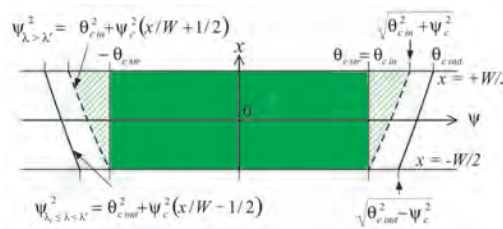


FIGURE 1: The acceptance diagram (transverse position x vs trajectory angle ψ) of a curved/straight guide system that is constrained by $\vartheta_{cin} = \vartheta_{cstr}$.

In conclusion, the idealized transmission of the curved-straight combination is 100 % (that of the *unfiltered* straight guide), the spatial-angular distribution is uniform, and the divergence is limited between $\pm\vartheta_{cstr}$ for all $\lambda > \lambda_{min}$ when the following four conditions are satisfied: (i) $L_c \geq \sqrt{(8W\rho)}$, (ii) $\kappa_{out} > \kappa_{in}$, (iii) $L_{str} \geq W/\kappa_{str}\lambda_{min}$, and (iv) $\lambda_{min} \geq (1/\kappa_{in})\sqrt{(2W/\rho)}/\sqrt{((\kappa_{out}/\kappa_{in})^2 - 1)}$. The combination guide acceptance is then represented by the solid green shaded region in Fig. 1. The unwanted, divergent part rejected by the straight guide is represented by the cross-hatching.

Example: A SANS guide requires a 5 cm wide beam with a divergence defined by the critical angle of natural Ni ($\kappa_{in} = \kappa_{str} = 1.73 \times 10^{-3}$ radians Å⁻¹) for all wavelengths greater than $\lambda_{min} = 4$ Å. Spatial constraints impose a minimum curved guide radius of 1500 m. Conditions (i) to (iv) then lead to $L_c \geq 24.5$ m, $\kappa_{out}/\kappa_{in} = 1.55$ (i.e., ϑ_{cout} is 55 % greater than that of natural Ni), and $L_{str} \geq 7.23$ m (minimum total guide length is 31.7 m). This is technically feasible.

References

[1] D. F. R. Mildner and J. C. Cook, Nucl. Instrum. Meth. A **592**, 414 (2008).

¹NIST Center for Neutron Research, National Institute of Standards and Technology, Gaithersburg, MD 20899

A Novel Optical Technique for Rapid Detection of Neutrons

A.K. Thompson¹, M.A. Coplan^{2,3}, J.W. Cooper³, P.P. Hughes¹, R.E. Vest², and C. Clark^{2,3,4}

Almost every instrument at the NCNR and other neutron scattering facilities depends on ³He proportional tube detectors because of their high efficiency, good background rejection, and reliability. New research results [1] may lead to a new detector for thermal and cold neutrons: the Lyman Alpha Neutron Detector (LAND). This detector, based on the same fundamental nuclear reaction as ³He proportional tubes, measures ultraviolet light of 122 nm wavelength produced by the reaction instead of amplifying and collecting charge. This new technique may be able to circumvent limitations of ³He proportional tubes while preserving their advantages over other techniques.

The fundamental nuclear reaction that is the basis of the LAND is $n + {}^3\text{He} \rightarrow t + p$, where n is a thermal or cold neutron, ${}^3\text{He}$ is the nucleus of an isotope of helium, and t and p are a tritium nucleus and a proton, respectively. The reaction releases 763 keV of energy that is shared between t and p . The velocities of the ³He atomic electrons and the outgoing t have similar magnitude, which makes it possible to have a reaction product that is a tritium atom (T) instead of a bare tritium nucleus. This tritium atom is likely to be formed in an excited state that quickly decays to its ground state, emitting one or more photons in the process. The decay from the first excited state of hydrogen to the ground state emits a characteristic photon at 121.6 nm, the “Lyman Alpha Line” (Ly_α). Because the energy needed to produce Ly_α light is 10.2 eV, there is enough energy available between the t and p to produce tens of thousands of photons.

The experimental apparatus (inset, Fig. 1) consisted of a gas cell with a neutron-transparent window, a gas-handling system to allow evacuating and filling the cell with ³He, ⁴He, or a mixture of the two, and a high-efficiency Ly_α sensitive photodetector (a Hamamatsu R6835 “solar-blind” photomultiplier, which detects light only between 120 nm and 180 nm). The detector was installed on the 4.96 Å NG-6M neutron beam line.

We measured photon detection rates with the gas cell evacuated, at various pressures of ⁴He, and at various pressures of ³He. The ⁴He has essentially no interaction with neutrons, and provides a check that we were not seeing signals produced by beam-related non-neutron radiation. A series of measurements both with and without a narrow band-pass filter demonstrated that the signal was within the filter bandwidth (8.7 nm bandwidth at 119.2 nm), and thus almost certainly Ly_α light.

Figure 1 shows the Ly_α photon yield per reacted neutron. If the photon production were a result of the $n + {}^3\text{He} \rightarrow t + p$ reaction alone,

their number per reacted neutron should be constant, independent of ³He pressure. Instead, the data fall on a curve. We take this as strong evidence that Ly_α photons are produced in atomic interactions with “spectator” ³He atoms occurring after the primary nuclear reaction. Preliminary theoretical calculations suggest that most of the radiation we observe comes from excitation of neutral atoms of H and T after they have been slowed to below 1 keV. At 93 kPa (700 Torr), 46 photons are produced for every neutron reacting with ³He. This high yield of photons is the main result of this investigation.

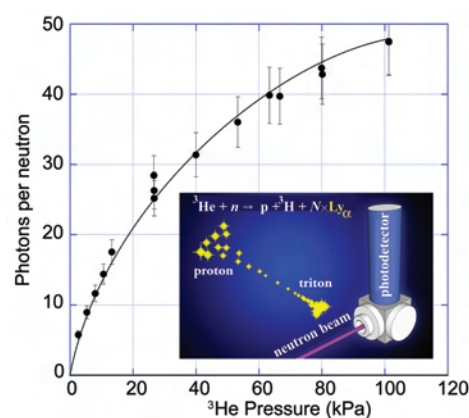


FIGURE 1: Lyman alpha photon yield per reacted neutron as a function of ³He pressure. The inset states the nuclear reaction and the cartoon indicates photon production and the experimental setup.

One way in which the LAND can improve upon current technology is in significantly reducing the time signal per detection event. Observed pulses were in the nanosecond range, compared to microseconds for typical ³He proportional tubes. Moreover, charge collection along a high-voltage anode wire requires a cylindrical geometry that has variable efficiency. The LAND would not be constrained to this geometry.

In sum, carefully calibrated experiments on a new type of neutron detector, LAND, using a ³He gas detector near atmospheric pressure, showed that tens of Ly_α photons were generated per neutron absorbed. In recognition of its promise for a transformational approach to neutron detection, this result has garnered a 2008 R&D 100 award for LAND as one of the most significant technologies developed during the previous year.

References

- [1] A.K. Thompson, M.A. Coplan, J.W. Cooper, P.P. Hughes, R.E. Vest and C. Clark, J. Res. Natl. Inst. Stand. Technol. 113, 69 (2008).

¹Ionizing Radiation Division, National Institute of Standards and Technology, Gaithersburg, MD 20899

²University of Maryland, College Park, MD 20742

³Electron and Optical Physics Division, National Institute of Standards and Technology, Gaithersburg, MD 20899

⁴Joint Quantum Institute, National Institute of Standards and Technology, Gaithersburg, MD 20899

Visualizing Nanoscale Magnetism in 3D with Polarized SANS

K. Krycka, J.A. Borchers, W.C. Chen, S. M. Watson, M. Laver, T. Gentile, B. Maranville;¹ C. Hogg, R. Booth, S. Majetich;² Y. Ijiri, C. Conlon;³ J. Rhyne⁴

Understanding how long-range magnetic correlations between nanoparticles form and evolve as a function of temperature, shape anisotropy, and near-neighbor particle proximity takes on heightened importance as technology increasingly utilizes nanoscale magnetism. For example, novel hyperthermia cancer treatment depends critically on the ability of magnetic nanoparticles to couple strongly for localized, high heat output. At the other extreme as densities of \approx TByte/cm² (TByte/in²) are approached, magnetic interparticle cross-talk in hard disk nanopatterned media must be minimized to avoid unintentional bit reversal during reading and writing. Both examples motivate the development of techniques for three dimensional (3D) profiling of these magnetic nanoparticle assemblies and this is where polarized small angle neutron scattering (SANS) excels.

with negligible loss [2]. Their polarizing efficiency, however, decays with a lifetime of 150 h to 200 h in our SANS set-up. Based on the formalism of Ref. 3, we have implemented an algorithm to extract all four polarization-corrected spin scattering cross-sections by explicitly including the ³He time dependence.

Our samples consist of ferromagnetic, monodispersed, magnetite nanoparticles 7 nm in diameter that exhibit strong magnetic coupling with an average edge-to-edge separation of 2.5 nm [4]. The nanoparticles form a powder of hexagonal close packed thin (several monolayer) crystallites on the order of a micrometer in the plane. A range of magnetic behaviors is experimentally accessible because the maximum temperature at which bulk ferromagnetism is observed (the blocking temperature) is well below room temperature.

To test our algorithm, we collected data at 50 K in a remanent magnetic field (2.5 mT to 3.0 mT) where the magnetic scattering should be nearly homogenous along the directions perpendicular (Y and Z) and parallel (X) to the neutron polarization. As shown in Fig. 1, the polarization-corrected data indeed exhibits this pattern. Even though the magnetic scattering is much smaller than the nuclear scattering, it can be fully resolved into its vectorial components (which happen in this case to be nearly the same).

Utilizing this technique, we studied the dependence of the magnetic correlation length on temperature from 50 K to 300 K. While the average structural separation remained constant, the long-range magnetic correlations showed marked decrease well past their ferromagnetic blocking temperature at 65 K. Quantitative analysis similar to Ref. 5 reveals that the magnetic domains ranged from 100 nm at 50 K (\approx 10 nanoparticles) to 10 nm (\approx 1 nanoparticle) at 300 K.

In conclusion we have shown that ³He spin filters with the appropriate time-dependent polarization correction can be used to perform full polarization analysis and subsequent 3D profiling of magnetic systems. We envision a suite of neutron magnetic techniques useful for investigating a variety of 3D systems such as biotagged magnetic sensors, *in situ* magnetically-manipulated bioprobes, controlled viscosity magnetic gels, self-assembled magnetic templates, and patterned thin-film magnetic media.

References

- [1] Y. Ijiri *et al.*, Applied Physics Letters **86** 243102 (2006).
- [2] G. L. Jones *et al.*, Physica B, **1131**, 385 (2006).
- [3] R. M. Moon *et al.*, Phys. Rev. **181** 920 (1969).
- [4] S. Sun and H. Zeng, J. Am. Chem. Soc. **124** 8204 (2002).
- [5] D. A. Farrell *et al.*, J. Magn. Magn. Mater. **303**, 318 (2006).

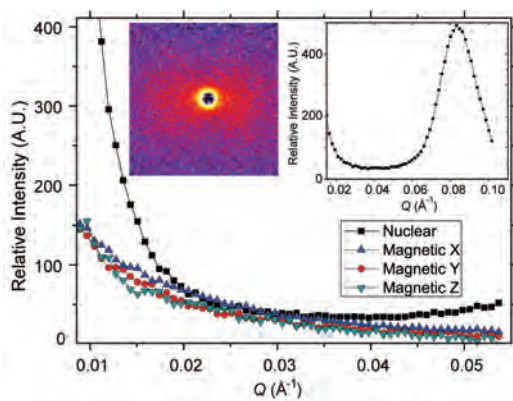


FIGURE 1: Magnetic and nuclear separation in a remanent magnetic field. The left inset is an asymmetric spin-flip scattering SANS pattern. The right inset shows nuclear scattering at larger Q . In the main plot nuclear scattering [black] is distinct from magnetic scattering [red and green: perpendicular to neutron polarization, blue: parallel].

Selecting the neutron polarization before small angle scattering from a sample and analyzing it after allows us to distinguish between non-spin flip scattering (involving nuclei and magnetic moments parallel to the neutron spin) and spin-flip scattering (magnetic moments perpendicular to the neutron spin). We can use these measurements to extract the magnetism and separate it into its average 3D components. This is important in systems where the nuclear scattering dominates the magnetic signal or when magnetic saturation cannot be achieved and used as a background [1].

The key to performing polarization analysis on a divergent scattered beam is to use a ³He spin polarized filter. These are excellent neutron spin polarizers/analyzers because of their high absorption asymmetry for parallel and anti-parallel neutron spins, and they can be reversed

¹NIST Center for Neutron Research, National Institute of Standards and Technology, Gaithersburg, MD 20899

²Carnegie Mellon University, Pittsburgh, PA 15213

³Oberlin College, Oberlin, OH 44074

⁴Los Alamos National Laboratory, Los Alamos, NM 87545

Neutron Phase Imaging with Talbot Optics

D.S. Hussey¹, S-W. Lee², D.L. Jacobson¹, and M. Arif¹

Neutron phase imaging can be potentially 10 to 100 times more sensitive than traditional neutron radiography, see Fig. 1a,b. However, it has seen limited application because the quasi-coherence required of the propagation technique reduces the incident neutron intensity by about 10^4 , which prevents realizing the improved sensitivity. By making use of the Talbot effect it is possible to form phase images with only a factor of two loss in intensity, which makes neutron phase imaging feasible.

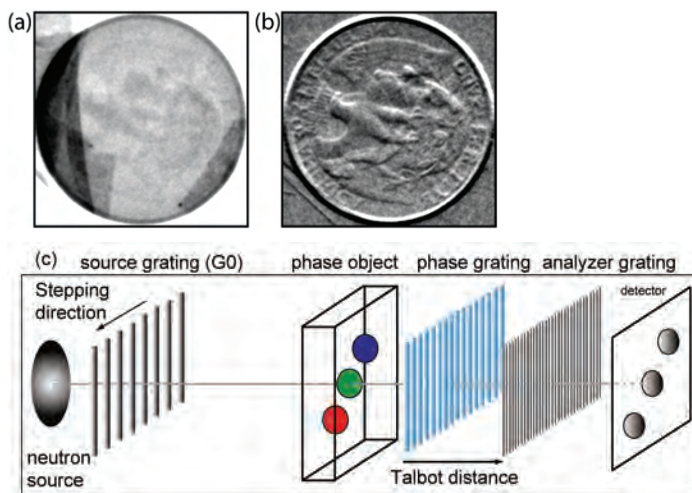


FIGURE 1: Comparison of the transmission image (a) to the neutron phase gradient image (b) of a U.S. quarter. The features of the quarter are not resolved in the transmission due to insufficient contrast. However, the eagle is clearly visible in the neutron phase gradient image. The setup is shown schematically in (c).

The Talbot effect is that a coherently illuminated phase grating produces a self-image at a specific downstream distance called the Talbot distance. Placing an object to be imaged in front of this phase grating (Fig. 1c) results in a phase shift of the self-image that is linearly related to the neutron phase gradient produced in the object. The neutron beam must be coherent only along the direction parallel to the phase grating but perpendicular to the grating lines. In our case the beam is formed with a source grating (G0) ($\approx 10 \mu\text{m}$ thick Gd lines with a $\approx 0.8 \text{ mm}$ period, 60 % duty cycle) which reduces the incident neutron intensity by 60 %. The phase grating is composed of lines of Si that are $30 \mu\text{m}$ thick and $4 \mu\text{m}$ wide periodically spaced by $8 \mu\text{m}$. The period of the self-image is smaller than current neutron detector resolution. However,

the self-image phase-shift can be measured by placing an absorbing analyzer grating at the Talbot distance, and then scanning the source grating through one period. The analyzer grating is composed of lines of Gd that are $3 \mu\text{m}$ thick and $2 \mu\text{m}$ wide periodically spaced by $4 \mu\text{m}$. The gratings were fabricated using the NIST Nanofabrication facility, and installed in a prototype phase imaging facility in the NG7 Neutron Interferometer and Optics Facility.

To obtain a neutron phase image with Talbot optics, a set of neutron images is acquired as the source grating is stepped through one period, analogous to a traditional neutron interferogram. Making a pixel-by-pixel comparison of the mean, amplitude, and phase shift of the interference patterns of the object to the open beam, one obtains the transmission image, the dark-field image, and the phase gradient image, respectively, as shown in Fig. 2. The neutron phase image can be obtained by integrating the phase gradient image along the dimension perpendicular to the phase grating lines.

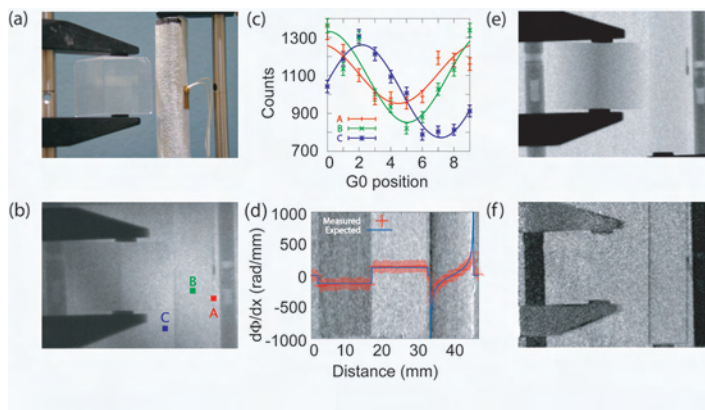


FIGURE 2: Talbot optics measurement. (a) A sapphire wedge and single crystal aluminum cylinder are a simple model system. (b) The raw image with the source grating (G0) stepped to the 4th position. (c) The interference pattern of points A, B, and C labeled in (b). (d) The neutron phase gradient image, and a plot of the average gradient and the expected phase gradient for the wedge and cylinder. (e) The transmission radiograph. (f) The dark-field image, which clearly shows the rough edges of the aluminum cylinder.

With the potentially greater sensitivity than radiography it may be possible to study residual stress in materials through the change in number density. Since the dark-field image is affected by the porosity of the material, Talbot optics would facilitate tomography of porous materials such as metal foams.

¹Physics Laboratory, National Institute of Standards and Technology, Gaithersburg, MD 20899-8461

²Korea Atomic Energy Research Institute, Daejeon, South Korea

Neutron Imaging Straw Detectors: Getting the Efficiency Right

R.G. Downing¹, L.R. Cao¹, J.L. Lacy²

Straw detectors are a new concept in position sensitive neutron detectors recently developed by Proportional Technologies, Inc. [1]. The detectors are especially valuable in large-area imaging applications and scattering instruments [2] and are being installed at the Spallation Neutron Source (SNS) at Oak Ridge National Laboratory. The atomic thickness of boron carbide deposits on the individual tubes is critical to the efficiency of the overall detector. Neutron Depth Profiling (NDP) [3], a nondestructive metrological technique, has played a critical role in optimizing the performance of these novel high resolution neutron systems.

Neutrons are not easily detected with high resolution and good efficiency. Consequently high-quality neutron detectors remain a challenge to manufacture. A few nuclides such as ^3He , ^{10}B and ^6Li are commonly used to convert impinging neutrons into an electrical pulse for electronic post-processing. The two most commonly used neutron position sensitive detectors are the ^3He proportional counter and the $\text{ZnS}/^6\text{LiF}$ scintillator. The first has, perhaps, the highest detection efficiency, but is costly to make and the spatial resolution is relatively poor. The latter has better spatial resolution, but suffers as an optimal solution since the afterglow in a scintillator can last for up to $10\ \mu\text{s}$, making it unsuitable for any high count event application [4].

The neutron-active surface of a straw detector is sputter-coated with enriched boron carbide ($^{10}\text{B}_4\text{C}$). In operation, two highly energetic charged particles are generated by neutron capture within the deposited width. One of those two particles must escape the deposit and ionize gas within the hollow straw to generate a signal pulse. The signal is read out via the suspended wire running through the center of the straw. Many straws are close-packed into a 2D array to form a large area neutron position-sensitive detector (Fig. 1a).

The ^{10}B atomic density of $^{10}\text{B}_4\text{C}$ coating applied to the straw strongly influences detector efficiency and overall performance. The $^{10}\text{B}_4\text{C}$ coating must be sufficiently thin to permit efficient escape of one or the other reaction product emitted upon each neutron reaction with a ^{10}B atom. Otherwise, the event is lost in self absorption. Furthermore, if the film is too thick, remaining neutrons cannot continue along their trajectories to the next straw, leading to further inefficiency. Obviously, the accurate determination of ^{10}B depth distribution (stoichiometry) and total mass – not linear thickness – of this thin ($0.1\ \mu\text{m}$) lining is critical in the manufacture of straw elements. The required metrology is readily achieved using NDP.

Sample coupons were selected representing material along the length and width of the $^{10}\text{B}_4\text{C}$ deposition chamber. NDP spectra were then determined from each sample; three spectra are overlaid and presented in Fig. 1b illustrating the variations in the atomic thickness of B found. NDP results revealed that the masks used in applying the film yielded a smoothly varying thickness in coating across the chamber, see Fig. 1c. Using the metrology provided by NDP, a practical and reliable approach to compensate the deposition mask was provided as determined in subsequent production runs.

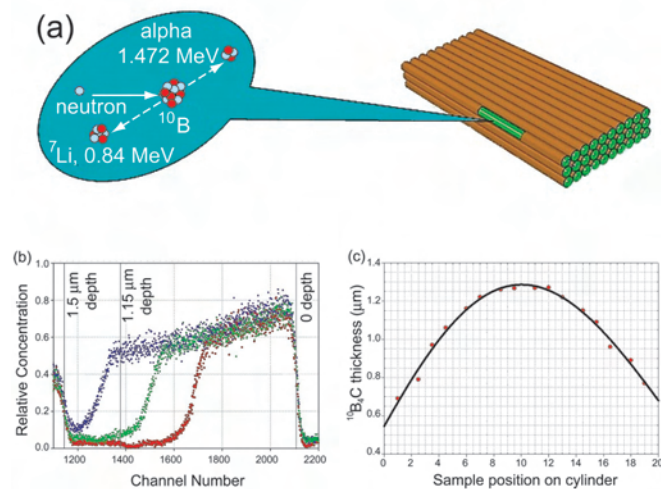


FIGURE 1: (a) Illustration of a 3D stack of straw detectors. The balloon shows the neutron- ^{10}B reaction. (b) An overlay of three NDP spectra for samples deposited with different masses of $^{10}\text{B}_4\text{C}$. Only the 1.472 keV alpha particle portion of the spectrum is shown. (c) A plot of the boron carbide thickness versus position in the deposition chamber as determined by NDP in the first production lots.

References

- [1] J.L. Lacy, Patent, Proportional Technologies, Inc.: USA (2005).
- [2] A. Athanasiades, N.N. Shehad, C.S. Martin, L. Sun, J.L. Lacy, IEEE Trans. Nucl. Sci., **N14-4**, 123 (2005).
- [3] R.G. Downing, G.P. Lamaze, J.K. Langland, S.T. Hwang, J. Res. Natl. Inst. Stand. Technol. **98**, 109 (1993).
- [4] N.J. Rhodes, Neutron News, **17**, 16 (2006).

¹Chemical Science and Technology Laboratory, National Institute of Standards and Technology, Gaithersburg, MD 20899

²Proportional Technologies, Inc., Houston, TX 77054